5-1992

Solid-State NMR Studies of Organometallic Complexes

Ae Ja Kim
Louisiana State University and Agricultural and Mechanical College

SOLID-STATE NMR STUDIES OF ORGANOMETALLIC COMPLEXES

A Dissertation

Submitted to the Graduate Faculty of the
Louisiana State University and
Agricultural and Mechanical College
in partial fulfillment of the
requirements for the degree of
Doctor of Philosophy

in

The Department of Chemistry

by
Ae Ja Kim
B.S., Ewha Womans University, Seoul, Korea, 1981
M.S. in Chemistry, Ewha Womans University, Seoul, Korea, 1986
May 1992

MANUSCRIPT THESES

Unpublished theses submitted for the Master's and Doctor's Degrees and deposited in the Louisiana State University Libraries are available for inspection. Use of any thesis is limited by the rights of the author. Bibliographical references may be noted, but passages may not be copied unless the author has given permission. Credit must be given in subsequent written or published work.

A library which borrows this thesis for use by its clientele is expected to make sure that the borrower is aware of the above restrictions.

LOUISIANA STATE UNIVERSITY LIBRARIES

Acknowledgements

First of all, I would like to thank Dr. Leslie G. Butler for his guidance and patience in the preparation of this work. Appreciation is extended to the members of the advisory committee: Dr. Andrew W. Maverick, Dr. James W. Robinson, Dr. Paul S. Russo, Dr. Robert J. Gale, and Dr. Richard L. Imlay. I would also like to thank numerous colleagues and friends at Louisiana State University.

The financial support from the National Science Foundation (CHE–8715517) and the Louisiana Board of Regents through the Louisiana Educational Quality Support Fund is gratefully acknowledged. The purchase of the Bruker MSL200 NMR spectrometer was made possible by NSF grant CHE–8711788. In addition, I wish to thank the financial assistance from the Charles E. Coates Memorial Fund in preparing this dissertation.

Finally, I would like to extend appreciation to my family for their help and encouragement.

To my husband and my parents

Table of Contents

List of Tables

List of Figures

List of Programs

Abstract

Solid-state NMR spectroscopy has been used to obtain information about electronic structure and molecular geometry for some organometallic complexes. The principal elements of the ^{13}C chemical shielding tensor for a dimetallocyclopropane unit and three square-planar metal cyanides have been determined from a nonlinear least-squares fit of the chemical shift powder pattern. For the dimetallocyclopropane unit, the orientation of the chemical shielding tensor with respect to the molecular axis has been assigned based on the dipolar coupling tensor. The principal elements of the ^{31}P chemical shielding tensor for three binuclear platinum diphosphite complexes have been obtained from a Herzfeld–Berger graphical analysis of the MAS spectra. The paramagnetic contribution to the ^{13}C chemical shielding tensor is related to the metal-carbon bonding interaction.

The deuterium quadrupole coupling constants and the asymmetry parameters for six bridging metal hydride complexes have been acquired from a nonlinear least-squares fit of the deuterium powder pattern. The relationships between the quadrupole coupling constant and the M–H bond length and between the asymmetry parameter and the M–H–M bond geometry are discussed on the basis of a point charge model.

Deuterium MAS spectra for four simple inorganic compounds and two physical mixtures have been obtained. The resolution of two inequivalent deuterium sites in the mixtures is described by the quality of the fit between experimental and calculated MAS spinning sideband intensities.

A fitting method using a Levenberg–Marquardt nonlinear least-squares algorithm is described for the extraction of the NMR parameters from the solid-state NMR powder patterns.

CHAPTER 1

Introduction

The critical feature of solid-state NMR spectroscopy is the preservation of the anisotropic character of various spin interactions, chemical shielding, J coupling, dipolar, and quadrupolar interactions, due to the relatively fixed orientations of the molecules with respect to the applied magnetic field.[1] In the case of dilute spins with I=1/2 (^{13}C, ^{31}P), the solid-state NMR spectra are dominated by the chemical shielding and the dipolar interactions. Solid-state NMR spectra of dilute spins, with enhanced signal-to-noise ratio, have been obtained with the development of the cross-polarization method. Dilute spin double resonance[2], 2D separated local field[3], and 2D rotational spin-echo[4] techniques have been used to separate the dipolar interaction from chemical shielding. The principal elements of the chemical shielding tensor provide three-dimensional information on electronic structure, in a way, a fundamental probe of the nature of the chemical bonding at a specific site. The dipolar coupling tensor can be used to find the orientation of the chemical shielding tensor relative to the molecular coordinate system. Another important aspect of the dipolar coupling tensor is to furnish information concerning molecular geometries such as bond lengths and bond angles.

In the case of quadrupolar nuclei (deuterium, I=1), the solid-state NMR spectra are dominated by the quadrupolar interaction, characterized by the quadrupole coupling constant and the asymmetry parameter. Because of the large line widths of solid-state deuterium spectra, up to 250 kHz, it is frequently difficult to detect deuterium NMR spectra. The recent application of quadrupolar spin-echo technique and the Fourier transform gives a dramatic improvement in deuterium NMR line shape for very large spectral widths.[5, 6]

Solid-state NMR spectroscopy has been widely used to study the molecular geometry, electronic structure, and motion of molecules in organic and biological systems, but there are few studies of organometallic complexes. ^{13}C chemical

shielding tensors have been measured in metal carbonyls to investigate the metal-carbonyl bonding[7-11] and in metal sandwich complexes to study the ring rotation[12,13]. ^{31}P chemical shielding tensors have been successfully correlated with structural parameters such as bond angle in phosphido-bridged complexes[14] and bond length in phosphine-metal complexes[15]. In addition, the solid-state structures[16] and the *cis* and *trans* isomers[17,18] of $(R_3P)_2MX_2$ (M = Pd, Pt) have been studied by CP/MAS spectroscopy. Deuterium quadrupole parameters have been obtained for characterization of terminal metal hydride sites in $(\eta_5\text{-}C_5H_5)_2M(^2H)_2$ (M = Mo, W, Zr)[19-21] and of rotational jump motion for the cyclopentadienyl ring in $(\mu\text{-}CO)_2[FeCp(CO)]_2$[22].

The principal objective of the research described in this dissertation is to demonstrate the application of the solid-state NMR spectroscopy for studies on several different aspects of organometallic chemistry. In the course of this work, contributions have been made in the interpretation of NMR parameters as well as procedures for extracting the parameters from solid-state NMR powder patterns. Thus, this work provides a foundation for future NMR work in the fields of organometallic chemistry, catalysis, and materials science. The focus of the research described herein is on the determination of the characteristic NMR parameters from the line shape analysis of the NMR powder pattern and the understanding of the structural and chemical aspects of organometallic complexes in the solid-state structures.

In Chapter 2, the principal elements and the orientation relative to the molecular axis system of the ^{13}C chemical shielding tensors have been obtained to yield three-dimensional information on molecular structure and the associated electronic structure for the bridging methylene unit in *cis*-$(\mu\text{-}CH_2)(\mu\text{-}CO)[FeCp(CO)]_2$. Two important aspects are shown in this chapter. First, the dipolar coupling can be used to determine the orientation of the chemical shielding tensor in the principal axis system. Second,

the paramagnetic contribution to the chemical shielding tensor is related to a molecular orbital description of the bonding at the methylene carbon site.

The influence of the molecular geometry at the bridging metal hydride site on the deuterium quadrupolar parameters is described in Chapter 3. The relationships between the quadrupole coupling constant and M–H bond length and between the asymmetry parameter and the M–H–M bond angle are described on the basis of a point charge model.

The ^{13}C chemical shielding tensors for metal cyanide complexes and the ^{31}P chemical shielding tensors for binuclear platinum diphosphite complexes are given in Chapter 4. The diamagnetic contribution to the chemical shielding tensor for the metal cyanide complexes has been estimated using Flygare–Goodisman's approximation. The applicability of Flygare–Goodisman's approximation to transition metal complexes is also discussed.

In Chapter 5, the ability to resolve two inequivalent deuterium sites in mixtures is described. The deuterium MAS NMR spectra are compared with simulations based on the Herzfeld–Berger method and the quality of the fit is noted for one and two component models. The significant feature is that the spin rate must be slower than the difference between the quadrupole coupling constants in order to resolve two distinct deuterium sites.

In Chapter 6, a fitting method for solid-state NMR powder patterns is described. The Levenberg–Marquardt algorithm for a nonlinear least-squares analysis is used to extract characteristic NMR parameters from the overall line shape of the NMR powder pattern. Four examples of fitting of the chemical shift and dipolar-coupled chemical shift powder patterns and the deuterium powder pattern are shown.

Finally, Chapter 7 summarizes this research and suggests recommendations for future work.

References for Chapter 1

(1) Fyfe, C. A. *Solid State NMR for Chemists*; C.F.C. Press: Ontario, 1983.

(2) Pines, A.; Gibby, M. G.; Waugh, J. S. *J. Chem. Phys.* **1973**, *59*, 569-90.

(3) Linder, M.; Höhener, A.; Ernst, R. R. *J. Chem. Phys.* **1980**, *73*, 4959-70.

(4) Munowitz, M. G.; Griffin, R. G.; Bodenhausen, G.; Huang, T. H. *J. Am. Chem. Soc.* **1981**, *103*, 2529-33.

(5) Bloom, M.; Davis, J. H.; Valic, M. I. *Can. J. Phys* **1980**, *58*, 1510-7.

(6) Hentschel, R.; Spiess, H. W. *J. Magn. Reson.* **1979**, *35*, 157-162.

(7) Walter, T. H.; Reven, L.; Oldfield, E. *J. Phys. Chem.* **1989**, *93*, 1320-6.

(8) Aime, S.; Botta, M.; Gobetto, R.; Osella, D.; Milone, L. *Inorg. Chim. Acta* **1988**, *146*, 151-2.

(9) Hasselbring, L.; Lamb, H.; Dybowski, C.; Rheingold, A. *Inorg. Chim. Acta* **1987**, *127*, L49-L51.

(10) Oldfield, E.; Keniry, M. A.; Shinoda, S.; Schramm, S.; Brown, T. L.; Gutowsky, H. S. *J. Chem. Soc., Chem. Comm.* **1985**, 791-3.

(11) Gleeson, J. W.; Vaughan, R. W. *J. Chem. Phys.* **1983**, *78*, 5384-92.

(12) Sayer, I. *J. Chem. Soc., Chem. Commun.* **1988**, 227-8.

(13) Wemmer, D. E.; Pines, A. *J. Am. Chem. Soc.* **1981**, *103*, 34-6.

(14) Carty, A. J.; Fyfe, C. A.; Lettinga, M.; Johnson, S.; Randall, L. H. *Inorg. Chem.* **1989**, *28*, 4120-4.

(15) Lindner, E.; Fawzi, R.; Mayer, H. A.; Eichele, K.; Pohmer, K. *Inorg. Chem.* **1991**, *30*, 1102-7.

(16) Rahn, J. A.; O'Donnell, D. J.; Palmer, A. R.; Nelson, J. H. *Inorg. Chem* **1989**, *28*, 1631-5.

(17) Rahn, J. A.; Baltusis, L.; Nelson, J. H. *Inorg. Chem.* **1990**, *29*, 750-5.

(18) Nelson, J. H.; Rahn, J. A.; Bearden, W. H. *Inorg. Chem.* **1987**, *26*, 2192-3.

(19) Ireland, P. S.; Olson, L. W.; Brown, T. L. *J. Am. Chem. Soc.* **1975**, *97*, 3548-9.

(20) Jarrett, W. L.; Farlee, R. D.; Butler, L. G. *Inorg. Chem.* **1987**, *25*, 1381-3.

(21) Wei, I. Y.; Fung, B. M. *J. Chem. Phys.* **1971**, *55*, 1486-7.

(22) Altbach, M. I.; Hiyama, Y.; Wittebort, R. J.; Butler, L. G. *Inorg. Chem.* **1990**, *29*, 741-7.

CHAPTER 2

The ^{13}C NMR Chemical Shielding Tensor of the Bridging Methylene Unit in *cis*-(μ-CH_2)(μ-CO)[FeCp(CO)]$_2$‡

by
Ae Ja Kim, Maria I. Altbach, and Leslie G. Butler*†

Contribution from the Department of Chemistry
Louisiana State University, Baton Rouge, Louisiana 70803-1804

*to whom correspondence should be addressed.
†Fellow of the Alfred P. Sloan Foundation (1989-91).
‡Keyword index: solid state ^{13}C NMR, bridging methylene, nanoscopic MRI, chemical shielding, dipolar coupling

Abstract

The principal elements of the ^{13}C NMR chemical shielding tensor have been determined for the bridging methylene unit in *cis*-(μ-CH_2)(μ-CO)[FeCp(CO)]$_2$ from a combination of a Herzfeld–Berger analysis of the CP/MAS spectrum and a nonlinear least-squares fit of the proton-decoupled ^{13}C powder pattern. The $^{13}CH_2$ unit is both spatially isolated from other magnetic nuclei in the solid and largely motionally decoupled from dipolar interactions with the Cp ring protons. For the purpose of interpreting the proton-coupled ^{13}C powder pattern, we have assumed that the carbon site of the dimetallocyclopropane unit lies on the intersection of two perpendicular mirror planes of symmetry. With this assumption, there are six possible relative orientations of the $^{13}CH_2$ unit with respect to the principal axis system of the ^{13}C chemical shielding tensor; simulations of the proton-coupled ^{13}C powder patterns have been compared to the experimental spectrum and the orientation of the chemical shielding tensor with respect to the molecular frameworks has been assigned. The C–H bond length and the H–C–H bond angle were obtained from the dipolar coupling tensor. A single, very large paramagnetic chemical shielding tensor element is a result of relatively weak carbon–metal bonds through two carbon atomic p orbitals and strong C–H bonds with the remaining carbon p orbital. Thus, these results are consistent with a molecular orbital analysis in which the methylene unit has σ-donating a_1 and π-accepting b_1 valence orbitals.

2.1. Introduction

The chemical and physical properties of bridging methylene metal dimers are fascinating.[1] With a hydride acceptor, $(\mu\text{-}CH_2)(\mu\text{-}CO)[FeCp(CO)]_2$ can be converted to a bridging methine metal cation;[2] treatment with a non-coordinating acid yields an agostic methyl-bridged cation.[3] Such reaction chemistry should be influenced in part by the charge resident on the bridging methylene carbon.[4] Two measures of carbon charge have yielded differing results. The binding energies of the C_{1s} orbital for several bridging methylene metal dimers are significantly less than for cyclopropane, indicative of a negative charge relative to the aliphatic reference.[5] Yet, for *cis*-$(\mu\text{-}C^2H_2)(\mu\text{-}CO)[FeCp(CO)]_2$, solid-state deuterium NMR shows that the electric field gradient at deuterons bound to carbon is nearly the same as found for deuterium bound to an aliphatic carbon site, suggesting the same charge as the reference.[6] The wide range of chemical and physical properties relative to an aliphatic methylene site emphasizes the importance of the metal-carbon interaction. A molecular orbital picture of the bonding between a CH_2 unit and the metal dimer has been developed by a number of groups.[7] The salient features are carbon based σ-donating a_1 and π-accepting b_1 valence orbitals interacting with metal based orbitals. With the presence of low-lying metal-carbon antibonding orbitals, one can anticipate an unusual ^{13}C NMR chemical shielding interaction. Herein, we report the results of a solid-state ^{13}C NMR study of a bridging methylene metal dimer, *cis*-$(\mu\text{-}^{13}CH_2)(\mu\text{-}CO)[FeCp(CO)]_2$.

An important feature of NMR studies is the ability of the spectroscopist to predict the general features of the spectrum on the basis of a knowledge of the interaction Hamiltonians, molecular geometry, molecular dynamics, and electronic structure. Because one aspect of the these results is so clearly defined, the major orientation of the chemical shielding tensor, this study provides a textbook example for what is often considered an obtuse area of NMR spectroscopy, the prediction of chemical shielding interactions based upon molecular and electronic structure.

With respect to the spectroscopy, there are two features of note in this work. First, in the context of I_2S spin systems, this study is one of the few in which orientation of the ^{13}C chemical shielding tensor[8,9] has been determined with use of a powder sample[10] rather than a single crystal, though rather more examples now exist for ^{15}N.[11-14] Several techniques have been developed for dealing with powdered samples: separated local field,[15-17] analyses of critical frequencies,[13,18] dipolar modulation,[19,20] and matching a dipolar coupled powder pattern.[18,21-23] In this work, calculated proton-coupled ^{13}C powder patterns were matched to the experimental spectrum. As a check, a separated local field spectrum was also calculated and matched to the corresponding experimental spectrum. Second, the ^{13}C chemical shift anisotropy for the bridging methylene site is very large, much larger than a typical methylene site[24] and exceeded only by sites such as metal carbonyls and carbon monoxide.[25,26] In fact, it is this very large chemical shift anisotropy that makes possible a qualitative correlation between the orientation of the chemical shielding tensor and the electronic structure of the bridging methylene unit.

2.2. Theory

2.2.1. Electronic Structure and the Chemical Shielding Tensor.

Chemical shielding is a sum of paramagnetic and diamagnetic contributions: $\sigma_{\alpha\alpha} = \sigma_{\alpha\alpha}^{para} + \sigma_{\alpha\alpha}^{dia}$ (α = x, y, z). Herein we use ^{13}C chemical shifts referenced to TMS with positive shifts to higher frequency, i.e., the isotropic chemical shift of benzene is +128.7 ppm. Therefore, $\sigma_{\alpha\alpha}^{para}$ is positive and $\sigma_{\alpha\alpha}^{dia}$ is generally negative. For ^{13}C sites in diamagnetic compounds, the diamagnetic contribution has a limiting value of about –90 ppm[26] and has less orientational dependence than the paramagnetic contribution.[27,28] Thus, we assume that most of the chemical shielding anisotropy will be due to the paramagnetic term; the component along the x-axis is given here:

$$\sigma_{xx}^{para}(TMS) = \frac{\mu_0 e^2}{8\pi m} \sum_{k\neq 0} \frac{1}{(E_k - E_0)} \left[\left\langle \psi_0 \left| \sum_i L_{ix} \right| \psi_k \right\rangle \left\langle \psi_k \left| \sum_i \frac{L_{ix}}{r_i^3} \right| \psi_0 \right\rangle + \left\langle \psi_0 \left| \sum_i \frac{L_{ix}}{r_i^3} \right| \psi_k \right\rangle \left\langle \psi_k \left| \sum_i L_{ix} \right| \psi_0 \right\rangle \right] \quad (2.1)$$

where μ_0 is the permittivity of free space, e is the charge of the electron, and m is the mass of the electron.[29] The wavefunctions ψ_0 and ψ_k refer to ground and excited molecular states as do, respectively, the state energies, E_0 and E_k. With the origin at carbon, r_i is the distance to the i-th electron and L_{ix} is the angular momentum operator for the i-th electron. In spite of the complexity of eq 2.1, many useful results have been obtained by evaluating eq 2.1 with use of wave functions derived from molecular orbital calculations.[30-32]

Generally, there is not sufficient information to evaluate the integrals contained in eq 2.1. For this reason, a set of approximations is commonly applied for a simple chemical shielding analysis. These approximations are the following:

(1) The ground- and excited-state molecular wave functions can be approximated by high-lying bonding and low-lying antibonding orbitals, ϕ and ϕ^*, respectively.

(2) For integrals of the type $\left\langle \phi \left| \sum_i L_{ix} \right| \phi^* \right\rangle$, the only nonzero component is centered on the carbon site[33] and is of the form $\left\langle p_z \left| \sum_i L_{ix} \right| p_y \right\rangle \neq 0$ where the Levi–Civita angular momentum rules[34] can be used to evaluate the integral.

(3) All of the nonzero integrals have the same constant, positive value.

With these quite gross, but common, approximations, the expression for the paramagnetic contribution is greatly simplified. A further simplification occurs for sites with C_{2v} symmetry; a coordinate system can be defined such that atomic p_x, p_y, and p_z orbitals at a site do not mix. Chart I shows the coordinate system for a bridging methylene site.

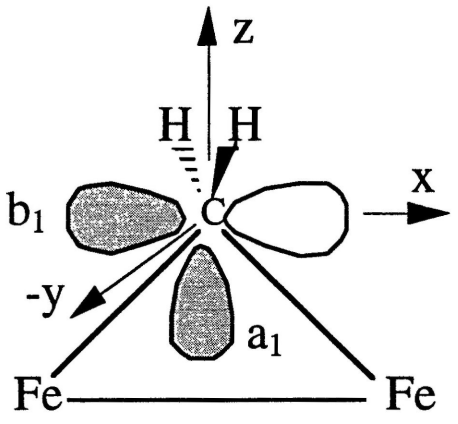

I

For the carbon site, the paramagnetic contribution to the chemical shielding along the y-axis is

$$\sigma_{yy}^{para}(TMS) \propto \frac{1}{\left(E_{a_1}^* - E_{b_1}\right)} + \frac{1}{\left(E_{b_1}^* - E_{a_1}\right)} \qquad (2.2)$$

where E_{a_1} and $E_{a_1}^*$ are the energies of high-lying bonding and low-lying antibonding orbitals with a contribution from the carbon p_Z orbital. Similarly, E_{b_1} and $E_{b_1}^*$ are related to the carbon p_X orbital. We note that expressions similar to eq 2.2 have been generated before.[35,36] However, the present work is unique in that the experimental data for the bridging methylene unit contains one element that is so exceedingly large that we may reasonably expect the approximations listed above to be qualitatively valid. Finally, the convention used herein for the relative assignment of the principal components of the chemical shielding tensor is $\sigma_{11} \geq \sigma_{22} \geq \sigma_{33}$ and $\sigma_{iso} = \frac{1}{3}(\sigma_{11} + \sigma_{22} + \sigma_{33})$; again, tensor elements, $\sigma_{\alpha\alpha}$, are referenced to TMS.[9,37]

2.2.2. Spectroscopy of I_2S Spin Systems. Herein, we give a brief outline of the procedure used to simulate the proton-coupled ^{13}C powder patterns. Briefly, we treat the methylene unit as an isolated three-spin system and calculate the transitions in the frequency domain by solving the time-independent total Hamiltonian

for the spin state energies.[15b,34] Carbon transition frequencies are summed over a range of possible orientations of the methylene unit with the applied magnetic field. The total Hamiltonian, in frequency units (rad s^{-1}), for the three spin system is

$$H_{\text{total}} = H_{\text{CS}}^{\text{C}} + H_{\text{Zeeman}}^{\text{H}} + H_{\text{dipolar}}^{\text{hetero}} + H_{\text{dipolar}}^{\text{homo}} \tag{2.3}$$

where the chemical shielding interaction, H_{CS}^{C}, is given by

$$H_{\text{CS}}^{\text{C}} = -\hbar\gamma^{\text{C}}\mathbf{B}_0 \cdot (\tilde{1} - \tilde{\sigma}) \cdot \mathbf{S}^{\text{C}} \tag{2.4}$$

and where γ^{C} is the gyromagnetic ratio for ^{13}C, $\mathbf{B}_0$ is the applied magnetic field, $\tilde{1}$ is the identity matrix, and $\mathbf{S}^{\text{C}}$ is the carbon spin angular momentum operator.[34] The chemical shielding tensor, $\tilde{\sigma}$, is a second-rank tensor with nine elements. Only the symmetric components of the tensor contribute in first order to the normal NMR spectrum.[37] With the TMS scale, there is a change in sign in eq 2.4, such that

$$H_{\text{CS}}^{\text{C}} = -\hbar\gamma^{\text{C}}B_z^0\left(1 + \sigma_{\text{Lab}}^{zz}\right) S_z^{\text{C}} \tag{2.5}$$

where we also note that the only nonzero component of the magnetic field is along the laboratory z-axis. The transformation between the laboratory coordinate system (Lab) and the molecular coordinate system (PA) is done with direction cosine matrices[38] by using the y-convention[39]:

$$\tilde{\sigma}_{\text{Lab}} = \mathbf{R}_N^{-1}(\theta)\,\mathbf{R}_z^{-1}(\chi)\,\tilde{\sigma}_{\text{PA}}\,\mathbf{R}_z(\chi)\mathbf{R}_N(\theta) \tag{2.6}$$

The proton Zeeman interaction, $H_{\text{Zeeman}}^{\text{H}}$, is given by

$$H_{\text{Zeeman}}^{\text{H}} = -\hbar\gamma^{\text{H}}B_z^0[I_{z1} + (1+\varepsilon)I_{z2}] \tag{2.7}$$

where I_{z1} and I_{z2} are spin angular momentum operators for hydrogen at sites 1 and 2,

respectively. The slight difference in chemical shift between sites 1 and 2, $\varepsilon = 10^{-9}$ ppm, is made so as to render the two sets of proton spin state energies nondegenerate as the algorithm used to assign spin quantum numbers to each proton spin state is suitable only for nondegenerate energy levels.

The dipolar interactions are separated into heteronuclear and homonuclear interactions. The heteronuclear dipolar coupling is given by

$$H_{\text{dipolar}}^{\text{hetero}} = \frac{\gamma_C \gamma_H \hbar}{\left|\mathbf{r}_{\text{Lab}}^{H1}\right|^3}\{[S_xI_{x1} + S_yI_{y1} + S_zI_{z1}] + [S_xI_{x2} + S_yI_{y2} + S_zI_{z2}]\} -$$
$$3\frac{\gamma_C \gamma_H \hbar}{\left|\mathbf{r}_{\text{Lab}}^{H1}\right|^5}\{[S_xr_{x1} + S_yr_{y1} + S_zr_{z1}][I_{x1}r_{x1} + I_{y1}r_{y1} + I_{z1}r_{z1}] +$$
$$[S_xr_{x2} + S_yr_{y2} + S_zr_{z2}][I_{x2}r_{x2} + I_{y2}r_{y2} + I_{z2}r_{z2}]\} \qquad (2.8)$$

in a molecular axis framework in which the carbon site is the origin and the vectors $\mathbf{r}_{\text{PA}}^{H1}$ and $\mathbf{r}_{\text{PA}}^{H2}$ define the positions of hydrogen sites H1 and H2, respectively, in the principal axis system. We have assumed that both C–H bond lengths are the same; $\left|\mathbf{r}_{\text{PA}}^{H1}\right| = \left|\mathbf{r}_{\text{PA}}^{H2}\right|$. Transformation of the vectors from the principal axis system into the laboratory axis system is again done with direction cosine matrices:

$$\mathbf{r}_{\text{Lab}}^{H1} = \mathbf{r}_{\text{PA}}^{H1}\,\mathbf{R}_z(\chi)\mathbf{R}_N(\theta). \qquad (2.9)$$

Similarly, the homonuclear dipolar coupling is given by

$$H_{\text{dipolar}}^{\text{homo}} = \frac{\gamma_H \gamma_H \hbar}{\left|\mathbf{r}_{\text{Lab}}^{H1} - \mathbf{r}_{\text{Lab}}^{H2}\right|^3}[I_{x1}I_{x2} + I_{y1}I_{y2} + I_{z1}I_{z2}] -$$
$$3\frac{\gamma_H \gamma_H \hbar}{\left|\mathbf{r}_{\text{Lab}}^{H1} - \mathbf{r}_{\text{Lab}}^{H2}\right|^5}\{[I_{x1}(r_{x1} - r_{x2}) + I_{y1}(r_{y1} - r_{y2}) + I_{z1}(r_{z1} - r_{z2})] \times$$
$$[I_{x2}(r_{x1} - r_{x2}) + I_{y2}(r_{y1} - r_{y2}) + I_{z2}(r_{z1} - r_{z2})]\} \qquad (2.10)$$

The spin angular momentum operators are defined for the uncoupled product basis set

of |H1 H2 ^{13}C > by direct product expansion from the Pauli spin matrices. There are six allowed ^{13}C transitions: | α, α, α > → | α, α, β >, | α, β, α > → | α, β, β >, | α, β, α > → | β, α, β >, | β, α, α > → | β, α, β >, | β, α, α > → | α, β, β >, and | β, β, α > → | β, β, β >.[15b] The spin-state energy levels are assigned the spin quantum number of the carbon based on a conditional test of the diagonal elements of $U^{\dagger} S_z^C U$; greater than zero indicates β and less than zero indicates α, and likewise, similar tests are performed for the two hydrogen nuclei. The unitary matrix, U, is obtained from the diagonalization of H_{total}. The carbon powder pattern, with proton dipolar coupling, is then obtained by summing the carbon transition frequencies over a range of χ, θ orientations over the range of 0 to 90°, inclusive, with sin θ weighting.[22] Typically, we use a uniform step angle of 2° and the calculation takes ca. 70 minutes on a VAXstation 3200. Figure 2.1 shows the six proton coupled ^{13}C powder patterns for a methylene unit for which the axes of the dipolar and chemical shielding tensors are colinear.

2.3. Experimental Methods

2.3.1. Sample Preparation. The preparation of $(\mu\text{-}^{13}CH_2)(\mu\text{-}CO)[FeCp(CO)]_2$ was based on literature methods.[41] The Wittig reagent was prepared starting from triphenyl phosphine and ^{13}C-labelled (99%) methyl iodide.

$$(C_6H_5)_3P + {}^{13}CH_3I + NaH \rightarrow (C_6H_5)_3P={}^{13}CH_2 + H_2 + NaI$$

$$(C_6H_5)_3P={}^{13}CH_2 + (\mu\text{-}CO)_2[FeCp(CO)]_2 \rightarrow$$

$$\textit{cis, trans}\text{-}(\mu\text{-}{}^{13}CH_2)(\mu\text{-}CO)[FeCp(CO)]_2$$

Low temperature column chromotagraphy was used to isolate the *cis* isomer. *Cis-trans* isomerization is facile in hexane solution at room temperature.[42] Also, the *cis* isomer can crystallize in both monoclinic[41a] and triclinic space groups.[43] On the

basis of X-ray powder diffraction, both forms are present in the sample used herein. Because the structure factors for the monoclinic form are not available, the relative abundance of each form can not be calculated. However, the diffractions corresponding to the triclinic form are more intense that those due to the monoclinic form; thus, we judge that the triclinic form is more abundant.

2.3.2. Solid-State ^{13}C NMR Spectroscopy. Solid-state ^{13}C NMR spectra were taken with Bruker MSL 200 solid-state NMR spectrometer operating at 50.301 MHz for ^{13}C provided with a temperature control unit which uses a copper-costantan thermocouple junction located near the MAS stator. While there are clear advantages to performing NMR experiments and the corresponding simulations at different magnetic field strengths, this was not done here.[18,23] A 15 kHz CP/MAS probe was used and the ~80 mg powdered sample was loosely packed into a 4 mm ZrO_2 rotor with a Kel-F cap. The data acquisition was via a standard single contact Hartmann-Hahn cross-polarization pulse sequence for the sample spinning experiments.[44] Slight modifications of this pulse sequence were used for acquiring the powder patterns: The proton-decoupled ^{13}C chemical shift powder pattern was acquired as a spin echo following an 80 μs delay. The proton-coupled ^{13}C powder pattern was also acquired as a spin echo following an 80 μs delay, however, the proton decoupling rf irradiation was terminated at the maximum of the spin echo. The slow spinning speed CP/MAS spectra were acquired in the same manner as the proton-decoupled ^{13}C chemical shift powder pattern; however, the delay in the spin echo sequence was set to the inverse of the spinning rate. The proton 90° pulse was 3 to 5 μs, though the probe tended to arc at the higher power levels. The cross-polarization contact time ranged between 0.1 and 5 ms and the recycle delay was 3 s. Typically, 10000 to 20000 free induction decays were acquired and an exponential linebroadening factor of 500 Hz was applied. The chemical shielding values are recorded on the

δ-scale indirectly referenced through adamantane (external) to tetramethylsilane (TMS). Fourier-transformed and manually-phased spectra were transferred as binary data files from the Bruker Aspect-3000 computer to a Macintosh II computer via an RS-232 serial connection and the KERMIT file transfer protocol.[45] Conversion from binary to ASCII data files was done with a program[46] written in LabVIEW, a graphical programming language.[47] Spectral simulation programs were written in Matlab v3.5f, a vector oriented programming language.[48] The Levenberg–Marquardt nonlinear least-square algorithm[49] was recoded in Matlab and the data variance was assigned on the basis of a selected region of the baseline. Recently developed techniques in critical frequency analysis were considered but not used.[13,18,23]

2.4. Results

The large chemical shielding anisotropy of the bridging methylene site in *cis*–(μ-$^{13}CH_2$)(μ-CO)[FeCp(CO)]$_2$ is readily apparent from the ^{13}C chemical shielding powder pattern shown in Figure 2.2a. The unusually large anisotropy for the methylene site is much larger than for the aromatic carbons in the cyclopentadienyl ligands of the related complex, *cis*–(μ-CO)$_2$[FeCp(CO)]$_2$, shown in Figure 2.2b, with $\sigma_\perp$ = 122.6 (6) and $\sigma_\parallel$ = 18.2 (12) ppm (TMS).[50] The presence of two magnetically inequivalent bridging methylene sites is revealed in the CP/MAS spectrum shown in Figure 2.2c. The CP/MAS spectrum at 10 kHz shows two bridging methylene sites in a 60:40 relative abundance based upon peak heights, σ_{iso} = 145.6 (60% abundant, triclinic) and σ_{iso} = 139 ppm (40%, monoclinic), and where the crystal morphology is tentatively assigned on the basis of the relative intensities of the X-ray powder diffraction lines. Because of the similarity in the spinning sideband pattern, the elements of the chemical shielding tensors for both the monoclinic and triclinic sites are similar.

There are several steps in the determination of the elements of the chemical shielding tensor and its orientation with respect to the molecular axis system. First, the proton-decoupled ^{13}C powder pattern was fitted to a model consisting of monoclinic and triclinic bridging methylene sites plus a contribution from the Cp carbons. Second, a Herzfeld–Berger analysis was done to verify an assumption made in the previous model. Third, the proton-coupled ^{13}C powder pattern was compared to the calculated patterns shown in Figure 2.1. Fourth, the fit to the proton-coupled ^{13}C powder pattern was optimized by varying d(C–H) and ∠H–C–H. Fifth, the assigned orientation was confirmed by the correspondence between experimental and calculated 2D separated local field spectra.

Figure 2.3 shows the results of a nonlinear least-squares fit to the chemical shielding powder pattern. The fitted variables include σ_{11}^{mono} and σ_{22}^{mono}; the value of σ_{33}^{mono} is determined from σ_{11}^{mono} and σ_{22}^{mono} and the isotropic chemical shift. We make the assumption that $\sigma_{\alpha\alpha}^{tri} = \sigma_{\alpha\alpha}^{mono} + 6.6$ ppm ($\alpha = 1, 2, 3$); the reason for this constraint is the close correspondence between the two chemical shielding tensors that would otherwise lead to a singularity in the nonlinear least-squares fitting. Finally, a fixed contribution from the Cp carbons sites is also included. With this model, we find $\sigma_{11}^{mono} = 365.7$ (6), $\sigma_{22}^{mono} = 75.5$ (1), and $\sigma_{33}^{mono} = -24.2$ (6) ppm. The value of $\chi_\nu^2 = 2.0$ (step angle = 2°, data variance = 2%) indicates that this model is tenable. There are two sources of systematic errors that are of concern: anisotropic cross polarization and finite pulse length effects. Briefly, anisotropic cross polarization is evident as a decreased cross polarization rate at orientations ("magic angle") for which the dipolar coupling between ^1H and ^{13}C is quenched.[24,51] An interesting experiment to test for anisotropic cross polarization in this system would be to acquire the ^{13}C chemical shielding powder pattern without cross polarization and compare the fit of this data to the model. Unfortunately, the long ^{13}C T_1, on the order of 100 s,

precluded acquisition of the spectrum without cross polarization. Finite pulse length effects would be evident as a reduced intensity in the experimental spectrum at the extremes. We note that the fit is poorest at 20 kHz, as would be expected for a systematic error due to finite pulse length effects.

In a Herzfeld–Berger analysis, the relative intensities of the spinning sidebands in series of CP/MAS spectra are used to determine the elements of the chemical shielding tensor.[52] However, here we have used the Herzfeld–Berger analysis for a more restricted application, verifying the difference between the chemical shielding tensor elements of the monoclinic and triclinic sites. Shown in Figure 2.4 are the results of the analysis which show that $\sigma_{\alpha\alpha}^{tri} = \sigma_{\alpha\alpha}^{mono} + 6.6$ ppm ($\alpha = 1, 2, 3$). It is possible to show the results for both sites since the calculated spinning sideband intensities depend only on the values of $\sigma_{33} - \sigma_{22}$ and $\sigma_{iso} - \sigma_{11}$. Because the experimental spinning sideband intensities for both crystallographic forms can be fitted to the same set of calculated traces, the constant 6.6 ppm difference between tensor elements of the two forms is confirmed. We note, however, that this technique is not particularly sensitive at the spin rates we can access.

Figure 2.5a shows the proton-coupled ^{13}C powder pattern for *cis*–(μ-$^{13}CH_2$)(μ-CO)[FeCp(CO)]$_2$. A simple comparison of the experimental results with the previously calculated spectra suggests a match with chemical shielding orientation shown in Figure 2.1a. The match with one of the spectra of Figure 2.1 indicates that the methylene unit can be treated as an isolated $^{13}CH_2$ spin system. Also, the Cp rings are rapidly rotating about an axis from the iron atom through the centroid of the Cp ring. In the related complex, *cis*–(μ-CO)$_2$[FeCp(CO)]$_2$, the Cp rings are executing C_5 jumps at a rate of (2.4 (5))x10^{11} s^{-1}.[53] With this rapid motion, the dipolar interaction between the $^{13}CH_2$ unit and the protons of the Cp rings is much reduced. The jump rate is temperature dependent. Since spectra taken at –10 and 40 °C showed no significant variation, aside from random noise, from the spectrum shown in

Figure 2.5a, we conclude that dipolar coupling between the $^{13}CH_2$ unit and the Cp protons is negligible.

The result of the nonlinear least-squares fit to the proton-coupled ^{13}C powder pattern is shown in Figure 2.5b where the fitted variables are vertical scale and vertical offset. Fixed parameters include the isotropic chemical shifts for the triclinic and monoclinic forms, the 60:40 relative abundance, d(C–H) = 1.1 Å, and ∠H–C–H = 109.5°. The contribution of the Cp ring sites to the proton-coupled ^{13}C powder pattern was ignored since the spectrum of *cis*–(μ-CO)$_2$[FeCp(CO)]$_2$ showed only a weak, broad resonance. The value of χ^2_ν is 2.7 (step angle = 2°, data variance = 2%) indicating that the model is tenable. Again, there is a possibility that systematic error may have been caused by anisotropic cross polarization. We note here the similarity in the pulse sequences used to acquire the spectra in Figures 3a and 5a. Since we have shown in Figure 2.3a that a ^{13}C spin echo has been prepared without detectable flaw caused by anisotropic cross polarization, we can then expect the proton-coupled ^{13}C powder pattern to be similarly unafflicted by artifacts. Thus, we are assured that apparent good fit of the proton-coupled ^{13}C powder pattern to Figure 2.1a is not an accidental coincidence associated with a powder pattern modulated by anisotropic cross polarization.

A proton-coupled powder pattern contains geometric information. We recall that the fit shown in Figure 2.5b was obtained with a fixed methylene geometry. The proton-coupled ^{13}C powder pattern was fitted while allowing the parameters d(C–H) and ∠H–C–H to vary. The nonlinear least-squares routine successfully converged on the values: d(C–H) = 1.122 (3) Å and ∠H–C–H = 110.8 (4)°, and the value of χ^2_ν is reduced to 2.1; thus, the fit is significantly better at the 95% confidence level than for previous fit with fixed d(C–H) and ∠H–C–H. For the comparison of bond lengths determined from NMR dipolar couplings with those obtained from scattering

experiments such as neutron diffraction, compensation must be made for the effect of molecular motions upon the measurements.[54] For the NMR experiments, Henry and Szabo have shown that the averaging of $\langle 1/r^3 \rangle$ for a ^{13}C–H unit is affected by the C–H stretching vibration and the librational motions of the molecule.[55] Generally, vibrational averaging of the NMR dipolar coupling acts to weaken the interaction such that the uncorrected bond length is too long, about 2.3 % (propane methylene)[55] to 2.7 % (benzene).[56] If extensive librational motions are present, say for the methylene units in solid octane, even larger correction factors are required.[55] On the basis of the C–H stretching frequency for the bridging methylene site,[6] and if we also assume that libration motions are similar to those for the propane methylene, then the corrected value of d(C–H) is 1.096 (3) Å. For comparison, the bridging methylene geometries in related rhodium and osmium complexes as determined from neutron diffraction are as follows: *trans*-(μ-CH_2)[RhCp(CO)]$_2$, d(C–H) = 1.095 (2), 1.094 (2) Å and ∠H–C–H = 110.4 (1);[57] (μ-H)$_2$(μ-CH_2)$Os_3(CO)_{10}$, d(C–H) = 1.090 (11), 1.091 (10) Å and ∠H–C–H = 106.0 (8).[58] In the X-ray crystallography work for *cis*-(μ-CH_2)(μ-CO)[FeCp(CO)]$_2$, the methylene hydrogen atoms were located and refined isotropically to give d(C–H) = 0.95 (3) and 1.00 (4) Å and ∠H–C–H = 110 (3).[43] The correspondence between the corrected NMR distance and those obtained from neutron diffraction is exceptionally good. But given the uncertainty associated the librational motions, the correspondence may be coincidental.

A 2D separated local field spectrum was acquired and is shown in Figure 2.6. The general features of the 2D spectrum correspond well with the calculated 2D spectrum obtained with the orientation of the chemical shielding as shown in Figure 2.1a. The dipolar projection along the F1 dimension is particularly sensitive to the orientation of the chemical shielding tensor and the experimental and calculated projections agree quite well. The 2D results confirm the orientation previously assigned on the basis of the 1D results.

2.5. Discussion

The chemical shielding elements for *cis*–(μ-$^{13}CH_2$)(μ-CO)[FeCp(CO)]$_2$ cover a very large range relative to methylene units in organic compounds; for comparison, in *n*-eicosane, $CH_3CH_2(^{13}CH_2)_{16}CH_2CH_3$, the chemical shielding elements (TMS scale) are σ_{11} = 50.2 (20), σ_{22} = 38.2 (20), and σ_{33} = 17.2 (20).[24] The chemical shielding elements are comparable to those found for CO and for terminally bound metal carbonyls: ^{13}CO (20 K, argon matrix), σ_{11} = 305, σ_{22} = 305, and σ_{33} = –48;[26] (μ-^{13}CO)$_2$[FeCp(CO)]$_2$, σ_{11} = 354, σ_{22} = 354, and σ_{33} = –85.[25]

It is often difficult to correlate chemical shielding in organometallic complexes with chemical bonding. One approach that appears particularly useful requires either Xα[59] or Fenske–Hall calculations of model complexes; Fenske and co-workers successfully modeled the ^{13}C chemical shift of metal carbenes and alkyls[60] and ^{11}B chemical shifts in metalloboranes.[61] However, due to three factors, we have an extremely fortunate situation here in which to apply a simplified chemical shielding analysis: large chemical shielding anisotropy, local C_{2v} symmetry for the dimetallacyclopropane unit, and published results of molecular orbital calculations. These three factors facilitate a correlation between chemical shielding and chemical bonding. The correlation requires two main components. First, the paramagnetic contribution to the chemical shielding elements is related to the energies of the bonding and antibonding orbitals and the appropriate angular momentum operators as was done in eq 2.2 for the chemical shielding tensor element directed along the y-axis. Second, a molecular orbital diagram for a dimetallacyclopropane unit is prepared on the basis of the best available information.

In a parameter-free Fenske–Hall calculation of (μ-CH_2)(μ-CO)[FeCp(CO)]$_2$, Bursten and Cayton determined the energies of molecular bonding and antibonding orbitals derived from the a_1 and b_1 frontier orbitals of the methylene unit; the relative energies of three out of the four orbitals are given in Figure 2 of their paper:

$a_1 \leftrightarrow b_1 = 3.2$ eV and $a_1 \leftrightarrow b_1^* = 9.2$ eV.[4a] The other necessary orbital energies are $a_1 = -14.47$, $a_1^* = -2.27$, b_2 (C–H) = -26.15, b_2^* (C–H) = 53.25 eV; only the highest occupied and lowest lying virtual orbital energies are given here.[62] We note here the reported tendency for Fenske–Hall calculations to spread the energy levels of ligand orbitals.[63] That feature is not important here as only orbital energy ordering and approximate spacings are required for the qualitative analysis of the chemical shielding tensor.

In Figure 2.7, the energies of molecular orbitals with significant methylene carbon atomic p orbital contribution are shown. The energies for cyclopropene are taken from the results of an SCF–HF calculation with a double-ξ basis set.[64] The energies for the dimetallacyclopropane unit are taken from the work of Bursten and Cayton with the assumptions listed above. The dashed lines between the two systems illustrate the evolution of the methylene carbon atomic p orbitals between the two bonding environments. The vertical double-headed arrows indicate the nonzero angular momentum integrals that contribute to the chemical shielding, analogous to eq 2.2. The experimental chemical shielding elements in the indicated coordinate system for both cyclopropene[65] and the dimetallacyclopropane unit (this work) are given above the respective manifolds.

Cyclopropene represents the typical situation where there is no apparent qualitative correlation between the chemical shielding elements and the reciprocal of differences among the orbital energies. We conclude that there is no single element of the chemical shielding tensor that is large enough to make the gross approximations inherent in eq 2.2 valid.

However, for the dimetallacyclopropane unit, there is a strong qualitative correlation between the largest element of the chemical shielding tensor and the close energy spacing among molecular orbitals composed of carbon atomic p_x and p_z

orbitals. There is a very large paramagnetic contribution to the chemical shielding tensor element directed along the y-axis as shown in Figure 2.7 and detailed here:

$$\sigma_{yy}^{total}(TMS) = \sigma_{yy}^{dia} + \sigma_{yy}^{para} = \sigma_{yy}^{dia} + k\left[\frac{1}{\left(a_1^* - b_1\right)} + \frac{1}{\left(b_1^* - a_1\right)}\right] = 372.3\ (6)\ ppm \qquad (2.11)$$

Thus, we conclude that the frontier orbital analysis indicated in Chart I is consistent with the NMR results for the major orientation of the chemical shielding tensor.

The simplified chemical shielding analysis is clearly of limited utility. For example, the orbital energy levels of the dimetallacyclopropane unit suggest that σ_{xx} and σ_{yy} should be nearly equal. Again, it is apparent that one element of the chemical shielding tensor must be very large so that the approximations leading to eq 2.2 are made valid. Alternatively, there may be a significant error in the orbital energy spacings in Figure 2.7, most likely in the placement of a_1* (see above).

We now turn to a brief discussion of the charge on the methylene carbon and possible inferences from the chemical shielding data. Generally, it is the diamagnetic contribution to the chemical shielding tensor that is most relevant to questions of charge.[66] In the case of axial symmetry, the paramagnetic contributions cancel for $\sigma_{||}$ and a fiducial value the diamagnetic contribution of –90 ppm was found for sp–hybridized carbon sites.[26,67] Since the methylene unit lacks axially symmetry, the most negative chemical shielding element, which is along the x-axis, is likely to have both paramagnetic and diamagnetic contributions. Therefore, σ_{xx}^{dia} may range anywhere from –17.6 (6) ppm to –90 ppm to even some much more negative value, if there should be a large negative charge on the methylene carbon. Very roughly, the σ_{xx}^{dia} term should change by about –65 ppm or greater for an additional unit of negative charge.[68] A second unknown is whether there is a change in the radial distribution

function of the carbon orbitals between the bridging methylene site and axially symmetric sites for which the fudical mark of $\sigma_{||} = -90$ ppm was determined. Thus, we can draw no conclusions from the chemical shielding data regarding the charge on carbon.

2.6. Conclusions

The complete orientation of the chemical shielding tensor has been obtained for a methylene unit in an organometallic complex. The determination was based upon the local symmetry of the methylene site (two orthogonal mirror planes) and the asymmetric dipolar coupling tensor due to the two methylene protons. The strength of the dipolar interaction was used to measure the methylene geometry: d(C–H) = 1.096 (3) Å (corrected for vibrational effects) and ∠H–C–H = 110.8 (4)°. The sample consisted of two crystallographic forms of *cis*-(μ-$^{13}CH_2$)(μ-CO)[FeCp(CO)]$_2$. For the triclinic form, the chemical shielding tensor elements are: $\sigma_{11} = 372.3$ (6) (perpendicular to the dimetallacyclopropane ring), $\sigma_{22} = 82.1$ (1) (bisects the two hydrogens of the CH_2 unit), and $\sigma_{33} = -17.6$ (6) ppm (TMS) (parallel to the Fe–Fe bond axis). The elements of the monoclinic form are very similar: $\sigma_{\alpha\alpha}^{mono} = \sigma_{\alpha\alpha}^{tri} - 6.6$ ppm ($\alpha = 1, 2, 3$).

The principal elements of the chemical shielding tensor are correlated, using a simplified chemical shielding analysis, with the published results of a Fenske–Hall molecular orbital calculation. On the basis of the symmetry and relative energies of the bonding and antibonding orbitals, the largest paramagnetic chemical shielding tensor element is predicted to be perpendicular to the plane of the dimetallacyclopropane unit, in excellent agreement with the experimental observation. However, the limitations of the simplified chemical shielding analysis are quite obvious on two counts: First, an incorrect prediction is made for the two paramagnetic chemical shielding elements in the plane of the dimetallacyclopropane unit. Second, the diamagnetic chemical shielding

elements are not determined from the simplified analysis; thus, no information is available regarding charge on the methylene carbon.

For several reasons, this study of a $^{13}CH_2$ unit provides a textbook example for a simple analysis of the paramagnetic contribution to the chemical shielding tensor.

(1) Because of the C_{2v} symmetry, the otherwise complex angular momentum integrals of the chemical shielding interaction can be dealt with by using the Levi–Civita rules.

(2) Because two of the carbon p orbitals participate in C–Fe bonds and one in the much stronger C–H bonds,[69] there is a conveniently large separation between sets of bonding and antibonding carbon valence orbitals. Therefore, one element of the chemical shielding tensor has a much large paramagnetic contribution than the other two.

(3) The dipolar coupling interaction allows not only the assignment of the chemical shielding tensor orientation, but also the determination of local molecular geometry ("nanoscopic MRI").

An extension of this work, NMR sensitivity permitting,[70] is the qualitative prediction and observation of surface bound species. The detection of bridging methylene units on surfaces has been particularly difficult.[71] Given that various aspects of the problem are already known in some detail, bonding[72] and Knight shift,[73] it should be possible to qualitatively predict some aspects of the chemical shielding tensor for a surface bound species.

Acknowledgments. The support of the National Science Foundation (CHE–8715517) is gratefully acknowledged. The purchase of the Bruker MSL 200 NMR spectrometer was made possible by NSF grant CHE–8711788. Useful discussions with R. W. Hall, N. R. Kestner, B. E. Bursten, G. G. Stanley, E. T. Samulski, D. G. Cory, and A. N. Garroway are gratefully acknowledged. Leslie G. Butler is a Fellow of the Alfred P. Sloan Foundation (1989-91).

Note Added in Proof. A recent compilation by Duncan[74] nicely clarifies the issue of chemical shift scales. To make our labels consistent with Duncan's, change σ to δ except for eq 2.4.

Figure 2.1.

Calculated proton-coupled ^{13}C powder patterns for the six possible relative orientations of the chemical shielding tensor with respect to the dipolar coupling tensor for a methylene site with local C_{2v} symmetry. Important parameters in these calculations are: σ_{11} = 378.9, σ_{22} = 67.5, σ_{33} = –29.4 ppm (TMS), d(C–H) = 1.1 Å, ∠H–C–H = 109.5°, $\nu(^{13}C)$ = 50.301 MHz, and Lorenztian line broadening 3 kHz.

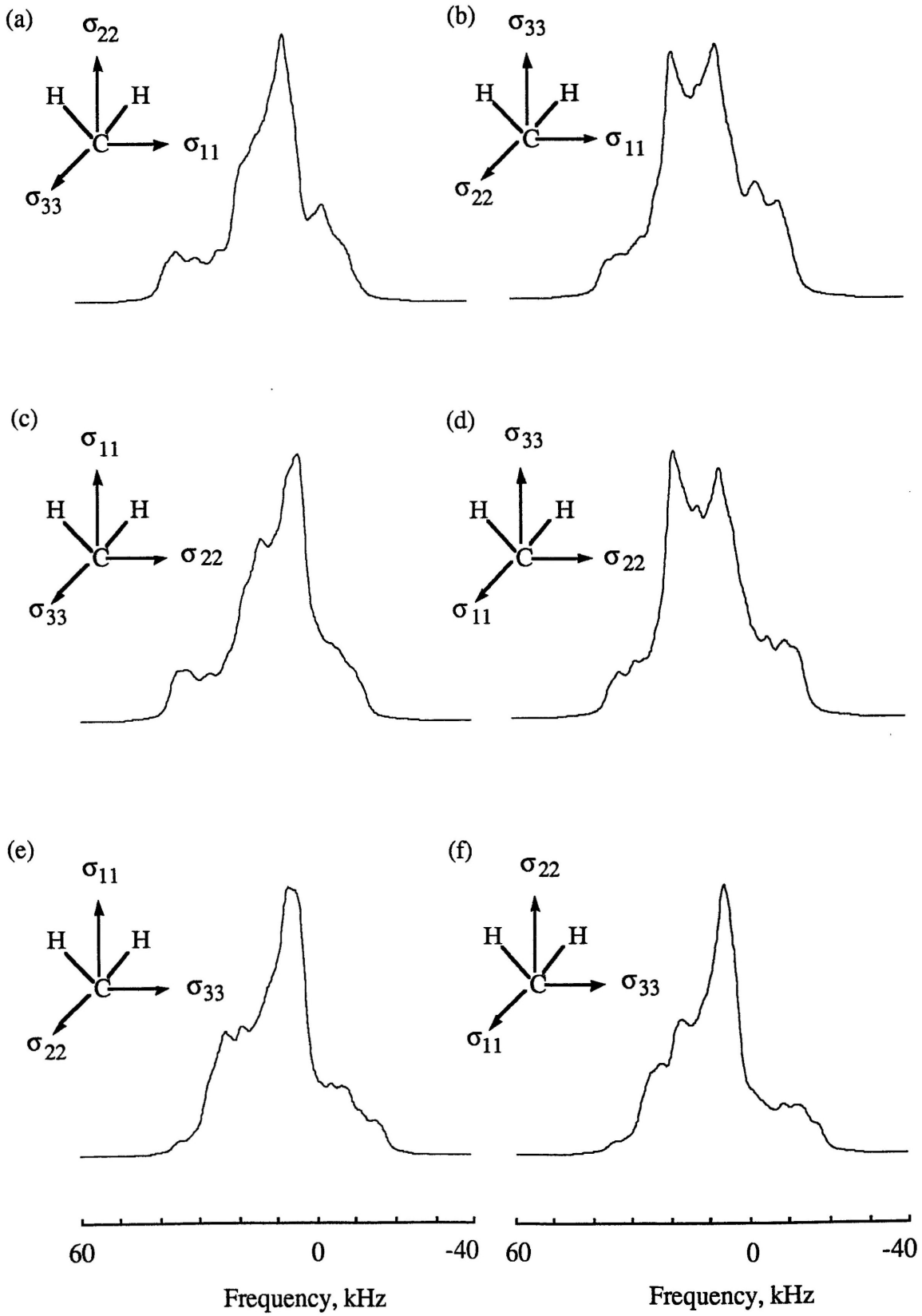
(a)
σ22
H
H
C
σ11
σ33
(b)
σ33
H
H
C
σ11
σ22
(c)
σ11
H
H
C
σ22
σ33
(d)
σ33
H
H
C
σ22
σ11
(e)
σ11
H
H
C
σ33
σ22
(f)
σ22
H
H
C
σ33
σ11
60
0
-40
Frequency, kHz
60
0
-40
Frequency, kHz

Figure 2.2.

Solid-state NMR spectra: (a) proton-decoupled ^{13}C chemical shielding powder pattern for *cis*- (μ-$^{13}CH_2$)(μ-CO)[FeCp(CO)]$_2$, cross polarization time of 5 ms was used at a field strength corresponding to a ^1H 90° pulse of 5 μs; (b) ^{13}C chemical shielding powder pattern for *cis*-(μ-CO)$_2$[FeCp(CO)]$_2$ showing the powder pattern for the cyclopentadienyl carbons; (c) CP/MAS spectrum of a 60:40 mixture of triclinic and monoclinic *cis*-(μ-$^{13}CH_2$)(μ-CO)[FeCp(CO)]$_2$; ν_R = 4.98 kHz, solid-state isotropic chemical shifts for the bridging methylene carbon are 145.6 and 139.0 ppm (TMS) for the triclinic and monoclinic forms, respectively, other resonances are at 87.8 ppm for the cyclopentadienyl carbons and 284.4 and 212.5 ppm for the bridging and terminal carbonyls, respectively.

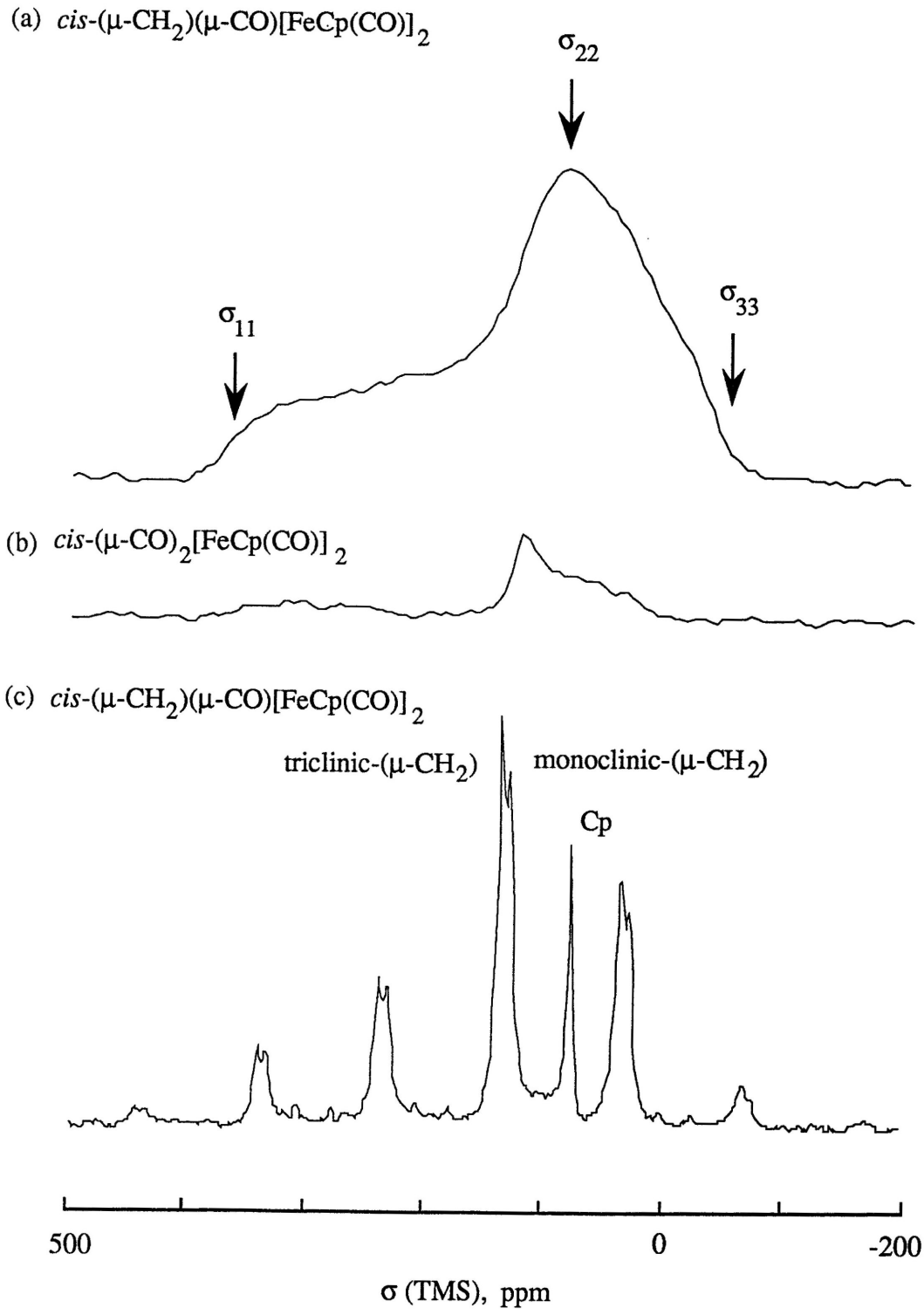
(a) cis-(μ-CH2)(μ-CO)[FeCp(CO)]2
σ22
σ11
σ33
(b) cis-(μ-CO)2[FeCp(CO)]2
(c) cis-(μ-CH2)(μ-CO)[FeCp(CO)]2
triclinic-(μ-CH2)
monoclinic-(μ-CH2)
Cp
500
0
-200
σ (TMS), ppm

Figure 2.3.

Results from a nonlinear least-squares analysis of the proton-decoupled ^{13}C chemical shielding powder pattern of a 60:40 mixture of triclinic and monoclinic *cis*-(μ-$^{13}CH_2$)(μ-CO)[FeCp(CO)]$_2$: (a) experimental ^{13}C chemical shielding powder pattern; (b) best calculated fit, with 1 kHz of Lorenztian line broadening, to the experimental spectrum and the corresponding residuals (c). The fit is composed of three components as shown in (d). The three components of the fit are the methylene carbons of monoclinic form (···), the triclinic form (---), and the cyclopentadienyl carbons (–·–). The deviation at about 380 ppm may be due to finite pulse length effects.

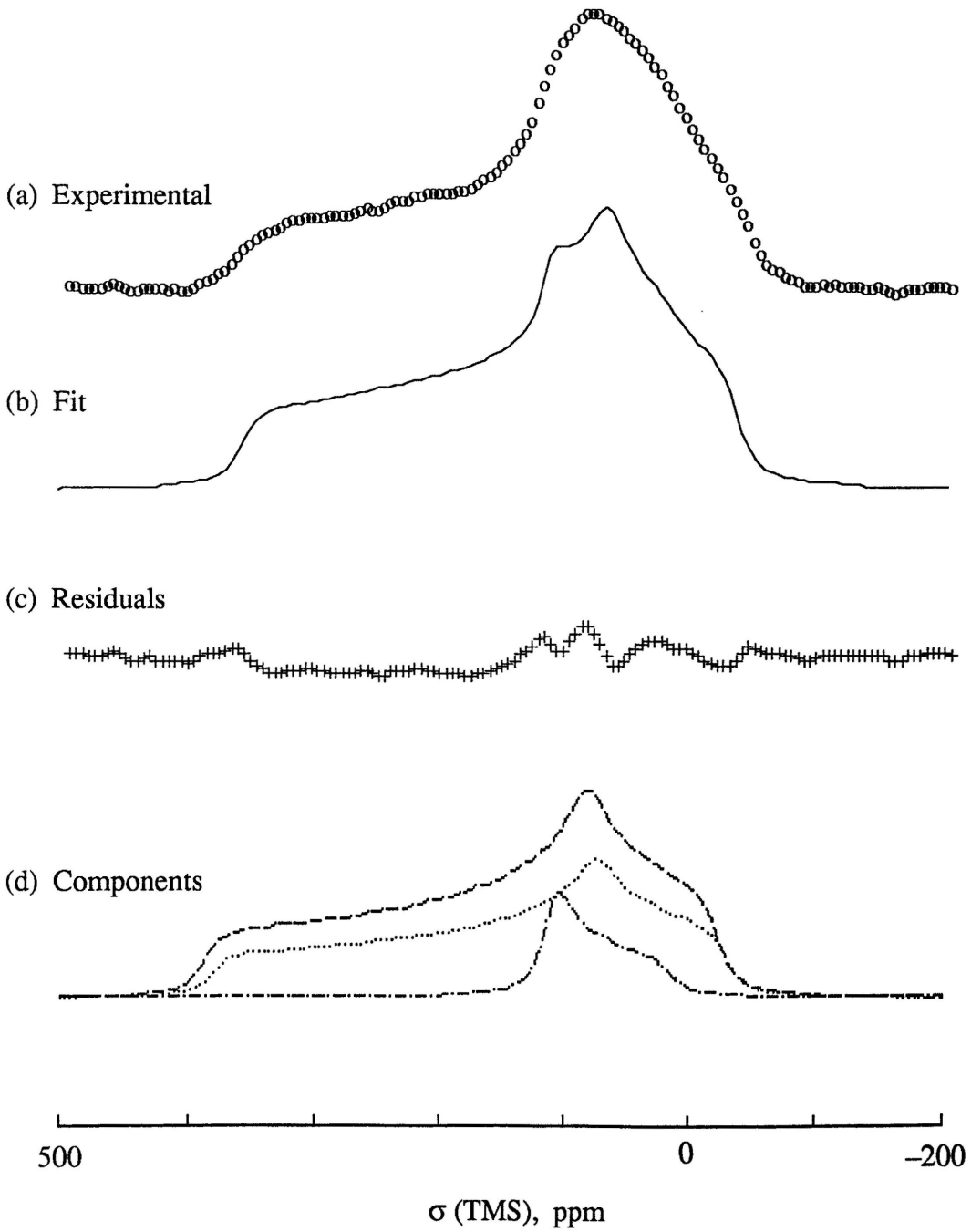
(a) Experimental
(b) Fit
(c) Residuals
(d) Components
500
0
–200
σ (TMS), ppm

Figure 2.4.

Traces show the calculated intensities of a central band and related spinning sidebands based on a Herzfeld–Berger analysis of the CP/MAS experiment. The solid traces are based on the monoclinic form with $\sigma_{11} = 365.7$, $\sigma_{22} = 75.5$, $\sigma_{33} = -24.2$ ppm. The experimental central and sideband intensities of the monoclinic form are indicated as with an asterisk. The data for the triclinic form are shown as a circle by making the assumption that $\sigma_{\alpha\alpha}^{tri} = \sigma_{\alpha\alpha}^{mono} + 6.6$ ppm ($\alpha = 1, 2, 3$). The dotted lines are to indicate the precision of this experiment and are shown for ±20 ppm variations in $\sigma_{33} - \sigma_{22}$ and $\sigma_{iso} - \sigma_{11}$. Spin rates range from 5 to 10 kHz; below 5 kHz, there was interference from the Cp ring spinning sideband pattern.

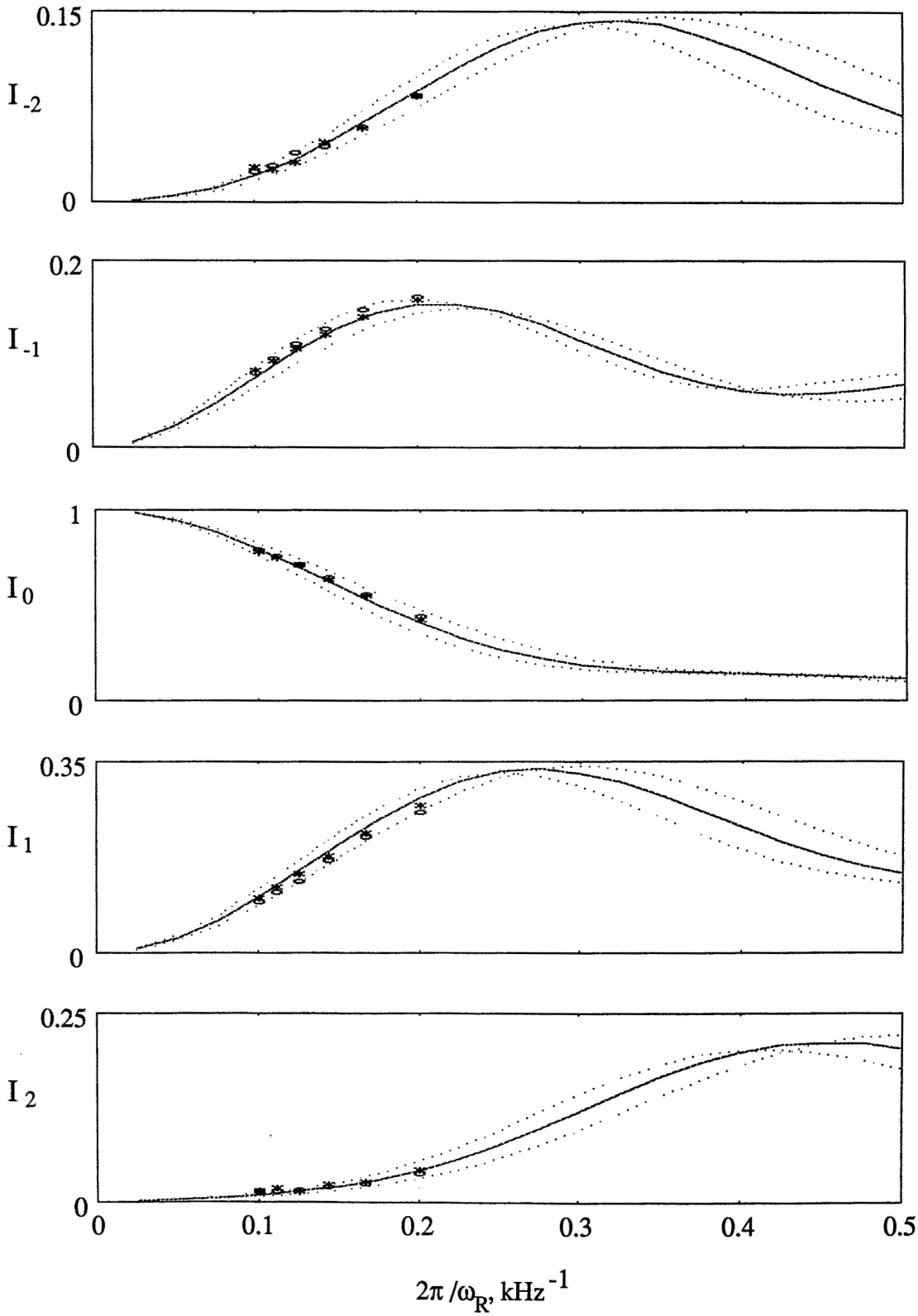
0.15
I -2
0
0.2
I -1
0
1
I 0
0
0.35
I 1
0
0.25
I 2
0
0
0.1
0.2
0.3
0.4
0.5
2π /ω R, kHz -1

Figure 2.5.

Results from a nonlinear least-squares analysis of the proton-coupled ^{13}C powder pattern of *cis*-(μ-$^{13}CH_2$)(μ-CO)[FeCp(CO)]$_2$ with the orientation shown in Figure 1a: (a) The experimental proton-coupled ^{13}C powder pattern, cross polarization time of 5 ms was used at a field strength corresponding to a ^1H 90° pulse of 5 μs; (b) best calculated fit, with 3 kHz of Lorenztian line broadening, to the experimental spectrum, $\chi^2_\nu = 2.7$ with a step angle of 2°, fit is composed of two components, the methylene carbons of the monoclinic and triclinic forms; (c) residual, negative deviation at about 800 ppm may be due to finite pulse length effects.

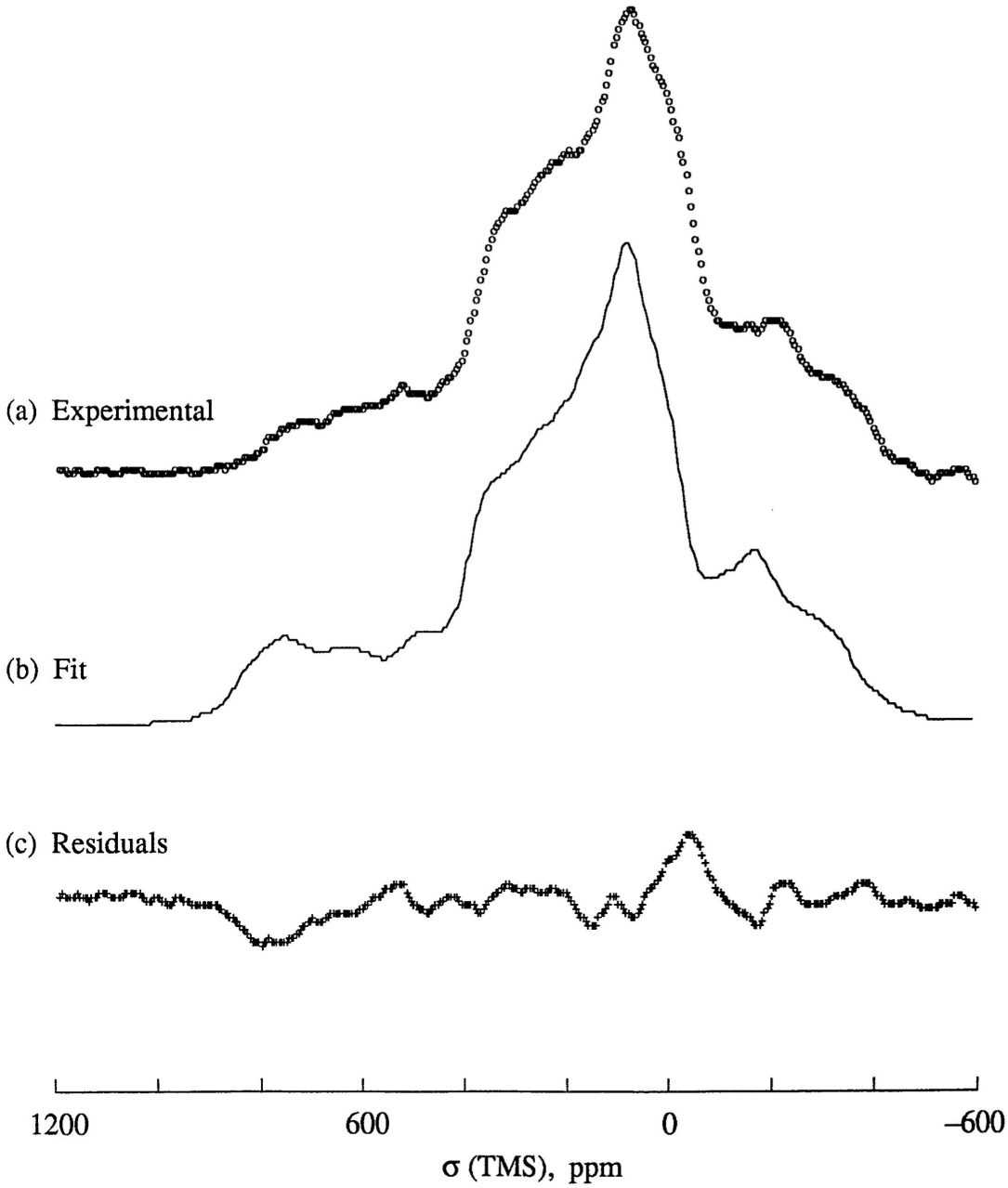
(a) Experimental
(b) Fit
(c) Residuals
1200
600
0
–600
σ (TMS), ppm

Figure 2.6.

Calculated (a) and experimental (b) 2D separated local field spectra of *cis*-(μ-$^{13}CH_2$)(μ-CO)[FeCp(CO)]$_2$. The pulse sequence of Linder *et al.* was used with a 5 μs 90° ^{1}H pulse and evolution with 141 kHz off resonance decoupling.[16] Also shown are the calculated and experimental dipolar projections along the F1 dimension. The calculated results are obtained with the same chemical shielding tensor elements and orientation as used for the 1D simulation in Figure 2.5.

(a) Calculated

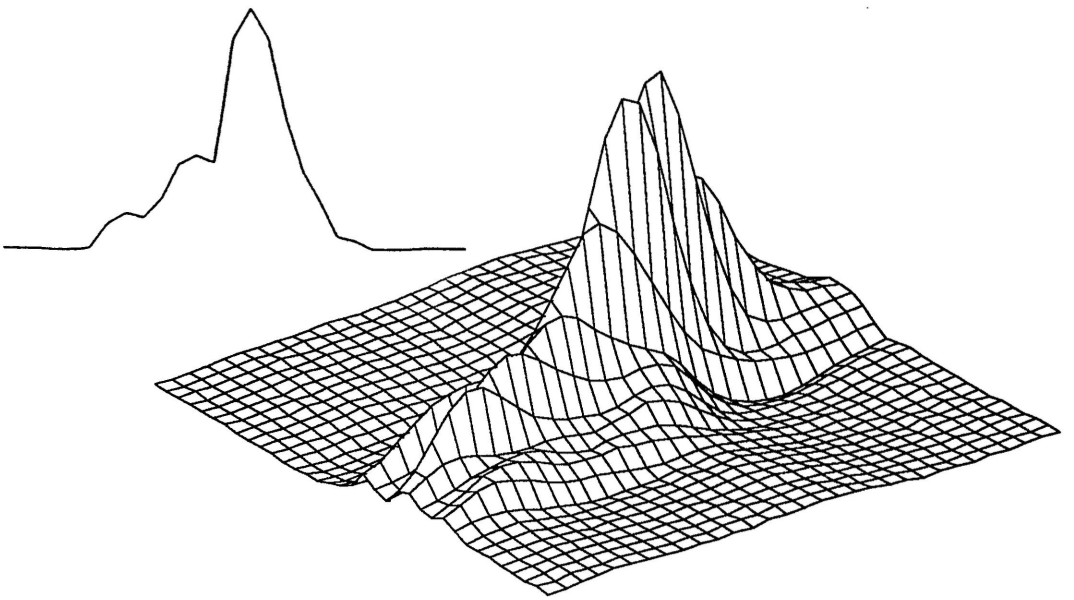

(b) Experimental

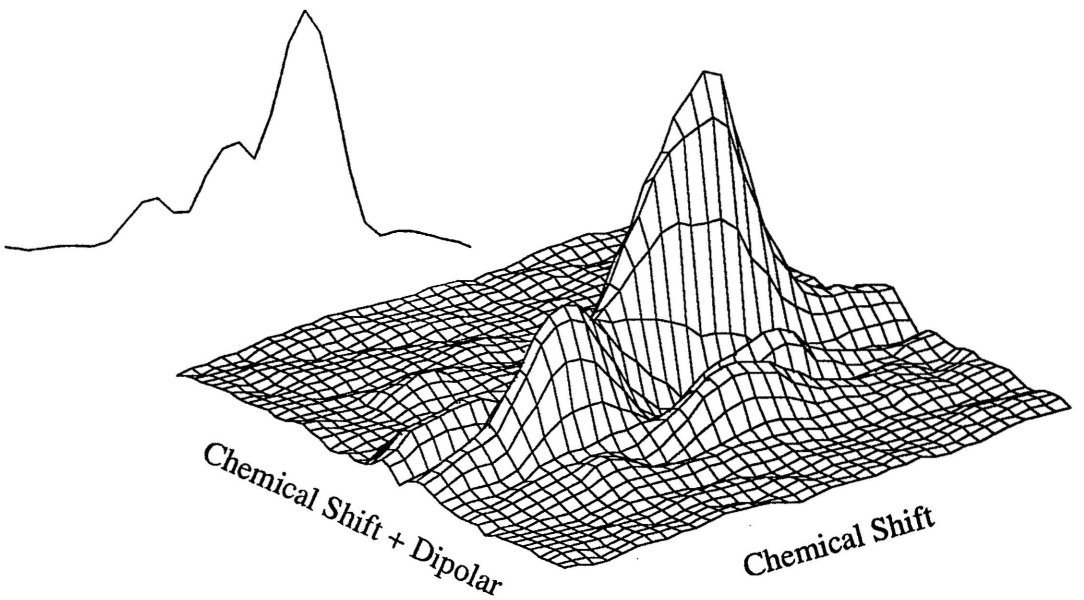

Figure 2.7.

Molecular orbital correlation diagram for cyclopropene and a dimetallocylcopropane unit. The orbital energies for cyclopropene are from an SCF–HF calculation with a double-ξ basis set; the axis system shown for cyclopropene is the same as used in the calculation.[64] The chemical shielding tensor elements for cyclopropene are listed above the manifold.[65] The orbital energies for the dimetallocyclopropane unit are taken, in part, from the results of a Fenske–Hall calculation of *cis*-(μ-CH_2)(μ-CO)[FeCp(CO)]$_2$;[4a] the energy scale and reference for the Fenske–Hall calculation are different than those of the SCF–HF work. In particular, the energy of the C–H antibonding orbital is, as expected, anomalously high;[63] however, that is not a problem for this qualitative analysis. The chemical shielding tensor elements listed above the manifold are from this work rewritten in the coordinate system defined by cyclopropene. The dashed lines connecting orbitals of the two manifolds indicate the evolution of atomic p orbitals on the methylene carbon. The vertical double-headed arrows indicate nonzero contributions to the paramagnetic chemical shielding interaction. The length of each arrow represents the inverse of the magnitude of the contribution as detailed in eq 2.2.

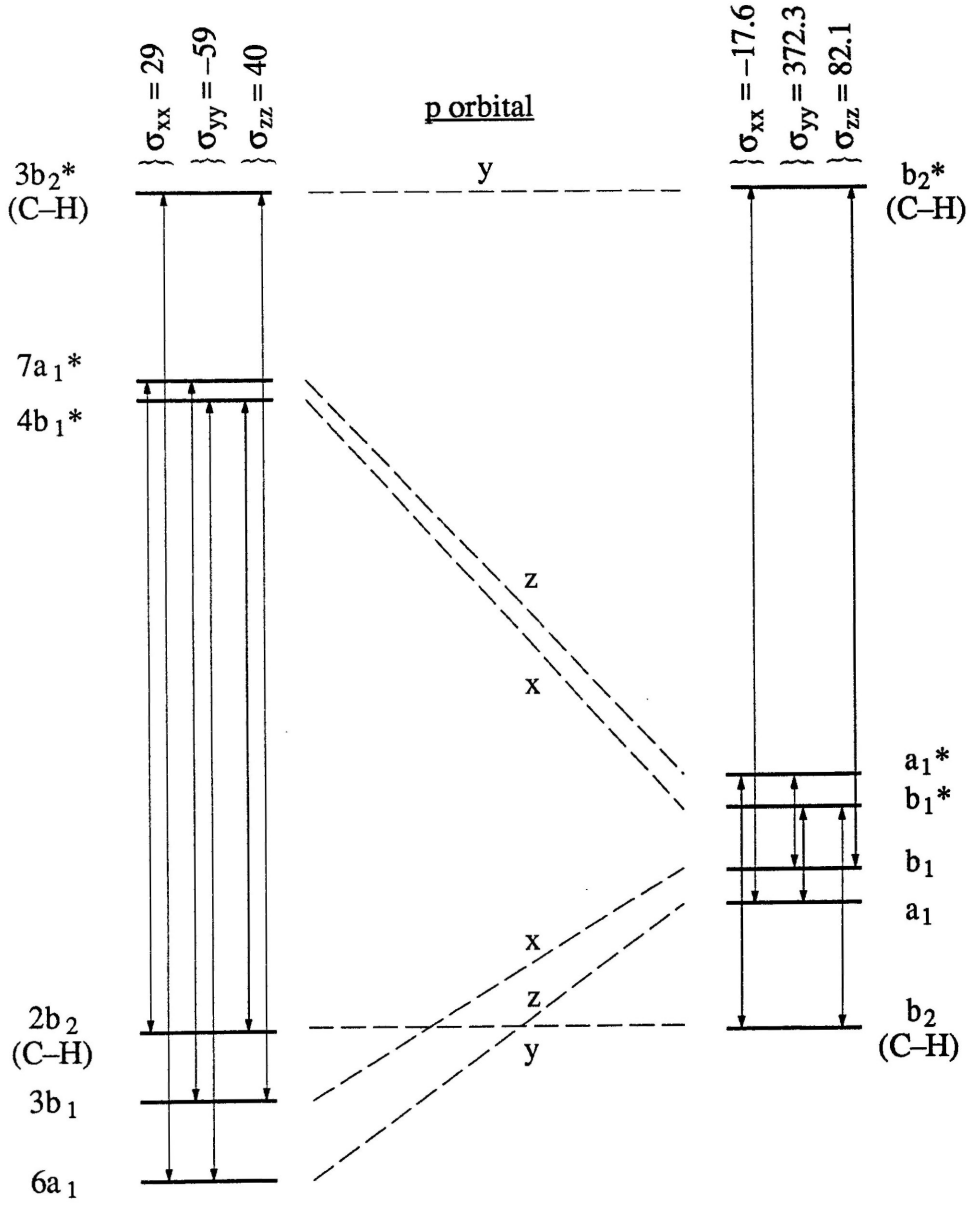
σxx = 29
σyy = –59
σzz = 40
p orbital
σxx = –17.6
σyy = 372.3
σzz = 82.1
3b2* (C–H)
y
b2* (C–H)
7a1*
4b1*
z
x
a1*
b1*
b1
a1
x
z
y
2b2 (C–H)
3b1
6a1
b2 (C–H)

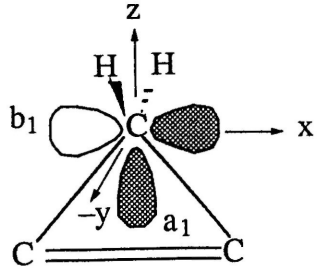
z
H
H
b1
C
x
–y
a1
C
C

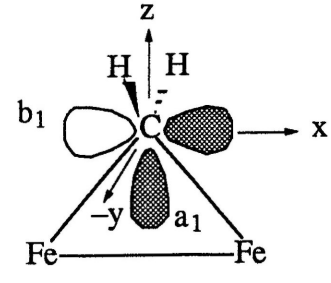
z
H
H
b1
C
x
–y
a1
Fe
Fe

References for Chapter 2

(1) Herrmann, W. A. *Advan. Organomet. Chem.* **1982**, *20*, 159-263.

(2) Casey, C. P.; Gable, K. P.; Roddick, D. M. *Organometallics* **1990**, *9*, 221-6.

(3) Casey, C. P.; Fagan, P. J.; Miles, W. H. *J. Am. Chem. Soc.* **1982**, *104*, 1134-6.

(4) (a) Bursten, B. E.; Cayton, R.H. *J. Am. Chem. Soc.* **1987**, *109*, 6053-9.
(b) Bursten, B. E.; Cayton, R. H. *Polyhedron* **1988**, *7*, 943-54.

(5) Xiang, S. F.; Chen, H. W.; Eyermann, C. J.; Jolly, W. L.; Smit, S. P.; Theopold, K. H.; Bergman, R. G.; Herrmann, W. A.; Pettit, R. *Organometallics* **1982**, *1*, 1200-3.

(6) Altbach, M. I.; Hiyama, Y.; Gerson, D. J.; Butler, L. G. *J. Am. Chem. Soc.* **1987**, *109*, 5529-31.

(7) (a) Hofmann, P. *Angew. Chem., Int. Ed. Engl.* **1979**, *18*, 554-6.
(b) Calabro, D. C.; Lichtenberger, D. L.; Herrmann, W. A. *J. Am. Chem. Soc.* **1981**, *103*, 6852-5.
(c) Bursten, B. E.; Cayton, R.H. *J. Am. Chem. Soc.* **1986**, *108*, 8241-9.

(8) Veeman, W. S. *Prog. Nucl. Magn. Reson. Spectrosc.* **1984**, *16*, 193-235.

(9) Duncan, T. M. *J. Phys. Chem. Ref. Data* **1987**, *16*, 125-51.

(10) Mass, W. E. J. R.; Ketgens, A. P. M.; Veeman, W. S. *J. Chem. Phys.* **1987**, *87*, 6854-8.

(11) Herzfeld, J.; Roberts, J. E.; Griffin, R. G. *J. Chem. Phys.* **1987**, *86*, 597-602.

(12) Hartzell, C. J.; Pratum, T. K.; Drobny, G. *J. Chem. Phys.* **1987**, *87*, 4324-31.

(13) Teng, Q.; Cross, T. A. *J. Magn. Reson.* **1989**, *85*, 439-47.

(14) Hiyama, Y.; Niu, C.-H.; Silverton, J. V.; Bavoso, A.; Torchia, D. A. *J. Am. Chem. Soc.* **1988**, *110*, 2378-83.

(15) (a) Opella, S. J.; Waugh, J. S. *J. Chem. Phys.* **1977**, *66*, 4919-24.
(b) Rybaczewski, E. F.; Neff, B. L.; Waugh, J. S.; Sherfinski, J. S. *J. Chem. Phys.* **1977**, *67*, 1231-6.

(16) Linder, M.; Höhener, A.; Ernst, R. R. *J. Chem. Phys.* ***1980***, *73*, 4959-70.

(17) Duijvestijn, M. J.; Manenschijn, A.; Smidt, J.; Wind, R. A. *J. Magn. Reson.* **1985**, *64*, 461-9.

(18) Chu, P. J.; Gerstein, B. C. *J. Chem. Phys.* **1989**, *91*, 2081-101.

(19) Munowitz, M.; Huang, T.-H.; Griffin, R. G. *J. Chem. Phys.* **1987**, *86*, 4362-8.

(20) Stoll, M. E.; Vega, A. J.; Vaughan, R. W. *J. Chem. Phys.* **1976**, *65*, 4093-8.

(21) Zilm, K. W.; Beeler, A. J.; Grant, D. M.; Michl, J.; Chou, T.-C.; Allred, E. L. *J. Am. Chem. Soc.* **1981**, *103*, 2119-20.

(22) Alderman, D. W.; Solum, M. S.; Grant, D. M. *J. Chem. Phys.* **1986**, *84*, 3717-25.

(23) (a) Oas, T. G.; Drobny, G. P.; Dahlquist, F. W. *J. Magn. Reson.* **1988**, *78*, 408-24.
(b) Hyde, J. S.; Pasenkiewicz-Gierula, M.; Basosi, R.; Froncisz, W.; Antholine, W. E. *J. Magn. Reson.* **1989**, *82*, 63-75.

(24) VanderHart, D. L. *J. Chem. Phys.* **1976**, *64*, 830-4.

(25) Gleeson, J. W.; Vaughan, R. W. *J. Chem. Phys.* **1983**, *78*, 5384-92.

(26) Beeler, A. J.; Orendt, A. M.; Grant, D. M.; Cutts, P. W.; Michl, J.; Zilm, K. W.; Downing, J. W.; Facelli, J. C.; Schindler, M. S.; Kutzelnigg, W. *J. Am. Chem. Soc.* **1984**, *106*, 7672-6.

(27) Ando, I.; Webb, G. A. *Theory of NMR Parameters*; Academic Press: New York, 1983.

(28) Dykstra, C. E. *Ab Initio Calculation of the Structures and Properties of Molecules*; Elsevier: New York, 1988.

(29) Derived from ref 27, eq 3.14.

(30) Facelli, J.C.; Grant, D. M.; Michl, J. *Acc. Chem. Res.* **1987**, 20, 152-8.

(31) Jameson, C. J.; De Dios, A.; Jameson, A. K. *Chem. Phys. Lett.* **1990**, *167*, 575-82.

(32) (a) Nakatsuji, H.; Nakao, T.; Kanda, K. *Chem. Phys.* **1987**, *118*, 25-32.
(b) Nakatsuji, H.; Nakao, T. *Chem. Phys. Lett.* **1990**, *167*, 571-4.
(c) Nakatsuji, H.; Sugimoto, M. *Inorg. Chem.* **1990**, *29*, 1221-5.

(33) Pople, J. A. *Mol. Phys.* **1964**, *7*, 301-6.

(34) Gerstein, B. C.; Dybowski, C. R. *Transient Techniques in NMR of Solids*; Academic Press: New York, 1985.

(35) Karplus, M.; Pople, J. A. *J. Chem. Phys.* **1963**, *38*, 2803-7.

(36) (a) Chisholm, M. H.; Godleski, S. *Prog. Inorg. Chem.* **1976**, *20*, 299-436.
(b) Jameson, C. J.; Mason, J. In *Multinuclear NMR*, Mason, J., Ed.; Plenum: New York, 1987; Chapt. 3 and references therein.

(37) Haeberlen, U. *High Resolution NMR in Solids*; Academic Press: New York, 1976.

(38) Ditchfield, R.; Ellis, P. D. in *Topics in Carbon-13 NMR Spectroscopy*, Levy, G. C., Ed.; John Wiley & Sons,: New York, 1974; Vol. I, p. 1-51.

(39) Zare, R. N. *Angular Momentum*; Wiley-Interscience: New York, 1988.

(40) Goldstein, H. *Classical Mechanics*, 2nd ed.;Addison-Wesley: New York, 1980. Note error in eq B-3y.

(41) (a) Korswagen, R.; Alt, R.; Speth, D.; Ziegler, M. L. *Angew. Chem. Int. Ed. Engl.* **1981**, *20*, 1049-51.
(b) Altbach, M. I. Ph.D. Thesis, Louisiana State University, 1988.

(42) Altbach, M. I.; Muedas, C. A.; Korswagen, R. P.; Ziegler, M. L. *J. Organomet. Chem.* **1986**, *306*, 375-83.

(43) Altbach, M. I.; Fronczek, F. R.; Butler, L. G. *Acta Cryst. Sect C* submitted.

(44) Pines, A.; Gibby, M. G.; Waugh, J. S. *J. Chem. Phys.* **1973**, *59*, 569-90.

(45) (a) Kermit Distribution, Columbia University Center for Computing Activities, 612 West 115th St., New York, NY 10025.
(b) Casey, P. K.; Jarrett, W. L.; Mathias, L. J. *American Laboratory* **1989**, *21*, March, 25-35.

(46) Michaels, D. C.; Kim, A. J.; Perilloux, B. C.; Barksdale, D.; Butler, L. G., *Comp. Chem.* submitted.

(47) LabVIEW, National Instruments Corp., 6504 Bridge Point Parkway, Austin TX 78730.

(48) Matlab. The Mathworks Inc., 24 Prime Parkway, Natick, MA 01760.

(49) (a) Bevington, P. R. *Data Reduction and Error Analysis for the Physical Sciences*; McGraw-Hill: New York, 1969.
(b) Press, W. H.; Flannery, B. P.; Teukolsky, S. A.; Vetterling, W. T. *Numerical Recipes*; Cambridge University Press: Cambridge, 1986.

(50) Result of the best non linear least squares fit of the spectrum shown in Figure 2.2b.

(51) (a) Griffin, R. G. *Methods in Enzymology* **1981**, *72*, 108-74.
(b) Levitt, M. H.; Suter, D.; Ernst, R. R. *J. Chem. Phys.* **1986**, *84*, 4243-55.

(52) Herzfeld, J.; Berger, A. E. *J. Chem. Phys.* **1980**, *73*, 6021-30.

(53) Altbach, M. I.; Hiyama, Y.; Wittebort, R. J.; Butler, L. G. *Inorg. Chem.* **1990**, *29*, 741-7.

(54) See for example: Roberts, J. E.; Harbison, G. S.; Munowitz, M. G.; Herzfeld, J. Griffin, R. G. *J. Am. Chem. Soc.* **1987**, *109*, 4163-9.

(55) Henry, E. R.; Szabo, A. *J. Chem. Phys.* **1985**, *82*, 4753-61.

(56) Diehl, P. In *Nuclear Magnetic Resonance of Liquid Crystals*, Emsley, J. W., Ed.; D. Reidel: Boston; Chapt. 7.

(57) Takusagawa, F.; Fumagalli, A.; Koetzle, T. F.; Herrmann, W. A. *Inorg. Chem.* **1981**, *20*, 3060-4.

(58) Schultz, A. J.; Williams, J. M.; Calvert, R. B.; Shapley, J. R.; Stucky, G. D. *Inorg. Chem.* **1979**, *18*, 319-23.

(59) Freier, D. G.; Fenske, R. F.; You, X.-Z. *J. Chem. Phys.* **1985**, *83*, 3526-37.

(60) Fenske, R. F. In *Organometallic Compounds*, Shapiro, B. L., Ed.; Texas A&M University Press: College Station, TX, 1983; p. 305-33.

(61) Fehlner, T. P.; Czech, P. T.; Fenske, R. F. *Inorg. Chem.* **1990**, *29*, 3103-9.

(62) Bruce E. Bursten, private communication.

(63) Bursten, B. E.; Cotton, F. A.; Stanley, G. G. *Isr. J. Chem.* **1980**, *19*, 132-42.

(64) Snyder, L. C.; Basch, H. *Molecular Wave Functions and Properties*; John Wiley & Sons: New York, 1972.

(65) Zilm, K. W.; Conlin, R. T.; Grant, D. M.; Michl, J. *J. Am. Chem. Soc.* **1980**, *102*, 6672-6.

(66) (a) Wu, W.-X; You, X.-Z; Dai, A.-B.; Jing, S.-P. *Polyhedron* **1990**, *9*, 1849-54.
(b) Bodner, G. M.; Todd, L. J. *Inorg. Chem.* **1974**, *13*, 1335-8.

(67) Pople, J. A. *Proc. R. Soc. London, Ser. A* **1957**, *239*, 541-9.

(68) Malli, G.; Froese, C. *Int. J. Quantum Chem.* **1967**, *1S*, 95-8.

(69) Collman, J. P.; Hegedus, L. S.; Norton, J. R.; Finke, R. G. *Principles and Applications of Organotransition Metal Chemistry*; University Science Books: Mill Valley, CA, 1987, Table 6.1.

(70) See for example: Pruski, M.; Kelzenberg, J. C.; Gerstein, B. C.; King, T. S. *J. Am. Chem. Soc.* **1990**, *112*, 4232-40.

(71) Albert, M. R.; Yates, Jr., J. T. *The Surface Scientist's Guide to Organometallic Chemistry*; American Chemical Society: Washington, D.C., 1987.

(72) (a) Zheng, C.; Apeloig, Y.; Hoffmann, R. *J. Am. Chem. Soc.* **1988**, *110*, 749-74.
(b) Hoffmann, R. *Rev. Mod. Phys.* **1988**, *60*, 601-28.

(73) (a) Wang, P.-K.; Slichter, C. P.; Sinfelt, J. H. *Phys. Rev. Lett.* **1984**, *53*, 82-5.
(b) Ansermet, J.-P.; Wang, P.-K.; Slichter, C. P.; Sinfelt, J. H. *Phys. Rev. B* **1988**, *37*, 1417-28.

(74) Duncan, T. M. *A Compilation of Chemical Shift Anisotropies*; Farragut Press: Chicago, 1990.

CHAPTER 3

Deuterium Quadrupole Coupling Constants and Asymmetry Parameters in Bridging Metal Hydride Complexes‡

by
Ae Ja Kim,[1a] Frank R. Fronczek,[1a] Leslie G. Butler*,†,[1a]
Shixiong Chen,[1b] and Ellen A. Keiter*[1b]

Contribution from the Department of Chemistry
Louisiana State University, Baton Rouge, Louisiana 70803-1804 and
the Department of Chemistry Eastern Illinois University, Charleston, Illinois, 61920

*To whom correspondence should be addressed.
†Fellow of the Alfred P. Sloan Foundation (1989-1991).
‡Keyword index: solid-state ^2H NMR, bridging metal hydrides,
^2H quadrupole coupling constant

Abstract

The deuterium quadrupole coupling constants and the asymmetry parameters for six bridging metal hydrides, $[Et_4N][^2HCr_2(CO)_{10}]$, $[(Ph_3P)_2N][^2HCr_2(CO)_{10}]$, $[Ph_4P][^2HCr_2(CO)_{10}]$, $[Et_4N][^2HW_2(CO)_{10}]$, $[(Ph_3P)_2N][^2HW_2(CO)_{10}]$, and $[Ph_4P][^2HW_2(CO)_{10}]$, were determined from the Levenberg–Marquardt nonlinear least-squares fit of the solid-state deuterium NMR powder patterns. The quadrupole coupling constant (absolute value) varies from 54.1 (8) to 90.4 (2) kHz; the asymmetry parameter ranges from 0.027 (3) to 0.31 (2). The relationships between the quadrupole coupling constant and M–H bond length and between the asymmetry parameter and the M–H–M bond geometry are discussed on the basis of a point charge model. In order to assess motional averaging at the deuterium site, the temperature dependence of the ^2H NMR spectrum for two bridging metal hydrides was examined at 140, 200, and 300 K. In addition, the isotropic chemical shifts have been obtained from ^1H CRAMPS. These NMR results are highly pertinent to NMR spectroscopy of adsorbed hydrogen on metal surfaces. The solid-state structure of $[Ph_4P][^2HCr_2(CO)_{10}]$ has been determined by X-ray diffraction.

3.1. Introduction

The M–H–M bond in the $[HM_2(CO)_{10}]^-$ monoanion (M = Cr, Mo, W) has been of considerable interest because it contains a single unsupported three-center bond.[2-6] Unlike the linear hydrogen bonds found in KHF_2 [7] and $Na[Me_3Al–H–AlMe_3]$ [8-10], the bridging metal hydride bonds in these transition metal dimers are bent [11-15], even when the metal carbonyl framework has a pseudo D_{4h} geometry, as shown in Figure 3.1a for $[Et_4N][HCr_2(CO)_{10}]$ [11]. The metal carbonyl framework is sensitive to the counter-ion with a bent staggered geometry being relatively common [3,4,11-15], as shown in Figure 3.1b. Metal hydrides are common species on surfaces and may often exist in a bridging environment [16,17].

Solid-state deuterium NMR techniques have previously been used to characterize the terminal metal hydride sites in $(\eta_5\text{-}C_5H_5)_2Mo(^2H)_2$[18], $(\eta_5\text{-}C_5H_5)_2W(^2H)_2$[18], $(\eta_5\text{-}C_5H_5)_2Zr(^2H)_2$[19], and $^2HMn(CO)_5$[20], and to determine the charge on a carbon atom in an organometallic alkyl complex [21]. Recently, dynamic information about the rotational jump motion for the cyclopentadienyl ring in $(\mu\text{-}CO)_2[FeCp(CO)]_2$ was obtained from deuterium line shape analyses and T_1 measurements.[22]

Deuterium quadrupole coupling constants have been measured in a wide variety of bridging hydrogen sites: K^2HF_2,[7,23] O-^{2}H···O in $CuSO_4\cdot5H_2O$,[24] and many other hydrogen bonds with oxygen atom donors and acceptors;[24-26] and N-^{2}H···O in anthranilic acid[27] and other systems involving nitrogen atom donors and/or acceptors[28,29]. Also, relatively accurate calculations can be made using *ab initio* molecular orbital techniques and extended basis sets. One possibility revealed by the results of calculations is that of a negative quadrupole coupling constant, either in a nonlinear site, as in diborane[30-34], or for a particularly long, symmetric linear hydrogen bond[25].

In this work we are trying to obtain structural information on the M-^{2}H-M unit in the $[^2HM_2(CO)_{10}]^-$ monoanion (M = Cr, W) by using solid-state deuterium NMR spectroscopy. This quest is based on the fact that the solid-state deuterium NMR spectrum of a powder is determined by two measurable parameters[35], the quadrupole coupling constant and the asymmetry parameter, which describe the principal elements of the electric field gradient tensor[36]. The quadrupole coupling constant is a measure of the magnitude of the electric field gradient at the deuterium site while the asymmetry parameter gives information about the shape of the electric field gradient; for example, an asymmetry parameter of zero suggests at least 3-fold symmetry at deuterium. Consequently, both parameters will be related to the M–H bond distance and the M–H–M bond angle.

3.2. Theory

For the calculation of the deuterium powder pattern NMR line shape, the total Hamiltonian is given by a combination of Zeeman and quadrupolar interactions,

$$H_{\text{total}} = -\gamma H_o(1 + \sigma_{iso})\mathbf{I}_z + H_Q \tag{3.1}$$

where γ is the gyromagnetic ratio for deuterium, 2π x 653.5 rad s^{-1} G^{-1}, H_o is the applied magnetic field, **I** is the deuterium spin angular momentum operator in the laboratory coordinate system, and σ_{iso} is the isotropic chemical shift relative to TMS. The quadrupole coupling Hamiltonian for a nucleus with $I \geq 1$ is given by[35]

$$H_Q = \frac{eQ/\hbar}{6I(2I-1)} \sum_{k,j} V_{kj}^{Lab} \left[\frac{3}{2}(\mathbf{I}_k\mathbf{I}_j + \mathbf{I}_j\mathbf{I}_k) - \delta_{kj}\mathbf{I}^2\right] \tag{3.2}$$

where Q is the nuclear quadrupole moment, 2.86×10^{-27} cm^2 for deuterium[37] and δ_{kj} is the kronecker delta. The electric field gradient, V_{kj} (=eq_{kj}), can be described as a symmetric 3x3 traceless tensor with the convention $|eq_{zz}| \geq |eq_{yy}| \geq |eq_{xx}|$.[36] The

magnitude of the electric field gradient tensor is given by the quadrupole coupling constant, $e^2q_{zz}Q/h$. The deviation from axial symmetry is indicated by the asymmetry parameter, η:

$$\eta = \frac{eq_{yy} - eq_{xx}}{eq_{zz}} \quad (0 \leq \eta \leq 1) \tag{3.3}$$

In the principal axis system, the electric field gradient tensor can be reduced to two parameters, eq_{zz} and η:

$$V^{PA} = -\frac{eq_{zz}}{2}\begin{bmatrix} (1-\eta) & 0 & 0 \\ 0 & (1+\eta) & 0 \\ 0 & 0 & -2 \end{bmatrix} \tag{3.4}$$

The transformation between the laboratory coordinate system (Lab) and the molecular coordinate system (PA) is accomplished with direction cosine matrices[38] using the y-convention[39]:

$$V^{Lab} = \mathbf{R}_N^{-1}(\theta)\,\mathbf{R}_z^{-1}(\chi)V^{PA}\,\mathbf{R}_z(\chi)\mathbf{R}_N(\theta) \tag{3.5}$$

Only two Euler angles, θ and χ, are needed to orient the electric field gradient tensor relative to the applied magnetic field, H_o.

The transition frequencies are obtained by solving the eigenvalue problem for H_{total} at a given orientation, θ and χ. There are two allowed transitions among the deuterium spin states: $|+1\rangle \rightarrow |0\rangle$ and $|0\rangle \rightarrow |-1\rangle$. Thus, the deuterium powder patterns are obtained by summing the deuterium transition frequencies over a range of θ and χ orientations within the limits of 0 and 90° with sin θ weighting[40]. Typically, we use a uniform step angle of 2° and the calculation takes about 10 minutes on a VAXstation 3200. At the temperatures and the magnetic fields used here, the shape of the deuterium powder pattern does not depend upon the sign of the quadrupole coupling

constant, thus, the sign can not be determined. However, at extreme conditions, for example, 0.02 K and 18 T, Boltzmann statistics do affect the line shape such that the sign can be obtained, provided a small tip angle rf pulse is used[41].

The elements of the electric field gradient tensor are the sum of nuclear and electronic terms, the latter is expressed as an expectation value of the electronic wavefunction Ψ,

$$eq_{zz} = +\sum_n K_n \frac{3z_n^2 - r_n^2}{r_n^5} - e\left\langle \Psi^* \left| \sum_i \frac{3z_i^2 - r_i^2}{r_i^5} \right| \Psi \right\rangle \qquad (3.6)$$

where e is the electronic charge, n is the index over the other nuclei whose charge is K_n, and i is the index over the electrons of the molecule. Molecular wavefunctions suitable for use in eq 3.6 can be obtained from *ab initio* SCF–HF calculations provided extended basis sets are used.[30-32] In the absence of detailed molecular wavefunctions, an approximate analysis is often feasible using point charges to represent the combined nuclear and electronic contributions from neighboring atoms. Thus, at the bridging deuteron, two point charges representing the metals will produce an electric field gradient along the z-axis (PA)

$$\frac{e^2 q_{zz} Q}{h} = \left(\frac{e^2 Q}{h}\right)(2K')\left(\frac{3z^2 - r^2}{r^5}\right) = \left(\frac{e^2 Q}{h}\right)(2K')\left(\frac{3\sin^2(\theta/2) - 1}{r^3}\right) \qquad (3.7)$$

where r is the M–H bond length, θ is the M–H–M bond angle, and z is along the M···M vector. Analogous expressions apply for eq_{xx} and eq_{yy}. The adjustable parameter, K', was determined from the experimental quadrupole coupling constant for $[Et_4N][^2HCr_2(CO)_{10}]$ at 300 K and has a value of +1.104 e, with the assumption that the sign of the quadrupole coupling constant is positive.[42] Due to the $1/r^3$ distance dependence, charges close to the origin have the greatest effect on the electric field gradient. With this model, the effects of structural variations in a static nonlinear

bridging metal hydride on the values of the quadrupole coupling constant and the asymmetry parameter can be assessed, as shown in Figure 3.2. Early on, a deficiency in the point charge model was found; an exaggerated dependence of the asymmetry parameter on the bond angle is apparent on comparison with the experimental results. Therefore, also shown in Figure 3.2b are the results from a set of *ab initio* molecular orbital calculations for a model system, $[Na–H–Na]^+$.[43]

3.3. Experimental Methods

3.3.1. Sample Preparation. Bridging metal hydrides, $[Et_4N][HCr_2(CO)_{10}]$, $[(Ph_3P)_2N][HCr_2(CO)_{10}]$, $[Ph_4P][HCr_2(CO)_{10}]$, $[Et_4N][HW_2(CO)_{10}]$, $[(Ph_3P)_2N][HW_2(CO)_{10}]$, and $[Ph_4P][HW_2(CO)_{10}]$, were synthesized from $Cr(CO)_6$ or $W(CO)_6$ and $NaBH_4$ according to the method described by Hayter for the tetraethylammonium salt.[44] For preparation of the bis(triphenylphosphine)iminium and tetraphenylphosphonium salts, $[(Ph_3P)_2N]Cl$ and $[Ph_4P]Cl$ were substituted for $[Et_4N]Br$. Identical methods were utilized for preparing the deuterated complexes except that $NaBD_4$ was used as the reducing agent. All reactants were reagent grade and were used as obtained from commercial sources without further purification. Purity of products was established by infrared spectroscopy. In cases where spectra of the initial product showed evidence of contamination by $M(CO)_6$, recrystallization from either ethanol or tetrahydrofuran/hexane was effected until all infrared evidence of starting material had been eliminated. Solution ^1H NMR data were recorded with a Varian T–60 spectrometer in deuteroacetone solutions.

3.3.2. Crystallographic Work for $[Ph_4P][^2HCr_2(CO)_{10}]$. Diffraction data were collected on an Enraf-Nonius CAD4 diffractometer equipped with Mo Kα radiation and a graphite monochromator. Data reduction included corrections

for Lorentz, polarization, background, and absorption effects. Absorption corrections were based on Ψ scans. The structure was refined by full-matrix least squares based on F. Calculations using the Enraf-Nonius SDP programs.[45] Non-hydrogen atoms were refined anisotropically; the bridging hydride was refined isotropically, while hydrogens bound to carbon were placed in calculated positions. Crystal, experimental, and refinement data are given in Table 3.1. Atomic positions are listed in Table 3.2. Selected bond distances and bond angles are listed in Table 3.3. Figure 3.1b shows the atom-labeling scheme for the $[^2HCr_2(CO)_{10}]^-$ anion in $[Ph_4P][^2HCr_2(CO)_{10}]$.

3.3.3. Solid-State Deuterium NMR Spectroscopy. Deuterium powder patterns were collected at 30.709 MHz on a Bruker MSL200 solid-state NMR spectrometer. A static wideline probe was used and ~ 200mg of sample was packed into a 5 mm glass sample holder. The spectra for $[Et_4N][^2HCr_2(CO)_{10}]$ and $[Ph_4P][^2HCr_2(CO)_{10}]$ were obtained at 140, 200, and 300 K and the others only at 300 K. In order to prevent the O-ring seals about the bore tube of the superconducting magnet from freezing during the 140 K experiment, a continuous room temperature nitrogen gas flow through the magnet bore was used. (We know of two cases where O-ring failure has lead to loss of vacuum in the Dewar and subsequent quenching of the superconducting magnet.) The spectra for $[Et_4N][^2HCr_2(CO)_{10}]$ showed some frequency shifts at lower temperatures; the spectrum acquired at 200 K exhibited an apparent isotropic shift of 180 ppm downfield relative to the 300 K spectrum. This shift is three times larger than the exponential line broadening and may have been due to a temperature dependent probe magnetic susceptibility and/or a paramagnetic impurity in the sample.

The quadrupolar echo pulse sequence was used: $(90_{x,-x} - \tau_1 - 90_y - \tau_2 - acq_{x,-x})$.[46] The 90° pulse length was 3 μs. The first delay between 90° pulses, τ_1, was 25 or 120 μs and the second delay before echo acquisition, τ_2, was 26.5 or 121.5 μs. Delays of 120 and 121.5 μs were used only for

$[(Ph_3P)_2N][^2HW_2(CO)_{10}]$ to remove a zero frequency spike possibly associated with a deuterated contaminant. A relaxation delay of 60 or 120 s was used. A two-step phase-cycling procedure, where the phase of the first 90° pulse and the receiver phase are alternated between 0° and 180°, was used in order to cancel the effects of probe ringing.[47]

Exponentially filtered (2 kHz), Fourier-transformed, and manually-phased spectra were transferred as binary files from the Bruker Aspect-3000 computer to a Macintosh II computer via an RS-232 serial connection and the KERMIT file transfer program. Conversion from binary to ASCII data files was done with a program[48] written in LabVIEW, a graphical programming language.[49] Spectral simulation programs were written in Matlab, a vector-oriented programming language.[50] The Levenberg–Marquardt nonlinear least-squares algorithm[51,52] was recoded in Matlab and used in a program to fit an experimental spectrum with a simulated line shape where the variables include the deuterium quadrupole coupling constant and the asymmetry parameter. The quality of the fit is judged to be good if no systematic deviations are observed in a plot of the residuals and the value of χ^2_ν is approximately one.

3.3.4. ^{1}H CRAMPS. ^{1}H CRAMPS NMR spectra were recorded at 187 MHz on a modified Nicolet NT–200 spectrometer.[53] The BR–24 pulse sequence was utilized,[54] with pulse widths and τ values of 1.26 μs and 3.0 μs, respectively. Samples (ca. 50 mg) were packed into 5 mm (2 mm i. d.) NMR tubes and were spun at the magic angle at a rate of 1.5 kHz. Each spectrum was accumulated with twenty repetitions and 512 data points. Chemical shifts were measured relative to tetrakis(trimethylsilyl)methane (δ = 3.75 ppm) and are reported relative to tetramethylsilane (TMS).

3.4. Results

Figure 3.1b shows the X-ray crystallographic structure of the $[^2HCr_2(CO)_{10}]^-$ anion in $[Ph_4P][^2HCr_2(CO)_{10}]$. This structure is similar to, although not isomorphous with, that of the tungsten complex.[3,4] The metal carbonyl framework shows a bent staggered metal carbonyl geometry. The torsion angle defined by C13–Cr1–Cr2–C23 is –44.3 (2)°. The dihedral angle between the two planes defined by each chromium atom and the carbon atoms of its corresponding equatorial carbonyl ligands is 16.0 (4)°.

To acquire the deuterium powder patterns in these metal hydrides with acceptable signal-to-noise ratio is very difficult because of the very few deuterons in the ~ 200 mg sample and the quite long spin-lattice relaxation time, T_1. For example, the number of deuterons in 200 mg of $[Et_4N][^2HCr_2(CO)_{10}]$ is only $4x10^{-4}$ moles. The deuterium T_1 was not quantitatively measured due to the poor signal-to-noise ratio, but estimated to be 60 seconds or longer for $[Et_4N][^2HCr_2(CO)_{10}]$, based on spectra taken with different relaxation times. The spectra in Figure 3.3 required between 3000 to 6600 scans for acquisition times of 70–110 hours each.

Figures 3.3 and 3.4 show the solid-state deuterium NMR powder patterns obtained at 300 K for six bridging metal hydrides and the nonlinear least-squares fits. The spectra show that three bridging metal sites have apparent axial symmetry, $\eta \approx 0$, and the other three do not have axial symmetry, $\eta \geq 0.16$. Because of the obvious potential for motional averaging, one compound from each group, $\eta \approx 0$ and $\eta \gg 0$, was studied as a function of temperature down to 140 K. The solid-state deuterium NMR powder patterns for $[Et_4N][^2HCr_2(CO)_{10}]$ and $[Ph_4P][^2HCr_2(CO)_{10}]$ and the nonlinear least-squares fits are shown in Figure 3.4 as a function of temperature. There are minor variations in the deuterium powder patterns, but no evidence for the transformation of one spectral type into the other was found. The results of the

nonlinear least-squares fit to the deuterium powder patterns of all spectra are listed in Table 3.4.

Solid state proton NMR spectra were collected on five of the protio complexes. The spectrum for $[Et_4N][HCr_2(CO)_{10}]$ is shown in Figure 3.5 and chemical shifts (relative to TMS) for the bridging hydride sites are reported in Table 3.4. The range of chemical shifts among the complexes of each metal is quite narrow: 0.3 and 1.0 ppm for Cr and W, respectively. Inasmuch as the accuracy of the δ values obtained by the CRAMPS technique is estimated to be $\pm$ 0.2 ppm, these ranges reflect insignificant chemical shift differences among complexes of the same metal and indicate that the shielding at the bridging H is quite insensitive to M–H–M geometry and metal-carbonyl conformation. Moreover, the solid state hydride chemical shifts are nearly identical to the solution values of –19.5 and –12.5 ppm for $[HCr_2(CO)_{10}]^-$ and $[HW_2(CO)_{10}]^-$, respectively. The absence of spinning sidebands on the hydride resonances in the ^1H spectra also suggests minimal chemical shift anisotropy for these sites in the solid state.

3.5. Discussion

The interpretation of the deuterium electric field gradient parameters, the quadrupole coupling constants and the asymmetry parameters, for these bridging metal hydrides can be understood by considering three main factors:

(1) the M–H bond length,

(2) the M–H–M bond angle, and

(3) possible rapid four-site jump motion in systems with an eclipsed metal carbonyl geometry.

The magnitude of the electric field gradient, the quadrupole coupling constant, is mainly affected by the M–^{2}H bond length since the electric field gradient has a $1/r^3$ distance dependency. From the neutron diffraction results, M–H bond distances range

from 1.707 (21) to 2.070 (12) Å. To indicate this variation, two traces are shown in Figure 3.2a in which the value of the quadrupole coupling constant is plotted as a function of the M–H–M bond angle. The upper trace, having the larger quadrupole coupling constant, is computed using d(M-H) = 1.7 Å whereas the lower trace represents d(M–H) = 1.9 Å. Again, the traces shown in Figure 3.2 are computed from a simple point charge model for a symmetric M–^{2}H–M unit. A parameter in the model, K', was determined from the experimental results for $[Et_4N][^2HCr_2(CO)_{10}]$. All deuterium sites with $|e^2q_{zz}Q/h| > 80$ kHz have at least one M–H bond length of ~ 1.7 Å.

To a lesser extent, the value of the quadrupole coupling constant is affected by the M–^{2}H–M bond angle. In the point charge model, the electric field gradients due to each metal add most efficiently for a bond angle of 180°. A decrease in the M–^{2}H–M bond angle causes a decrease in the value of the quadrupole coupling constant. The two metal complexes, $[Ph_4P][^2HCr_2(CO)_{10}]$ and $[Ph_4P][^2HW_2(CO)_{10}]$, have both a relatively symmetric M–H–M unit and a small M–H–M bond angle and also have the smallest quadrupole coupling constants.

The asymmetry parameter directly reflects the M–H–M bond angle, as shown in Figure 3.2b. As discussed earlier, the point charge model apparently exaggerates the effect of nonlinearity, so results from the study of a model system, $[Na–H–Na]^+$, obtained by *ab initio* molecular orbital techniques, are also shown in Figure 3.2b.[43] The bridging metal hydride with the most acute M–^{2}H–M bond angle, $[Ph_4P][^2HW_2(CO)_{10}]$, also has the largest asymmetry parameter, $\eta = 0.31$ (2). With the exception of the highly asymmetric $[Et_4N][^2HW_2(CO)_{10}]$ complex (d(M–H) = 1.718 (12), 2.070 (12) Å), the asymmetry parameters are extremely well fit by the $[Na–H–Na]^+$ model system. The point charge model yields an exaggerated dependence of the asymmetry parameter on the M–^{2}H–M bond angle, whereas the more diffuse charge associated with the sodium cations leads to a smaller difference

between the two minor elements of the electric field gradient tensor. The largest deviation from the $[Na–H–Na]^+$ model is found for $[Et_4N][^2HW_2(CO)_{10}]$: there are two possible explanations for the deviation. First, the W–H–W unit is asymmetric[55] and has two different W–H bond lengths, thus the electric field gradient at deuterium may be similar to that of a terminal metal hydride with axial symmetry ($\eta = 0$). Second, motional effects may be important for this complex with its eclipsed metal carbonyl geometry, as discussed below. We note here that the NMR experiment is performed at 300 K whereas the neutron diffraction data were collected at 14 K. Therefore, the metal hydride NMR data may be affected by jump motions between hydride sites identified in the low temperature structure.

The last factor to consider is motional averaging of the electric field gradient due to rapid jump motion of the bridging deuteron among several different sites in the M–^{2}H–M bond. In a neutron study at 17 K of $[(Ph_3P)_2N][^2HCr_2(CO)_{10}]$,[14] four equivalent off-axis sites of the bridging deuteron were refined in a system with an eclipsed metal carbonyl geometry. Rapid jump motion among the four off-axis sites will average the two minor components, eq_{xx} and eq_{yy}, of the electric field gradient. Thus, the expected motionally averaged asymmetry parameter is zero, as may be the case here for $[Et_4N][^2HW_2(CO)_{10}]$. A near-zero asymmetry parameter indicates that the jump motion is rapid with respect to the frequency separation of the minor components of the spectrum, on the order of 10 kHz for $\eta = 0.3$ in the static limit. The $[Et_4N][^2HW_2(CO)_{10}]$ complex is an especially interesting prospect for future NMR studies at very low temperatures. Averaging the asymmetry parameter to zero would be accomplished by a four-site jump motion; a two-site jump, like that indicated in Figure 3.1a, would not be sufficient to change the value or orientation of the minor components.[56]

The temperature dependent studies do not show clear evidence for rapid four-site jump motions in either complex studied. For $[Et_4N][^2HCr_2(CO)_{10}]$, which has the eclipsed structure, the fact that the asymmetry parameter remains near zero from 300 to 140 K could be interpreted as evidence that the activation barrier to a possible four-site jump motion is small (two-site rather than four-site disorder was found in the 295 K neutron diffraction study[11]). However, analysis with the point charge model suggests that even in the static limit, the asymmetry parameter for $[Et_4N][^2HCr_2(CO)_{10}]$ will be small simply as a result of the large M–^{2}H–M bond angle. Similarly, the small asymmetry parameter for $[(Ph_3P)_2N][^2HCr_2(CO)_{10}]$ may also be due to the large M–^{2}H–M bond angle rather than motional effects.

Raman and infrared spectroscopy of bridging metal hydrides is usually done at low temperature so as to increase the spectral resolution for the metal-hydride stretching and bending modes[5,57]. The temperature-dependent line-broadening mechanism affecting Raman spectroscopy may also affect the deuterium electric field gradient tensor, as seen most clearly in the temperature dependence of the asymmetry parameter for $[Ph_4P][^2HCr_2(CO)_{10}]$. The sharp increase from $\eta = 0.162$ (6) at 300 K to $\eta = 0.23$ (1) at 140 K is seldom observed in NQR spectroscopy in the absence of a distinct phase change. It is not clear what the low temperature limit for the asymmetry parameter might be, and further experiments are planned.

Because of crystallographic disorder, one of the complexes studied, $[(Ph_3P)_2N][^2HW_2(CO)_{10}]$, has an unknown M–H–M geometry.[15] The solid state deuterium NMR parameters are similar to those found for $[Ph_4P][^2HW_2(CO)_{10}]$ and suggest a similar structure. Some refinement of the structural prediction is possible with the aid of the modified point charge model. The most likely M–H–M angle is more obtuse than for $[Ph_4P][^2HW_2(CO)_{10}]$, possibly about 135°, based upon the asymmetry parameter of 0.201 (3).

3.6. Conclusions

Solid-state deuterium NMR powder patterns were acquired for six bridging metal hydrides to obtain structural information on the M–^{2}H–M structure. The complexes studied have both eclipsed and bent staggered metal carbonyl geometries. The observed deuterium powder patterns are a result of the deuterium quadrupole coupling constant, the asymmetry parameter, and, for sites with an eclipsed metal carbonyl geometry, possible rapid four-site jump motion in the M–^{2}H–M unit. The temperature dependence of the deuterium spectrum was examined for $[Et_4N][^2HCr_2(CO)_{10}]$ and $[Ph_4P][^2HCr_2(CO)_{10}]$ which have eclipsed and bent staggered metal carbonyl geometries, respectively. The former shows little temperature dependence beyond a slight increase in the quadrupole coupling constant. Most importantly, the apparent axial symmetry of the eclipsed metal carbonyl structure was preserved to the lowest temperature studied, 140 K, but does not necessarily indicate rapid four-site jump motion. The latter complex shows a significant increase in the asymmetry parameter, possibly correlated with the same line-broadening mechanism noted in Raman and infrared spectroscopy of the bridging metal hydrides. The deuterium quadrupole coupling constants and asymmetry parameters were related to the M–H–M bond distance and the M–H–M bond angle with a point charge model and by assuming that the sign of the quadrupole coupling constant is positive.

This work shows that solid-state deuterium NMR spectroscopy has the potential to investigate structure in metal hydrides. In particular, μ_2–bridging hydrides on surfaces should have quadrupole coupling constants and asymmetry parameters similar to those found herein for metal dimers where the important factors are the M–^{2}H bond length, the M–^{2}H–M bond angle, the effective charge on the metal, and the mobility of the deuteron across a metal surface[58]. An extension to μ_3–bridging hydrides on surfaces is possible by a change in the model presented in eq 3.7; briefly, the asymmetry parameter should be zero and the z-axis of the electric field gradient aligned

along the C_3 axis of the triply bridging site. Otherwise, the same factors should again determine the deuterium NMR parameters.

Acknowledgments. The support of the National Science Foundation (CHE–8715517) is gratefully acknowledged. The purchase of the Bruker MSL 200 NMR spectrometer was made possible by NSF grant CHE–8711788. Leslie G. Butler is a Fellow of the Alfred P. Sloan Foundation (1989-1991). We gratefully acknowledge Prof. J. L. Petersen for an introductory sample of $[K(crypt–222)][^2HCr_2(CO)_{10}]$. Dr. C. E. Bronnimann and the Colorado State University Regional NMR Center, funded by National Science Foundation Grant CHE–8616437, are gratefully acknowledged for providing the ^1H CRAMPS results.

Supplementary Material Available. Listings of bond distances and angles for $[Ph_4P][^2HCr_2(CO)_{10}]$, coordinates of hydrogen atoms, table of least-squares planes for the two sets of $Cr–(C_{eq})_4$ units, table of anisotropic thermal parameters (8 pages); listing of observed and calculated structure factors (30 pages). Ordering information is given on any current masthead page.

Figure 3.1.

The flexible geometry of the M–H–M structure in the $[HM_2(CO)_{10}]^-$ anion is shown for two representative structures. (a) The metal carbonyl framework shown in an eclipsed configuration (from a neutron diffraction study of $[Et_4N][HCr_2(CO)_{10}]$, reprinted with permission from ref 11). The bridging hydride is crystallographically disordered; the Cr–H–Cr bond exhibits a bent structure. (b) The bent staggered metal–carbonyl geometry is shown here for the anion of $[Ph_4P][^2HCr_2(CO)_{10}]$ (this work).

(a) $[Et_4N][^2HCr_2(CO)_{10}]$

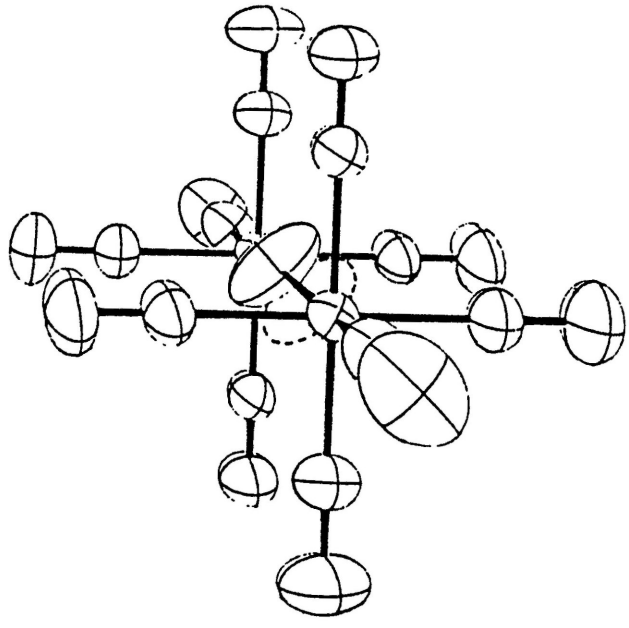

(b) $[Ph_4P][^2HCr_2(CO)_{10}]$

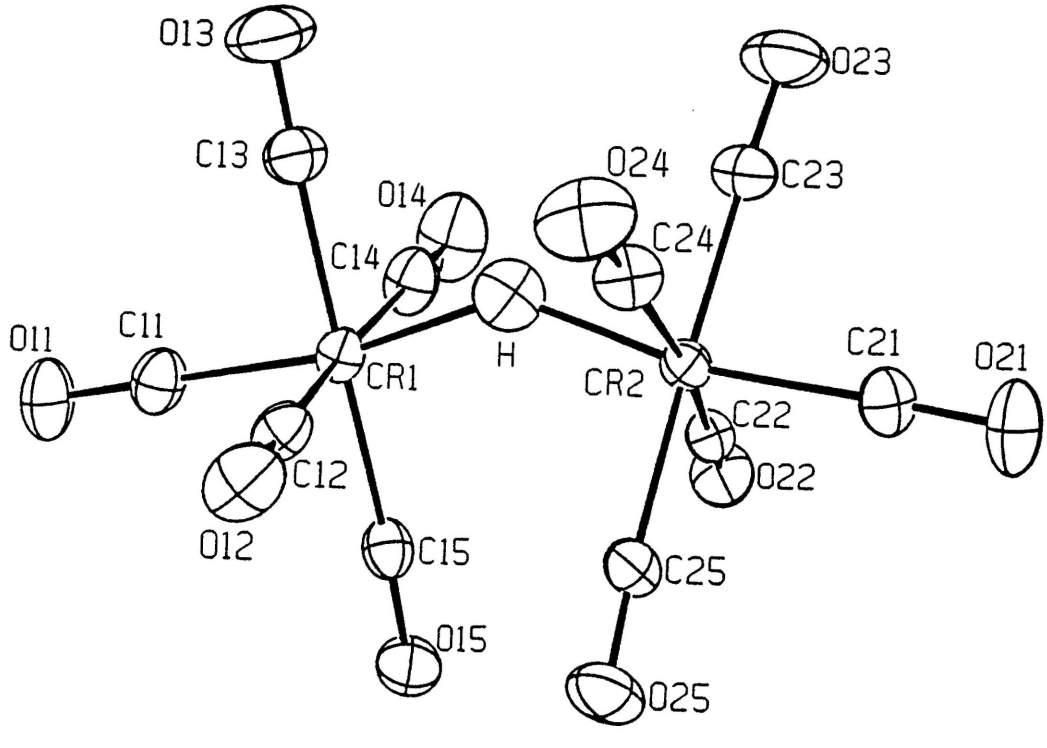

Figure 3.2.

The effect of a nonlinear, symmetric M–^{2}H–M bond on the deuterium quadrupole coupling constant and the asymmetry parameter. (a) Two traces showing the quadrupole coupling constant as a function of M–^{2}H–M bond angle for two different M–H bond lengths. The circles (o) represent the experimental deuterium quadrupole coupling constants and the labels are defined in Table 3.4. (b) The asymmetry parameter as a function of the M–^{2}H–M bond angle as computed for both a point charge model, eq 3.7, and an in *ab initio* SCF–HF calculation of a model system, $[Na–H–Na]^+$ (ref 43). In the limit of a point charge representation for the metal, the value of the asymmetry parameter does not depend upon the M–H bond length.

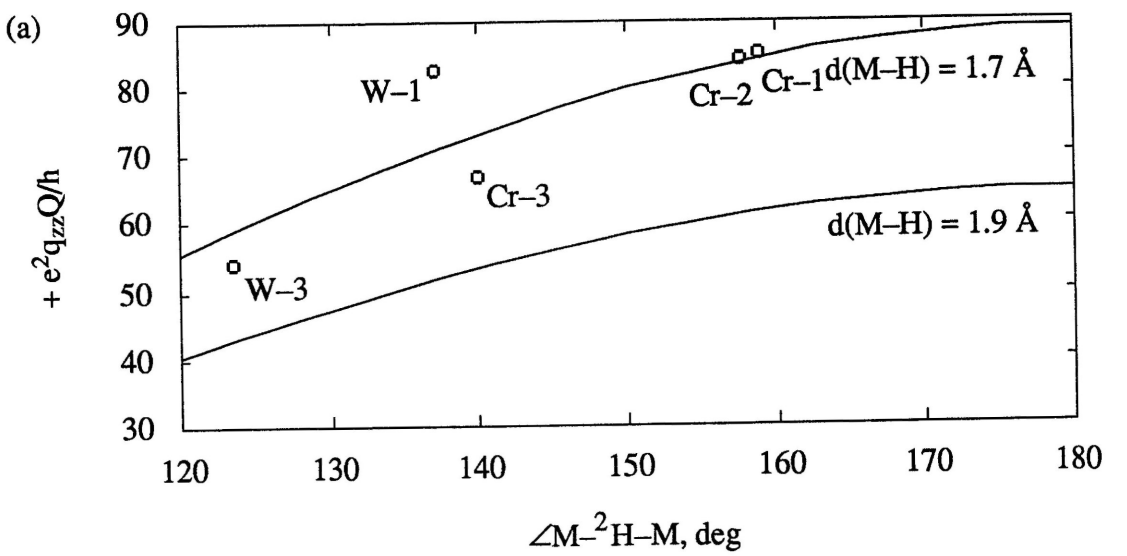
(a)
90
80
70
60
50
40
30
+ e²q_zzQ/h
W–1
Cr–2
Cr–1
d(M–H) = 1.7 Å
Cr–3
d(M–H) = 1.9 Å
W–3
120
130
140
150
160
170
180
∠M–²H–M, deg

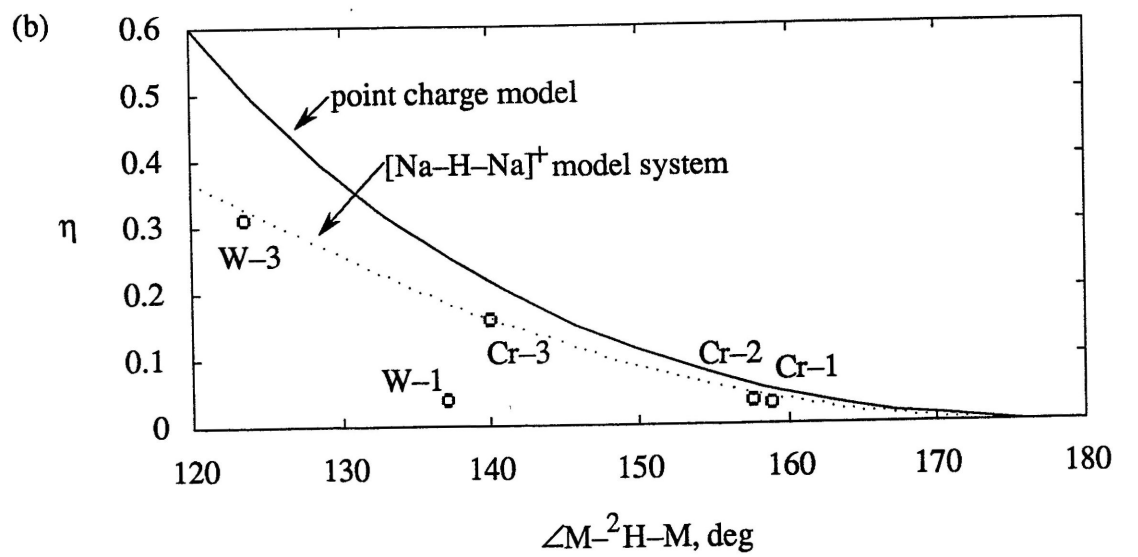
(b)
0.6
0.5
0.4
0.3
0.2
0.1
0
η
point charge model
[Na–H–Na]⁺ model system
W–3
Cr–3
Cr–2
Cr–1
W–1
120
130
140
150
160
170
180
∠M–²H–M, deg

Figure 3.3.

Solid-state deuterium NMR powder patterns obtained at 300 K for four bridging metal hydrides and the corresponding nonlinear least-squares fits. Circles (o), solid lines (–), and crosses (+) represent the experimental deuterium powder pattern, the best calculated fit, and the residual between the experimental spectrum and the fit, respectively. Experimental parameters are as follows (NS = number of scans, RD = relaxation delay):

(a) $[(Ph_3P)_2N][^2HCr_2(CO)_{10}]$, NS = 6600, RD = 60 s;

(b) $[Et_4N][^2HW_2(CO)_{10}]$, 3000, 120 s;

(c) $[(Ph_3P)_2N][^2HW_2(CO)_{10}]$, 4360, 60 s; and,

(d) $[Ph_4P][^2HW_2(CO)_{10}]$, 6520, 60 s.

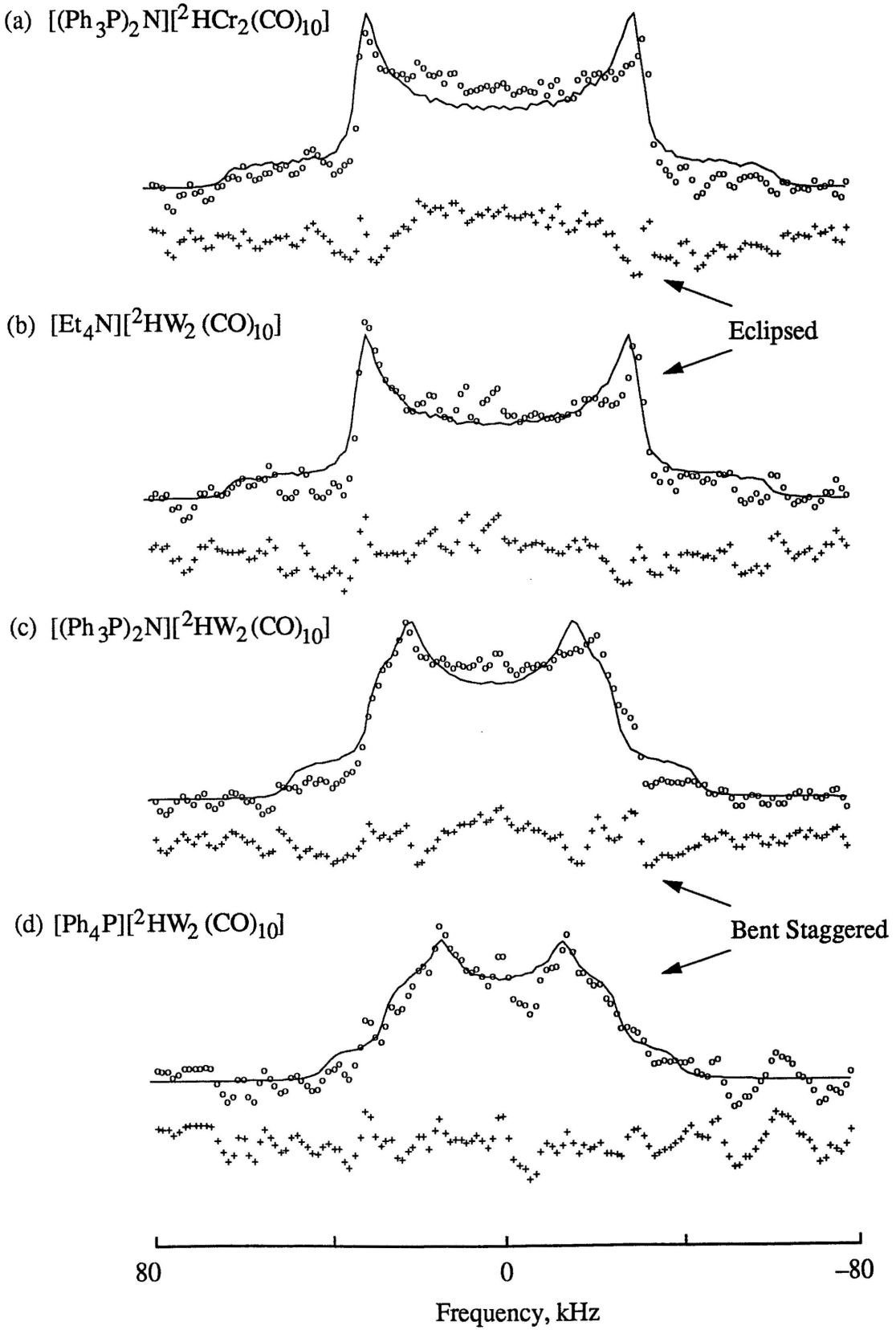
(a) [(Ph3P)2N][2HCr2(CO)10]
(b) [Et4N][2HW2 (CO)10]
Eclipsed
(c) [(Ph3P)2N][2HW2 (CO)10]
(d) [Ph4P][2HW2 (CO)10]
Bent Staggered
80
0
–80
Frequency, kHz

Figure 3.4.

Solid-state deuterium NMR powder patterns obtained for two bridging metal hydrides as a function of temperature and the corresponding nonlinear least-squares fits. Experimental parameters are as follows:

(a) $[Et_4N][^2HCr_2(CO)_{10}]$; T = 300 K, NS = 5730, RD = 60 s;
200 K, 500, 120 s; and,
140 K, 46, 120 s.

(b) $[Ph_4P][^2HCr_2(CO)_{10}]$; T = 300 K, NS = 6518, RD = 60 s;
200 K, 2150, 120 s ; and,
140 K, 156, 120 s.

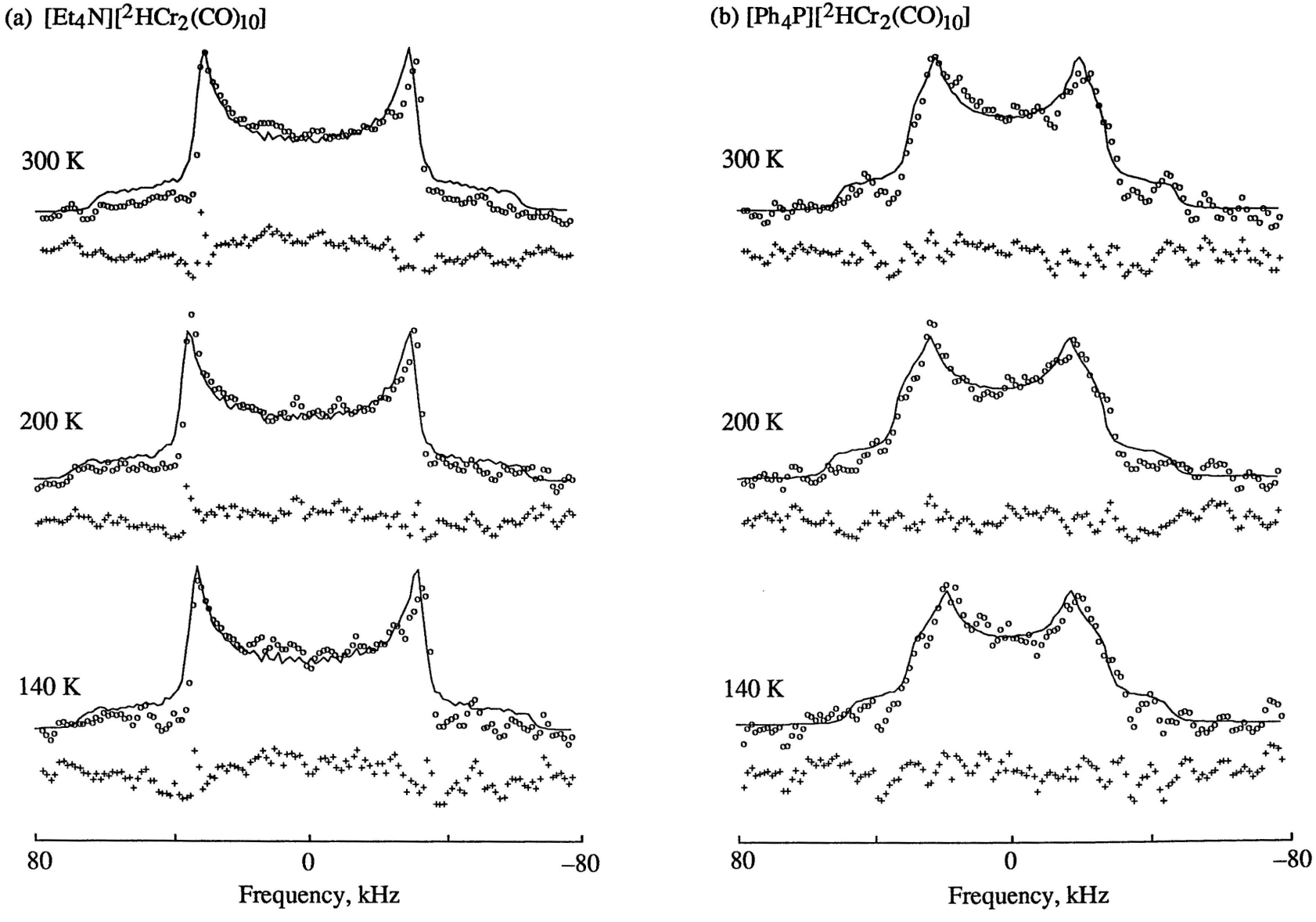
(a) [Et4N][2HCr2(CO)10]
300 K
200 K
140 K
80
0
–80
Frequency, kHz
(b) [Ph4P][2HCr2(CO)10]
300 K
200 K
140 K
80
0
–80
Frequency, kHz

Figure 3.5.

The ^{1}H CRAMPS NMR spectrum for $[Et_4N][HCr_2(CO)_{10}]$.

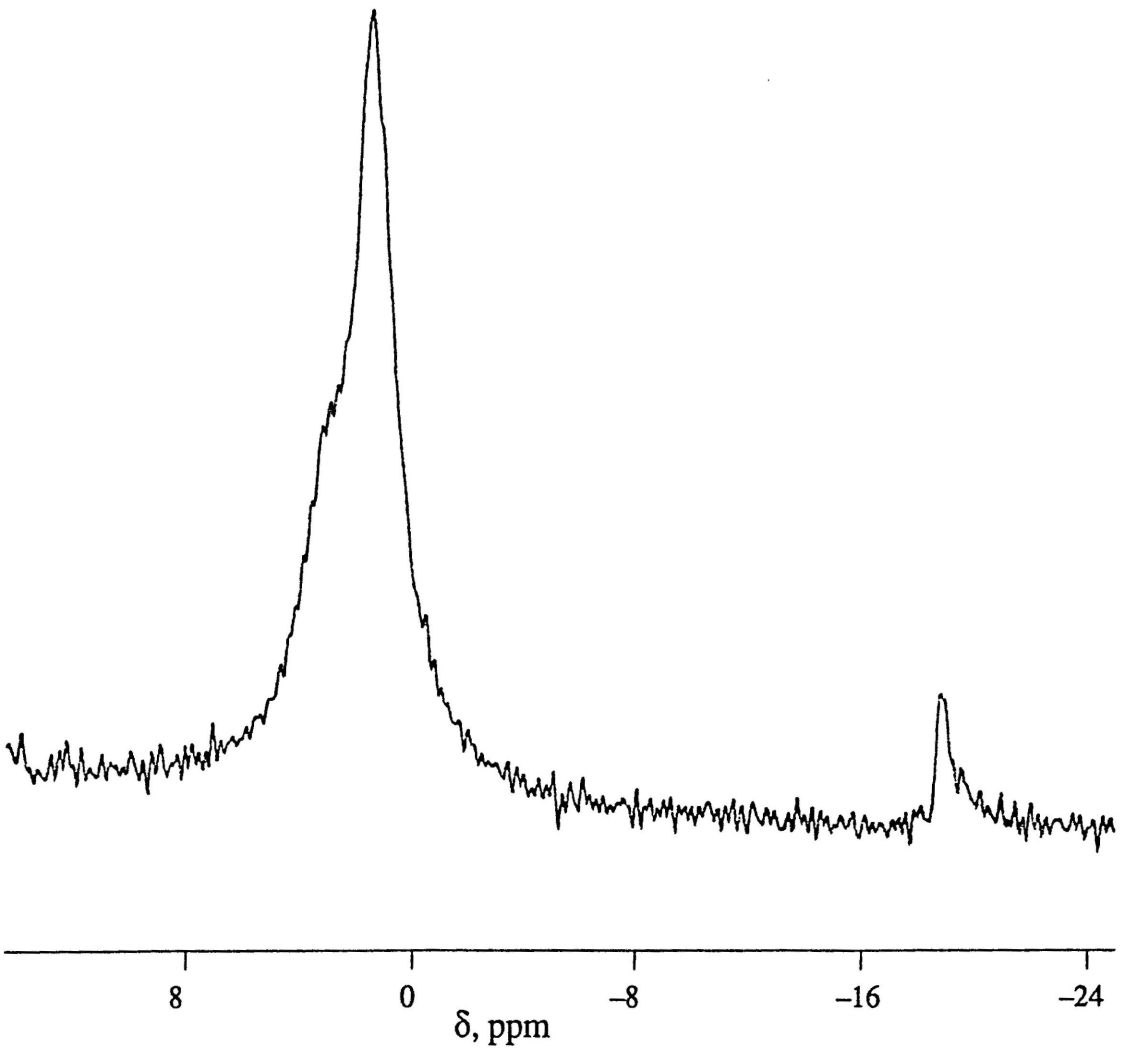
8
0
–8
–16
–24
δ, ppm

Table 3.1. Crystal, Experimental, and Refinement Data for $[Ph_4P][^2HCr_2(CO)_{10}]$.

mol formula	$Cr_2PC_{34}H_{21}O_{10}$
FW	724.5
a, Å	14.2384 (9)
b, Å	16.6178 (12)
c, Å	15.9909 (8)
β, deg	115.511 (5)
V, Å^3	3414.7 (9)
Z	4
D_{calcd}, g cm^{-3}	1.409
λ, Å	0.71073
cryst syst	monoclinic
space group	$P2_1/c$
μ, cm^{-1}	7.2
cryst dimens, mm	0.10 × 0.12 × 0.50
color	yellow
min rel transmissn, %	93.84
temp., °C	26
scan type	ω–2θ
θ limits, deg	1–25
no. of reflcns	5988
no. of obsd reflcns	4268
observn criterion	$I>1\sigma(I)$
no. of parameters refined	428
$R\left(=\sum \lvert\Delta F\rvert / \sum F_o\right)$	0.055
$R_w\left(=\left(\sum w(\Delta F)^2 / \sum wF^2\right)^{1/2}\right)$	0.043
max resid density, e Å^{-3}	0.33
min resid density, e Å^{-3}	–0.34

Table 3.2. Coordinates and Equivalent Isotropic Thermal Parameters for $[Ph_4P][^2HCr_2(CO)_{10}]$.

Atom	x	y	z	Beq[a],
Cr1	0.20618 (4)	0.56338 (4)	0.57651 (4)	4.14 (1)
Cr2	0.42548 (4)	0.46794 (4)	0.67861 (4)	3.90 (1)
C11	0.0905 (3)	0.6223 (3)	0.5051 (3)	5.6 (1)
O11	0.0187 (2)	0.6603 (2)	0.4597 (2)	8.1 (1)
C12	0.1579 (3)	0.4726 (2)	0.4994 (3)	5.2 (1)
O12	0.1287 (2)	0.4179 (2)	0.4526 (2)	8.19 (9)
C13	0.1440 (3)	0.5234 (3)	0.6524 (3)	6.1 (1)
O13	0.1088 (2)	0.5004 (3)	0.6984 (2)	10.6 (1)
C14	0.2652 (3)	0.6486 (3)	0.6607 (3)	5.9 (1)
O14	0.3008 (3)	0.6994 (2)	0.7121 (2)	9.3 (1)
C15	0.2714 (3)	0.6007 (2)	0.5029 (3)	4.7 (1)
O15	0.3061 (2)	0.6247 (2)	0.4558 (2)	6.69 (8)
C21	0.5509 (3)	0.4157 (2)	0.7196 (3)	5.3 (1)
O21	0.6300 (2)	0.3837 (2)	0.7443 (2)	8.4 (1)
C22	0.4808 (3)	0.5701 (2)	0.6760 (2)	4.23 (9)
O22	0.5130 (2)	0.6331 (2)	0.6755 (2)	6.09 (8)
C23	0.4503 (3)	0.4869 (3)	0.8024 (3)	5.4 (1)
O23	0.4683 (3)	0.4976 (2)	0.8780 (2)	9.0 (1)
C24	0.3499 (3)	0.3746 (3)	0.6770 (3)	5.9 (1)
O24	0.3016 (3)	0.3193 (2)	0.6752 (2)	9.3 (1)
C25	0.4062 (3)	0.4490 (2)	0.5554 (2)	4.7 (1)
O25	0.3988 (2)	0.4363 (2)	0.4833 (2)	7.38 (9)
P	0.18883 (6)	0.40053 (6)	–0.00915 (6)	3.29 (2)
C31	0.2968 (2)	0.3435 (2)	–0.0067 (2)	3.36 (8)
C32	0.3772 (3)	0.3217 (2)	0.0768 (2)	4.6 (1)
C33	0.4610 (3)	0.2788 (2)	0.0771 (3)	5.6 (1)

Table 3.2. Continued

C34	0.4629 (3)	0.2570 (3)	–0.0042 (3)	6.2 (1)
C35	0.3836 (3)	0.2781 (3)	–0.0872 (3)	6.3 (1)
C36	0.2995 (3)	0.3214 (2)	–0.0892 (3)	5.0 (1)
C41	0.2082 (3)	0.5054 (2)	–0.0217 (2)	3.72 (9)
C42	0.2816 (3)	0.5299 (3)	–0.0506 (3)	5.9 (1)
C43	0.2966 (4)	0.6112 (3)	–0.0586 (3)	8.7 (2)
C44	0.2414 (4)	0.6667 (3)	–0.0348 (4)	8.6 (2)
C45	0.1707 (4)	0.6423 (3)	–0.0052 (4)	7.7 (2)
C46	0.1526 (3)	0.5623 (3)	0.0009 (3)	6.1 (1)
C51	0.0724 (2)	0.3651 (2)	–0.1036 (2)	3.36 (8)
C52	0.0007 (3)	0.4180 (2)	–0.1643 (3)	4.9 (1)
C53	–0.0911 (3)	0.3879 (3)	–0.2328 (3)	6.9 (1)
C54	–0.1108 (3)	0.3072 (3)	–0.2405 (3)	6.4 (1)
C55	–0.0391 (3)	0.2549 (3)	–0.1817 (3)	5.4 (1)
C56	0.0530 (3)	0.2827 (2)	–0.1132 (2)	4.13 (9)
C61	0.1789 (2)	0.3878 (2)	0.0983 (2)	3.45 (8)
C62	0.1157 (3)	0.3296 (3)	0.1079 (2)	5.1 (1)
C63	0.1145 (3)	0.3180 (3)	0.1932 (3)	7.2 (1)
C64	0.1737 (3)	0.3653 (3)	0.2666 (3)	6.5 (1)
C65	0.2372 (3)	0.4227 (3)	0.2580 (3)	6.2 (1)
C66	0.2392 (3)	0.4348 (3)	0.1735 (3)	5.3 (1)
H	0.305 (3)	0.507 (2)	0.658 (2)	8 (1)[b]

[a]The equivalent isotropic thermal parameter is defined by the equation

[b]The bridging hydrogen atom was refined isotropically.

Table 3.3. Selected Bond Distances (Å) and Angles (°) for $[Ph_4P][^2HCr_2(CO)_{10}]$.

Cr1–Cr2	3.2465 (8)	Cr1–H–Cr2	140 (3)
Cr1–H	1.72 (3)	C13–Cr1–Cr2–C23	–44.3 (2)
Cr2–H	1.74 (4)		
ave Cr–C_{ax}	1.833 (3)		
ave Cr–C_{eq}	1.887 [8]		

Table 3.4. Deuterium Quadrupole Coupling Constants and Asymmetry Parameters, ^1H Chemical Shifts, and Crystallographic Structural Data.

Fig 2 label	comp temp, K	metal–carbonyl [a] geometry	$\lvert e^2q_{zz}Q/h \rvert$, kHz	η	χ_ν^2 [b]	chemical [c] shift, ppm	d(M–H), Å	∠(M–H–M), deg	method [d]	ref
Cr–1	$[Et_4N][^2HCr_2(CO)_{10}]$	eclipsed				–18.8	1.707 (21), 1.737 (19)	158.9 (6)	N	11
	300		85.4 (1)	0.034 (1)	2.6				(^1H, 295 K)	
	200		89.5 (2)	0.032 (3)	1.2					
	140		90.4 (2)	0.027 (3)	1.8					
Cr–2	$[(Ph_3P)_2N][^2HCr_2(CO)_{10}]$	eclipsed				–18.5	1.718 (9) – 1.750(8)	153.9 (10),	N	14
	300		84.6 (3)	0.039 (4)	1.4			157.6 (7)	(^2H, 17 K)	
Cr–3	$[Ph_4P][^2HCr_2(CO)_{10}]$	bent staggered				NA	1.72 (3), 1.74 (4)	140 (3)	X	this work
	300		66.7 (4)	0.162 (6)	1.7				(^2H, 299 K)	
	200		68.2 (5)	0.200 (8)	1.0					
	140		63.2 (5)	0.23 (1)	1.7					
W–1	$[Et_4N][^2HW_2(CO)_{10}]$	eclipsed				–12.1	1.718 (12), 2.070 (12)	137.1 (10)	N	34
	300		83.0 (4)	0.040 (4)	0.9				(^1H, 14 K)	

Table 3.4. Continued

	$[(Ph_3P)_2N][^2HW_2(CO)_{10}]$	bent staggered			−11.6	nd[f]	nd[f]	X	15
	300	62.6 (3)	0.201 (3)	2.1				(^{1}H, rt[e])	
W–3	$[Ph_4P][^2HW_2(CO)_{10}]$	bent staggered			−11.1	1.897 (5)	123.4 (5)	N	4
	300	54.1 (8)	0.31 (2)	0.6				(^{1}H, 40 K)	

[a] See Figure 3.1. [b] Data variance obtained from the baseline, typically ~5 %. [c] Obtained from ^{1}H CRAMPS results. Solution ^{1}H NMR chemical shifts (d_6-acetone) are: $[HCr_2(CO)_{10}]^-$ salts, –19.5 ppm; $[HW_2(CO)_{10}]^-$ salts, –12.5 ppm. The chemical shift for the $[Et_4N]$ salts are in reference 41 for THF solution. [d] N = Neutron diffraction and X = X-ray diffraction. The isotope in the bridging hydride and the temperature are also listed. [e] Room temperature = rt. [f] Not determined = nd.

References for Chapter 3

(1) (a) Louisiana State University, (b) Eastern Illinois University.

(2) Handy, L. B.; Ruff, J. K.; Dahl, L. F. *J. Am. Chem. Soc.* **1970**, *92*, 7312-26.

(3) Bau, R.; Teller, R. G.; Kirtley, S. W.; Koetzle, T. F. *Acc. Chem. Res.* **1979**, *12*, 176-83.

(4) Hart, D. W.; Bau, R.; Koetzle, T. F. *Organometallics* **1985**, *4*, 1590-4.

(5) Harris, D. C.; Gray, H. B. *J. Am. Chem. Soc.* **1975**, *97*, 3073-5.

(6) Eyermann, C. J.; Chung-Phillips, A. *Inorg. Chem.* **1984**, *23*, 2025-9.

(7) Blinc, R.; Rutar, V.; Seliger, J.; Slak, J.; Smolej, V. *Chem. Phys. Lett.* **1977**, *48*, 576-8.

(8) Atwood, J. L.; Hrncir, D. C.; Rogers, R. D.; Howard, J. A. K. *J. Am. Chem. Soc.* **1981**, *103*, 6787-8.

(9) Howell, J. M.; Sapse, A. M.; Singman, E.; Synder, G. *J. Am. Chem. Soc.* **1982**, *104*, 4758-9.

(10) Chiles, R. A.; Dykstra, C. E. *Chem. Phys. Lett.* **1982**, *92*, 471-3.

(11) Roziere, J.; Williams, J. M.; Stewart, R. P., Jr.; Petersen, J. L.; Dahl, L. F. *J. Am. Chem. Soc.* **1977**, *99*, 4497-9.

(12) Petersen, J. L.; Johnson, P. L.; O'Connor, J.; Dahl, L. F.; Williams, J. M. *Inorg. Chem.* **1978**, *17*, 3460-9.

(13) Bau, R.; Koetzle, T. F. *Pure & Appl. Chem.* **1978**, *50*, 55-63.

(14) Petersen, J. L.; Brown, R. K.; Williams, J. M.; McMullan, R. K. *Inorg. Chem.* **1979**, *18*, 3493-8.

(15) Wilson, R. D.; Graham, S. A.; Bau, R. *J. Organometal. Chem.* **1975**, *91*, C49-52.

(16) Ertl, G. In *The Nature of the Surface Chemical Bond*; Rhodin, T. M.; Ertl, G., Ed.; North-Holland: Amsterdam, 1979, Chapter. 5.

(17) Panas, I.; Siegbahn, P. E. M. *J. Chem. Phys.* **1990**, *92*, 4625-7.

(18) Wei, I. Y.; Fung, B. M. *J. Chem. Phys.* **1971**, *55*, 1486-7.

(19) Jarrett, W. L.; Farlee, R. D.; Butler, L. G. *Inorg. Chem.* **1987**, *25*, 1381-3.

(20) Ireland, P. S.; Olson, L. W.; Brown, T. L. *J. Am. Chem. Soc.* **1975**, *97*, 3548-9.

(21) Altbach, M. I.; Hiyama, Y.; Gerson, D. J.; Butler, L. G. *J. Am. Chem. Soc.* **1987**, *109*, 5529-31.

(22) Altbach, M. I.; Hiyama, Y.; Wittebort, R. J.; Butler, L. G. *Inorg. Chem.* **1990**, *29*, 741-7.

(23) Dixon, M.; Overill, R. E.; Platt, E. *J. Mol. Struct.* **1978**, *48*, 115-122.

(24) Soda, G.; Chiba, T. *J. Chem. Phys.* **1969**, *50*, 439-55.

(25) Butler, L. G.; Brown, T. L. *J. Am. Chem. Soc.* **1981**, *103*, 6541-6549.

(26) Brown, T. L.; Butler, L. G.; Curtin, D. Y.; Hiyama, Y. ;. P., I. C.; Wilson, R. G. *J. Am. Chem. Soc.* **1982**, *104*, 1172-1177.

(27) d'Avignon, D. A.; Brown, T. L. *J. Phys. Chem.* **1981**, *85*, 4073-9.

(28) Keiter, E. A.; Hiyama, Y.; Brown, T. L. *J. Mol. Struct.* **1983**, *111*, 1-10.

(29) Hiyama, Y.; Keiter, E. A.; Brown, T. L. *J. Magn. Reson.* **1986**, *67*, 202-10.

(30) Huber, H. *J. Chem. Phys.* **1985**, *83*, 4591-8.

(31) Snyder, L. C.; Basch, H. *Molecular Wave Functions and Properties*; John Wiley & Sons: New York, 1972.

(32) Snyder, L. C. *J. Chem. Phys.* **1978**, *68*, 291-4.

(33) Barfield, M.; Gottlieb, H. P. W.; Doddrell, D. M. *J. Chem. Phys.* **1978**, *69*, 4504-15.

(34) Witschel, J., Jr.; Fung, B. M. *J. Chem. Phys.* **1972**, *56*, 5417-22.

(35) Gerstein, B. C.; Dybowski, C. R. *Transient Techniques in NMR of Solids*; Academic Press: New York, 1985.

(36) Poole, C. P.; Farach, H. A. *Theory of Magnetic Resonance*; Wiley-Interscience: New York, 1987.

(37) Reid, R. V., Jr.; Vaida, M. L. *Phys. Rev. Lett.* **1975**, *34*, 1064.

(38) Zare, R. N. *Angular Momentum*; Wiley-Interscience: New York, 1988.

(39) Goldstein, H. *Classical Mechanics*, 2nd ed.; Addison-Wesley: New York, 1980, Note error in eq B-3y.

(40) A more efficient weighting scheme has been reported. Alderman, D. W.; Solum, M. S.; Grant, D. M. *J. Chem. Phys.* **1986**, *84*, 3717-25.

(41) Waugh, J. S.; Gonen, O.; Kuhns, P. *J. Chem. Phys.* **1987**, *86*, 3816-8.

(42) $e^2q_{zz}Q/h = +85.4$ kHz, $r = 1.7\text{x}10^{-8}$ cm, $\theta = 158.9°$.

(43) Guo, K.; Jarrett, W. L.; Butler, L. G. *Inorg. Chem.* **1987**, *26*, 3001-4.

(44) Hayter, R. G. *J. Am. Chem. Soc.* **1966**, *88*, 4376-82.

(45) Frenz, B. A. *Enraf Nonius Structure Determination Package SDP/VAX V3.0*; Enraf-Nonius: Delft, Holland, copyright 1985.

(46) Butler, L. G. *J. Magn. Reson.* **1991**, *91*, 369-9, and references therein.

(47) Fukushima, E.; Roeder, S. B. W. *Experimental Pulse NMR: A Nuts and Bolts Approach*; Addison-Wesley: Reading, MA, 1981, Chapter 5.

(48) Michaels, D. C.; Kim, A. J.; Perilloux, B. C.; Barksdale, D.; Butler, L. G. *Computers & Chemistry* **1991**, submitted for publication.

(49) LabVIEW for Macintosh computers, National Instruments, 6504 Bridge Point Parkway, Austin, TX 78730-5039.

(50) Matlab for VAX/VMS and Macintosh computers. The MathWorks Inc., 24 Prime Park Way, Natick, MA 01760.

(51) Bevington, P. R. *Data Reduction and Error Analysis for the Physical Sciences*; McGraw-Hill: New York, 1969.

(52) Press, W. H.; Flannery, B. P.; Teukolsky, S. A.; Vetterling, W. T. *Numerical Recipes*; Cambridge University Press: Cambridge, 1986.

(53) Bronnimann, C. E.; Hawkins, B. L.; Zhang, M.; Maciel, G. E. *Anal. Chem.* **1988**, *60*, 1743-50.

(54) Burum, D. P.; Rhim, W. K. *J. Chem. Phys.* **1979**, *70*, 3553-4.

(55) The 17 K neutron crystallographic structural determination is made difficult because of extensive cation disorder and some disorder in the anion.

(56) The symmetry of the jump motion discussed herein differs from that of previous ^2H NMR studies. The four site jump motion occurs between equivalent sites of a compound with D_{4h} local symmetry. The possible two-site jump motion refers to a system with local D_{2h} symmetry, in contrast to two-site jumps of phenyl rings where the effective symmetry at the deuteron is C_{2v}.

(57) Cooper, C. B.; Shriver, D. F.; Onaka, S. In *Transition Metal Hydrides*; Bau, R., Ed.; American Chemical Society: Washington, DC, 1978, p 232-47.

(58) Kara, A.; DePristo, A. E. *J. Chem. Phys.* **1990**, *92*, 5653-60.

CHAPTER 4

Solid-State ^{13}C and ^{31}P NMR Chemical Shielding Tensors in Square-Planar Metal Complexes and Metal Dimers

4.1. Introduction

Solid-state NMR spectroscopy of S = 1/2 nuclei, principally ^{13}C and ^{31}P, has been utilized to yield information concerning electronic and structural aspects of organometallic complexes. ^{31}P NMR spectroscopy has been more frequently used than ^{13}C in the organometallic studies, because of the 100 % natural abundance and the relatively high sensitivity of the ^{31}P nucleus. ^{13}C chemical shielding tensors have been measured in metal carbonyls[23-27] to investigate the metal-carbonyl bonding. ^{31}P chemical shielding tensors have been successfully correlated with the M–P–M bond angle in $M_2(CO)_6(\mu\text{–}X)(\mu\text{–}PPh_2)$ (M = Fe, Ru, Os and X = three-electron-donor hydrocarbyl ligand)[28]. The oxidation state of phosphorus and the formal charge on the phosphate group[29] also have a pronounced effect on the ^{31}P chemical shielding tensor. In addition, the solid-state structures of $(R_3P)_2MX_2$ (M = Pd, Pt and X = Cl, Br, I, CN, N_3)[30,31] and the *cis* and *trans* isomers of $(R_3P)_2MCl_2$ (M = Pd, Pt)[32] have been studied by ^{13}C and ^{31}P CP/MAS NMR spectroscopy.

Herein, we report the ^{13}C chemical shielding tensors for $K_2Ni(CN)_4\cdot H_2O$, $K_2Pd(CN)_4\cdot 3H_2O$, and $K_2Pt(CN)_4\cdot 3H_2O$ and the ^{31}P chemical shielding tensors for $K_4[Pt_2(P_2O_5H_2)_4]\cdot 2H_2O$ and $K_4[Pt_2(P_2O_5H)_4X_2]\cdot 2H_2O$ (X = Cl, Br). The ^{13}C chemical shielding tensors were obtained from the ^{13}C NMR powder patterns. The ^{31}P chemical shielding tensors were determined from the ^{31}P MAS spectra. The diamagnetic and paramagnetic contributions to the chemical shielding tensors for the metal cyanide complexes have been estimated using the Flygare–Goodisman approximation. The paramagnetic contribution shows a good correlation with the metal-cyanide π back–bonding. However, the applicability of the Flygare–Goodisman approximation to transition metal complexes is questioned. We speculate that a modification may be necessary, possibly one that treats core and valence metal electrons separately.

4.2. Spectroscopy of the $M(CN)_4^{2-}$ (M=Ni, Pd, and Pt) System

The major components of the time-independent Hamiltonian for the M–CN system include the ^{13}C Zeeman and chemical shielding interactions, ^{14}N Zeeman and quadrupolar interactions, and ^{13}C–^{14}N dipolar coupling. If the metal has an isotope of appreciable abundance with S>0 and a relatively large gyromagnetic ratio, then M–^{13}C dipolar and, possibly, J coupling must be included.

In the case of $[Pt(CN)_4]^{2-}$, the total Hamiltonian for the interactions experienced by the ^{13}C nucleus is

$$H_{total} = H_{CS}^{C} + H_{Z}^{N} + H_{Q}^{N} + H_{D}^{CN} + H_{Z}^{Pt} + H_{D}^{PtC} + H_{J}^{PtC} \tag{4.1}$$

where the ^{13}C Zeeman and chemical shielding interaction with the static magnetic field along the laboratory z-axis, B_z^o, is expressed by

$$H_{CS}^{C} = -\hbar\gamma^{C}B_{z}^{o}\left(1 + \delta_{Lab}^{zz}\right)\mathbf{I}_{z}^{C} \tag{4.2}$$

The ^{13}C resonance of the CN group is affected by not only the quadrupole-perturbed Zeeman states of ^{14}N but also by the ^{13}C–^{14}N dipolar interaction in the Hamiltonian,

$$\begin{aligned} H_{Z}^{N} + H_{Q}^{N} + H_{D}^{CN} = & -\hbar\gamma^{N}B_{z}^{o}\left(1 + \delta_{iso}^{N}\right)\mathbf{S}_{z}^{N} + \\ & \frac{eQ/\hbar}{6I(2I-1)}\sum_{k,j} eq_{kj}^{Lab}\left[\frac{3}{2}\left(\mathbf{S}_{k}^{N}\mathbf{S}_{j}^{N} + \mathbf{S}_{j}^{N}\mathbf{S}_{k}^{N}\right) - \delta_{kj}\mathbf{S}^{N2}\right] + \\ & \left\{\frac{\gamma^{C}\gamma^{N}\hbar}{\left|\mathbf{r}_{Lab}^{CN}\right|^{3}}\left[\mathbf{I}_{x}^{C}\mathbf{S}_{x}^{N} + \mathbf{I}_{y}^{C}\mathbf{S}_{y}^{N} + \mathbf{I}_{z}^{C}\mathbf{S}_{z}^{N}\right] - \right. \\ & \left. 3\frac{\gamma^{C}\gamma^{N}\hbar}{\left|\mathbf{r}_{Lab}^{CN}\right|^{5}}\left\{\left[\mathbf{I}_{x}^{C}r_{x} + \mathbf{I}_{y}^{C}r_{y} + \mathbf{I}_{z}^{C}r_{z}\right] + \left[\mathbf{S}_{x}^{N}r_{x} + \mathbf{S}_{y}^{N}r_{y} + \mathbf{S}_{z}^{N}r_{z}\right]\right\}\right\} \end{aligned} \tag{4.3}$$

where the ^{15}N isotropic chemical shift, δ_{iso}^{N}, is 105.5 (2) ppm relative to $NaNO_3$[33]. The ^{15}N chemical shift anisotropy[34] of the cyanide ion in $(CH_3)_3(C_6H_4)C{\equiv}N$[35] is

384 ppm, which has a negligible effect on the ^{13}C NMR powder pattern. The ^{14}N quadrupole coupling constant, $e^2q_{zz}Q/h$, for $K_2[Pt(CN)_4]\cdot 3H_2O$ is 3.467 MHz and the asymmetry parameter, η, is 0.032[36]; the same values were used in the analysis of Ni and Pd complexes. The ^{14}N quadrupole interaction perturbs the ^{13}C NMR powder pattern only when the ^{14}N quadrupole interaction is comparable in size to the ^{14}N Zeeman interaction; the ^{14}N Larmor frequency is 14.448 MHz at 4.7 Tesla. Given the relatively small effect of the quadrupolar interaction, the partial assignment of the ^{13}C chemical shielding tensor orientation is based largely on the ^{13}C–^{14}N dipolar coupling. The C–N bond distance of 1.159 Å from the X–ray crystallographic studies for $K_2[Pt(CN)_4]\cdot 3H_2O$[37,38] was used in the calculation of the ^{13}C powder patterns. The C–N bond distances are 1.13 Å for $K_2[Ni(CN)_4]$[37] and 1.16 Å for $Na_2[Pd(CN)_4]\cdot 3H_2O$[39]. In the calculations for the Ni and Pd complexes, quadrupole interactions from the S = 3/2 ^{61}Ni isotopomer (1.19 %) and S = 5/2 ^{105}Pd isotopomer (22.23 %) are ignored.

The ^{195}Pt–^{13}C dipolar and ^{195}Pt Zeeman interactions are similar to those given in eq 4.3. The ^{195}Pt isotropic chemical shift for $K_2[Pt(CN)_4]\cdot 3H_2O$ is 4713 ppm relative to H_2PtCl_6[40]. Even though the ^{195}Pt chemical shift anisotropy can be quite large for square-planar complexes, 9100 ppm in $Ba[Pt(CN)_4]\cdot 2H_2O$[41] and 10340 ppm in K_2PtCl_4,[42] ^{195}Pt chemical shift anisotropy does not significantly affect the ^{13}C NMR powder pattern. The Pt–C bond distance is 1.989 (2) Å[38]. The ^{195}Pt–^{13}C isotropic J coupling is given by

$$H_J^{PtC} = J\,(\mathbf{I}_x^C\mathbf{S}_x^{Pt} + \mathbf{I}_y^C\mathbf{S}_y^{Pt} + \mathbf{I}_z^C\mathbf{S}_z^{Pt}) \qquad (4.4)$$

The isotropic J coupling constant between ^{13}C and ^{195}Pt nucleus, 1300 Hz, is measured from the ^{13}C MAS spectrum. No corrections are made for J anisotropy; if the J anisotropy is similar to that found for the ^{199}Hg–^{31}P system[43], then the effect on the ^{13}C powder pattern is negligible.

After each Hamiltonian term has been expanded for the uncoupled product basis set of $|^{14}N\ ^{195}Pt\ ^{13}C>$ by direct product expansion from Pauli spin matrices, the resulting 12x12 matrices are added to obtain the total Hamiltonian matrix. The eigenenergies are obtained by diagonalization. The six single-quantum ^{13}C transitions are used to generate the ^{13}C powder pattern over the two Euler angles, θ and χ, where the angles are incremented by a uniform step angle of 2° within the range of 0 to 90° and with sin θ weighting. Figure 4.1 shows a calculated ^{13}C powder pattern for $[Pt(CN)_4]^{2-}$, in which both ^{13}C–^{14}N and ^{195}Pt–^{13}C interactions are considered and the orientation of the largest principal element of the ^{14}N electric field gradient tensor, eq_{zz}, coincides with the C–N bond direction.

4.3. Experimental Methods

4.3.1. Sample Preparation. $K_2Ni(CN)_4 \cdot H_2O$ was made by the literature method[44] from $NiSO_4 \cdot 6H_2O$ (Aldrich) and KCN (99 % ^{13}C enrichment, Isotec). $K_2Pd(CN)_4 \cdot 3H_2O$ and $K_2Pt(CN)_4 \cdot 3H_2O$ were made by analogous procedures from $PdSO_4$ (Aldrich) and $K_2Pt(NO_2)_4$ (Aldrich). $K_4[Pt_2(P_2O_5H)_4] \cdot 2H_2O$ ("Pt_2"), $K_4[Pt_2(P_2O_5H)_4Cl_2] \cdot 2H_2O$ ("Pt_2Cl_2"), and $K_4[Pt_2(P_2O_5H)_4Br_2] \cdot 2H_2O$ ("Pt_2Br_2") were made by literature method.[45,46]

4.3.2. Solid-State ^{13}C and ^{31}P NMR Spectroscopy. Solid-state ^{13}C and ^{31}P powder patterns were taken on stationary samples with a Bruker MSL 200 solid-state NMR spectrometer operating at 50.301 and 80.98 MHz for ^{13}C and ^{31}P, respectively, using a high power probe with a solenoidal coil. The 90° pulse length was 2 μs for both ^{13}C and ^{31}P and the spectra were acquired as simple Bloch decays. The ^{13}C chemical shift values recorded on the δ scale are referenced through benzene (128.7 ppm) to TMS and the ^{31}P values to 85 % H_3PO_4 as external standards.

Exponentially filtered (200 Hz), Fourier-transformed, and manually phased spectra were transferred as binary files from the Bruker Aspect-3000 computer to a Macintosh II computer via an RS-232 serial connection and the KERMIT file transfer program. Conversion from binary to ASCII data files was done with a program[47] written in LabVIEW, a graphical programming language.[48] Spectral simulation programs were written in Matlab, a vector oriented programming language.[49] The Levenberg–Marquardt nonlinear least-squares algorithm[50,51] was recoded in Matlab.

The ^{31}P MAS spectra were acquired on Bruker MSL 200 and 500 solid-state NMR spectrometers using a 15 kHz CP/MAS probe and a 4 mm ZrO_2 rotor with a Kel-F cap. Powdered samples, 70 to 100 mg, were loosely packed into the rotor along with alumina as an inert filler. At 80.98 MHz resonance frequency (MSL 200), the 90° pulse was 5 μs and the spectra were acquired as simple Bloch decays. At 202.46 MHz (MSL 500), an 8.9 μs (< 90° tip angle) pulse was used. Note: This work was the first usage of this 500 MHz CP/MAS probe for ^{31}P where it was discovered that the probe could not be tuned well to the resonance frequency. A Herzfeld–Berger graphical method[52] was used to obtain the ^{31}P principal tensor elements from the spinning sidebands of the MAS spectra.

The isotropic ^{13}C chemical shifts were acquired for the metal cyanide complexes with ^{13}C MAS NMR and referenced through adamantane (external) to TMS. The ^{13}C MAS line shape of each sideband is affected by dipolar coupling to ^{14}N, but the isotropic chemical shift remains basically unchanged[53,54].

4.4. Results

The ^{13}C experimental powder patterns for $K_2Ni(CN)_4 \cdot H_2O$, $K_2Pd(CN)_4 \cdot 3H_2O$, and $K_2Pt(CN)_4 \cdot 3H_2O$ are shown in Figure 4.2. Also shown are the nonlinear least-squares fits of a simulated spectrum to the experimental spectrum,

obtained by varying δ_{11} and δ_{33}; the value of δ_{22} is determined from δ_{11} and δ_{33} and the isotropic chemical shift. Based on the ^{13}C–^{14}N dipolar coupling, δ_{33} is required to be aligned with the CN bond axis. In a single crystal NMR study of $K_2Pt(CN)_4Br_{0.3}\cdot 3H_2O$[55], the orientation of the ^{13}C chemical shielding tensor relative to the molecular axis was assigned. Based on the similar values for δ_{11} and δ_{22} found, here, the same orientation is likely with δ_{22} perpendicular to the plane of the square-planar metal complex, and δ_{11} perpendicular to the CN bond axis and in the plane of the metal complex. The assignment of the orientations of δ_{11} and δ_{22} is tentative; single crystal NMR studies could be used to confirm the assignment. Table 4.1 shows the solid-state ^{13}C chemical shielding tensor elements and their orientations relative to the molecular framework.

It is difficult to reliably extract the principal elements of the chemical shielding tensor from the ^{31}P powder pattern. In principle, an analysis of the ^{31}P powder patterns can be made as was done for ^{13}C in $K_2Pt(CN)_4\cdot 3H_2O$. However, because the chemical shift range for the phosphorus site is relatively small with respect to both the ^{31}P–^{195}Pt dipolar and J coupling interactions, the ^{31}P powder pattern is relatively featureless at 4.7 Tesla. Thus, the uncertainty in the fit of a simulated ^{31}P powder pattern to the experimental powder pattern is unacceptably large. For this reason, the principal elements of the ^{31}P chemical shielding tensor were acquired from a Herzfeld–Berger analysis of the ^{31}P MAS spectra and are listed in Table 4.2. In the MAS experiment, it is possible to focus on the spinning sidebands of the S = 0 Pt isotopomer; thus the ^{195}Pt spectral component is excluded from the analysis. Shown in Figure 4.3 is the featureless ^{31}P powder pattern of $K_4[Pt_2(P_2O_5H_2)_4]\cdot 2H_2O$ and well-resolved ^{31}P MAS spectra at three different spin rates. Figure 4.4 compares the ^{31}P MAS spectra for $K_4[Pt_2(P_2O_5H_2)_4]\cdot 2H_2O$, $K_4[Pt_2(P_2O_5H_2)_4Cl_2]\cdot 2H_2O$, and $K_4[Pt_2(P_2O_5H_2)_4Br_2]\cdot 2H_2O$. The spectra are similar to solution-state ^{31}P NMR spectra, though the line width, ~430 Hz (FWHH), obscures all but the single bond

J coupling between ^{31}P and ^{195}Pt. The 33% abundant ^{195}Pt leads to a doublet in the ^{31}P spectrum which is superimposed upon the ^{31}P singlet; the J coupling constants are given in Table 4.2. The doublet for the ^{31}P–^{195}Pt spin system in $K_4[Pt_2(P_2O_5H_2)_4Cl_2]\cdot 2H_2O$ is noticeably asymmetric in the MAS spectrum. An asymmetry of this type in a ^{31}P powder pattern has been shown to be a result of an anisotropic J (^{31}P–^{199}Hg) coupling tensor.[56] The orientation of the ^{31}P chemical shielding tensor is not obtained from a Herzfeld–Berger analysis of the S = 0 Pt isotopomers. Single crystal NMR studies were attempted for $K_4[Pt_2(P_2O_5H_2)_4]\cdot 2H_2O$, but were unsuccessful due to a lack of a large crystal.

The changes in the ^{13}C and ^{31}P chemical shielding tensors show the following trends. For metal cyanide complexes, the isotropic ^{13}C chemical shift is essentially the same in solution as in the solid state. There is a small upfield shift (more negative values on the δ scale) in δ_{11} and δ_{22} going from Ni to Pt, and that effect has been noted earlier for δ_{iso}[57]. The value of δ_{33} is nearly constant. For the binuclear platinum diphosphite complexes, the isotropic chemical shifts and J coupling constants are essentially the same in solution as in the solid state. There is an upfield shift going from Pt(II) to Pt(III); δ_{11} and δ_{33} shift upfield while δ_{22} is nearly constant.

4.5. Discussion

The NMR chemical shielding of a nucleus, in the Ramsey approach[58], can be decomposed into two contributions, diamagnetic and paramagnetic, which are opposite in sign. In *ab initio* SCF calculations, the decomposition leads to a diamagnetic contribution that can vary greatly, but can be quite accurately estimated by the Flygare–Goodisman approximation. On the other hand, when either Pople–Slater's or Pople–Burn's approximations are applied to calculate the diamagnetic contribution, the changes are negligible.[59] The Flygare–Goodisman approximation have been applied

to the estimation of the diamagnetic contribution and successfully utilized for chemical shift analysis in several organic molecules containing 1st and 2nd row atoms.[60,61]

We pose two questions: (1) In the metal cyanide complexes, the ^{13}C chemical shielding tensor elements are quite similar, with only a minor variation in δ_{11} and δ_{22}. Why is there so little change in the chemical shift on going from Ni to Pt? (2) Is the Flygare–Goodisman approximation for the diamagnetic contribution valid for transition metal complexes? If we estimate the diamagnetic contribution using the Flygare–Goodisman approximation and paramagnetic contribution, the corresponding paramagnetic contribution has a very large dependence on the metal, yet it seems quite fortuitous that the variation acts so as to cancel most of the variation from the diamagnetic contribution over the range of metals Ni to Pt.

The decomposition of the chemical shielding tensor into diamagnetic and paramagnetic contributions is given by[58]

$$\delta_{\alpha\alpha} = \delta^{dia}_{\alpha\alpha} + \delta^{para}_{\alpha\alpha} \quad (\alpha = x,y,z). \tag{4.5}$$

In a series of molecular orbital calculations on small molecules, Flygare and Goodisman noted that the calculated diamagnetic contribution can be approximated by (using the δ scale and in SI units)[62]

$$\delta^{dia}_{xx} = \delta^{dia}(\text{free atom}) - \frac{\mu_o e^2}{8\pi m} \sum \frac{Z}{r^3}(r_y^2 + r_z^2) \tag{4.6}$$

(and analogous eqs for δ^{dia}_{yy} and δ^{dia}_{zz}) where μ_o is the permittivity of free space, e is the charge of the electron, m is the mass of electron, and Z is the atomic number. The scalar δ^{dia}(free atom) is relatively easily calculated[63,64]. While the validity of the Flygare–Goodisman approximation for transition metal complexes has been briefly questioned[65], we are not aware of any detailed investigation of the matter. However,

the approximation describes quite well the $\sigma_{\parallel}$ elements for both ^{13}C and ^{33}S in carbon disulfide as obtained from SCF calculations over a variety of basis sets.[66]

For the purpose of better illustrating this rather arcane area of NMR spectroscopy, we now discuss the particular case of acetonitrile. Shown in Figure 4.5 are selected ^{13}C chemical shielding tensor elements for $CH_3{}^{13}CN$ on both the σ and δ chemical shift scales; the scales are related by

$$\delta = \frac{(\sigma_{ref} - \sigma)}{(1 - \sigma_{ref})} \tag{4.7}$$

where σ_{ref} is the shielding of the appropriate reference compound relative to the bare C nucleus.[34,67] Since $CH_3{}^{13}CN$ has axial symmetry, the parallel and perpendicular components, $\delta_{\parallel}^{dia}$ and $\delta_{\perp}^{dia}$, define the diamagnetic component of the chemical shielding tensor. Shown in Figure 4.5 is $\delta_{\perp}^{dia}$(calc) = –221.8 ppm from an INDO SCF–MO calculation[68]. Also shown in Figure 4.5 (insert) is the Flygare–Goodisman approximation for $\delta_{\perp}^{dia}$ for $CH_3{}^{13}CN$ based on contributions from the neighboring nitrogen and methyl carbon atoms, but ignoring the methyl hydrogens. The relatively close agreement with the INDO SCF–MO results is typical for the Flygare–Goodisman approximation for small molecules. The ^{13}C chemical shielding tensor component parallel to the C–N bond, $\delta_{\parallel}$(exp) = –96 ppm, is dominated by diamagnetic shielding; sites with axial symmetry have small values for $\delta_{\parallel}^{para}$[69,70]. The Flygare–Goodisman approximation yields $\delta_{\parallel}^{dia}$ = –75.34 ppm, in rather good agreement with the experimental result. We conclude that the accuracy for estimating the diamagnetic contribution in small molecules is on the order of 20 ppm. As a starting point, we will assume that the Flygare–Goodisman approximation can be applied to transition metal systems.

To illustrate the diamagnetic and paramagnetic contributions in a metal cyanide complex, we show in Figure 4.6 a simple metal-carbon fragment. The ^{13}C chemical

shielding tensor is decomposed into diamagnetic and paramagnetic shielding tensors. From this figure, and again using the Flygare–Goodisman approximation, we note that the metal contributes to an upfield shift (more negative values on the δ scale) in the elements of the diamagnetic tensor perpendicular to the metal-carbon bond.

The paramagnetic contribution depends in large part on carbon p orbitals (the effect of metal d orbitals is diminished by the $1/r^3$ operator centered on carbon). The angular momentum operators couple to give either 0 or ±1 according to the following relationships,

$$\langle p_m | L_k | p_j \rangle = \varepsilon_{mjk}, \quad \varepsilon_{mjk} = \begin{cases} 0, & \text{if m, j, k repeat} \\ +1, \text{ or} & \text{if m, j, k are in cyclic order: (x,y,z), (y,z,x), or (z,x,y)} \\ -1, & \text{if m, j, k are in anticyclic order: (x,z,y), (z,y,x), or (y,x,z)} \end{cases} \tag{4.8}$$

where ε_{mjk} is the Levi–Civita symbol.[59] So, the occupied σ-donating orbital (p_z) couples with one of the empty π-accepting orbitals (p_x) to create a paramagnetic contribution along the y-axis. Similarly, the other empty π-accepting orbital (p_y) couples with the σ-donating (p_z) orbital to create a contribution along the x-axis. Here, we use the common, simplifying assumption that state wavefunctions can be represented by contributions from simple atomic orbitals. Because of the cylindrical symmetry of the metal-carbon fragment, the paramagnetic term along the z-axis is zero.[70]

To summarize, metal cyanide complexes can be expected to exhibit the following patterns in the ^{13}C chemical shielding tensor:

(1) $\delta_{\parallel}^{dia}$ and $\delta_{\parallel}^{para}$ will not depend on the metal; thus $\delta_{\parallel}$ should have a value near –75 ppm (that of a free carbon atom).

(2) If the Flygare–Goodisman approximation is valid for transition metal

complexes, then $\delta_{\perp}^{dia}$ will shift upfield as the atomic number of the metal increases.

(3) Changes in the metal-carbon bonding, either σ-donating or π-accepting, will be reflected in $\delta_{\perp}^{para}$. There are many factors involved in the paramagnetic contribution, but roughly, the stronger the metal-carbon bond, the larger, and more positive, will be $\delta_{\perp}^{para}$.

We now turn to the experimental results for Ni, Pd, and Pt cyanide complexes. In the following discussion of the ^{13}C NMR data, we make a simplifying assumption. We will treat the metal cyanides as axially symmetric triatomic systems. Thus, we define $\delta_{\perp} = (\delta_{11} + \delta_{22})/2$ and $\delta_{\parallel} = \delta_{33}$. First, we discuss the value of $\delta_{\parallel}$ for the metal cyanide complexes. Since the analysis shown in Figure 4.6 indicates that the metal does not contribute to either $\delta_{\parallel}^{dia}$ or $\delta_{\parallel}^{para}$, the estimated value for $\delta_{\parallel}^{dia}$ = δ(free atom) = –75 ppm. The measured values range from –92.7 (3) to –94.9 (4) ppm in reasonable agreement with the prediction. The most important observation is the lack of a dependence upon the metal atom.

We now turn to the value of $\delta_{\perp}$ for the metal cyanide complexes. We make the assumption that the Flygare–Goodisman approximation can be applied to transition metals. From eq 4.6, we calculate the value of $\delta_{\perp}^{dia}$ for the metal cyanides based on the experimental M–C bond lengths and the calculated value of $\delta_{\perp}^{dia}$ for $CH_3{}^{13}CN$[68] to obtain the following values: Ni, $\delta_{\perp}^{dia}$ = –364.8 ppm; Pd, $\delta_{\perp}^{dia}$ = –478.8 ppm; and, Pt, $\delta_{\perp}^{dia}$ = –706.3 ppm. The difference between $\delta_{\perp}$(exp) and $\delta_{\perp}^{dia}$ yields $\delta_{\perp}^{para}$. The estimated values of $\delta_{\perp}^{para}$ range from 620 for Ni to 945 ppm for Pt complex.

The value of $\delta_{\perp}^{para}$ should show a rational dependence upon structural features that reflect changes in the metal-carbon bonding. Two structural features of note are: (1) F_{MC}, the metal-carbon bond stretching force constant determined from a force field

analysis of the metal cyanide complexes in aqueous solution[71], and (2) Δ_1, a ligand-field parameter derived from d–d transitions in the electronic absorption spectrum. Δ_1 is the difference between the $b_{1g}(x^2-y^2)$ and $b_{2g}(xy)$ orbital energies in a square-planar metal complex and is a measure of both σ and π bonding interactions between the metal and the ligand[72,73]. This ligand field parameter is used here as an approximation for the energy separation between ground and excited electronic states; it is not required here that the magnitude of the energy separation is correct but only that the change in the energy separation going from Ni to Pt is well represented. Shown in Figure 4.7 are plots of both $1/F_{MC}$ and $1/\Delta_1$ versus the estimated $\delta_{\perp}^{para}$ for Ni, Pd, and Pt cyanide complexes. The reciprocals of F_{MC} and Δ_1 are plotted since δ^{para} shows an inverse energy dependence with the $1/(E_{ex} - E_{grd})$ term (see Figure 4.6). One interpretation of Figure 4.7 is based on the concept that π back–bonding is stronger for Pt than for Ni, as can be inferred from the reduction in the C–N stretching force constant on going from Ni to Pt[71]. Then, π back–bonding lowers the energy of excited states that have contributions from carbon p_x and p_y orbitals, and the larger $1/(E_{ex} - E_{grd})$ terms for the Pt complex create a larger value for $\delta_{\perp}^{para}$.

There may be a problem with this decomposition of the chemical shielding tensor. We do not know if the Flygare–Goodisman approximation for δ^{dia} is appropriate for metal core electrons. In their original work, only light atoms were discussed. It is plausible that only valence electrons of neighboring atoms should contribute to the diamagnetic shielding. The estimated value of $\delta_{\perp}^{dia}$ varies from –221.8 ppm for $CH_3{}^{13}CN$ to –167.8 ppm for HCN[68] and to –706.3 ppm for Pt–CN. Yet, the observed $\delta_{\perp}$ varies by only 33 ppm (HCN to Ni–CN). It seems fortuitous that the paramagnetic contribution should track so precisely in magnitude, but having the opposite sign, so as to cancel nearly completely the changes in the diamagnetic contribution. The isotropic chemical shifts of transition metal hydrides also suggest

that the diamagnetic contribution is over-estimated by using the Flygare–Goodisman approximation in a simple fashion. The isotropic chemical shifts for transition metal hydrides should be dominated by the diamagnetic contribution since the paramagnetic terms will be small due to a lack of low-lying p orbitals centered on hydrogen. If the Flygare–Goodisman approximation is valid for metals, then third row metal hydrides should be upfield of first row metal hydrides; similarly bridging metal hydrides should be upfield of terminal metal hydrides. Neither effect is consistently observed[74], suggesting that the diamagnetic contribution from the metal is over-estimated by a simple application of the Flygare–Goodisman approximation to transition metal complexes.

We now turn to the ^{31}P chemical shift tensors in binuclear platinum diphosphite complexes. Because the coordination at phosphorus is not changed in the series $K_4[Pt_2(P_2O_5H_2)_4]\cdot 2H_2O$, $K_4[Pt_2(P_2O_5H_2)_4Cl_2]\cdot 2H_2O$, and $K_4[Pt_2(P_2O_5H_2)_4Br_2]\cdot 2H_2O$, the diamagnetic contribution to the chemical shielding tensor elements should remain nearly constant. The range of chemical shift for ^{31}P is quite large. In analogy with Figure 4.5, the chemical shifts (δ scale) for the bare ^{31}P nucleus and free ^{31}P atom are 356 and –605 ppm, respectively, relative to 85 % H_3PO_4.[63,75] The fact that the value of δ_{33} is not close to that for a free ^{31}P atom for any of the compounds listed in Table 4.2 suggests a large paramagnetic contribution. In fact, highly shielded tensor elements are relatively rare in ^{31}P NMR, with P_4 (δ_{11} = –190, δ_{22} = –597, and δ_{33} = –597 ppm)[34,76] and related systems such as P_4S_3[34,77] being some of the few examples.

The ^{31}P chemical shift tensor orientations have not been determined experimentally in this study, though the element δ_{33} is believed to be parallel to the Pt–^{31}P bond axis. The partial tensor orientation is shown in Table 4.2, as is the tensor orientation for a related ^{31}P site, the phosphite anion. In the solution-state NMR study by Farrar and Locker of HPO_3^{2-}, the value of the chemical shift tensor elements were

determined by T_1 studies of the P–H spin system. Also, a single crystal ^{31}P NMR study of chlorotris(triphenylphosphine)rhodium(I) showed that the most shielded element is almost parallel to the Rh–P bond.[78]

As the platinum metal center is oxidized from the II to III formal oxidation state, two of the three chemical shielding tensor elements and the $^{1}J(P–Pt)$ coupling constant change. We speculate that one of the more significant changes occurring at the platinum metal center is a change in coordinate number from four to six, with the higher symmetry of the six-coordinate site affecting the paramagnetic contribution. An increase in the value of $^{1}J(P–Pt)$ may be due to the shorter P–Pt bond, with increased *s*-orbital character in the P–Pt bonds.

4.6. Conclusions

The principal elements and the relative orientations of the ^{13}C chemical shielding tensor have been obtained for Ni, Pd, and Pt cyanide complexes in the solid state. The results can be correlated with an increase in π back–bonding in the order Ni < Pd < Pt. The principal elements of the ^{31}P chemical shielding tensor have been obtained for three binuclear platinum diphosphite complexes. Two of the three tensor elements change, becoming more shielded, as the coordination number at platinum increases.

The individual contributions from diamagnetic and paramagnetic interactions have been discussed for the ^{13}C chemical shielding tensors. While Flygare–Goodisman's approximation has been useful for calculating diamagnetic contribution in molecules containing light atoms, our results suggest that the validity of the approximation for transition metal complexes should be reexamined. We note here that in their original paper, Flygare and Goodisman explained the approximation only in terms of light atoms; the application to transition metal systems was not discussed, and

perhaps not intended or implied by the authors. Nevertheless, the notion that the magnitude of the diamagnetic contribution, even for transition metal complexes, depends upon Z and is, unfortunately, well established. We now suspect that the diamagnetic contribution from atoms, at least for transitions metals, near an NMR-active nucleus is a more complicated function of the core and valence electron distribution. We would be delighted if a modified Flygare–Goodisman approximation were to be developed by one of the many clever theoreticians in NMR spectroscopy.

Acknowledgments. The support of the National Science Foundation (CHE–8715517) is gratefully acknowledged. The purchase of the Bruker MSL 200 NMR spectrometer and the high–speed CP/MAS probe was made possible by NSF grant CHE–8711788 and the Louisiana Education Quality Support Fund, respectively. Leslie G. Butler is a Fellow of the Alfred P. Sloan Foundation (1989-91). Dr.Carol Fitzpatrick and the Exxon Research and Engineering Company at Baton Rouge are gratefully acknowledged for the use of the Bruker MSL 500 NMR spectrometer.

Figure 4.1.

Calculated ^{13}C powder pattern for $K_2Pt(CN)_4 \cdot 3H_2O$. Important parameters in this calculation are: $\delta_{11} = 251.8$, $\delta_{22} = 226.2$, $\delta_{33} = -94.2$ ppm, d(C–N) = 1.159, d(Pt–C) = 1.989 Å, $e^2q_{zz}Q/h$ (^{14}N) = 3.467 MHz, and $\eta = 0.032$. (a) The ^{13}C powder pattern is composed of two components; the relative intensities from two isotopomers, ^{196}Pt–$^{13}C^{14}N$ and ^{195}Pt–$^{13}C^{14}N$, are 66.2 : 33.8. (Here, we use ^{196}Pt to represent all the S = 0 isotopomers of Pt.) (b) The spectrum calculated for the ^{196}Pt–$^{13}C^{14}N$ isotopomer. The ^{13}C–^{14}N dipolar coupling splits the ^{13}C resonance into three sub-spectra. (c) The spectrum calculated for the ^{195}Pt–$^{13}C^{14}N$ isotopomer. The ^{195}Pt–^{13}C dipolar coupling splits the ^{13}C resonance into two sub-spectra.

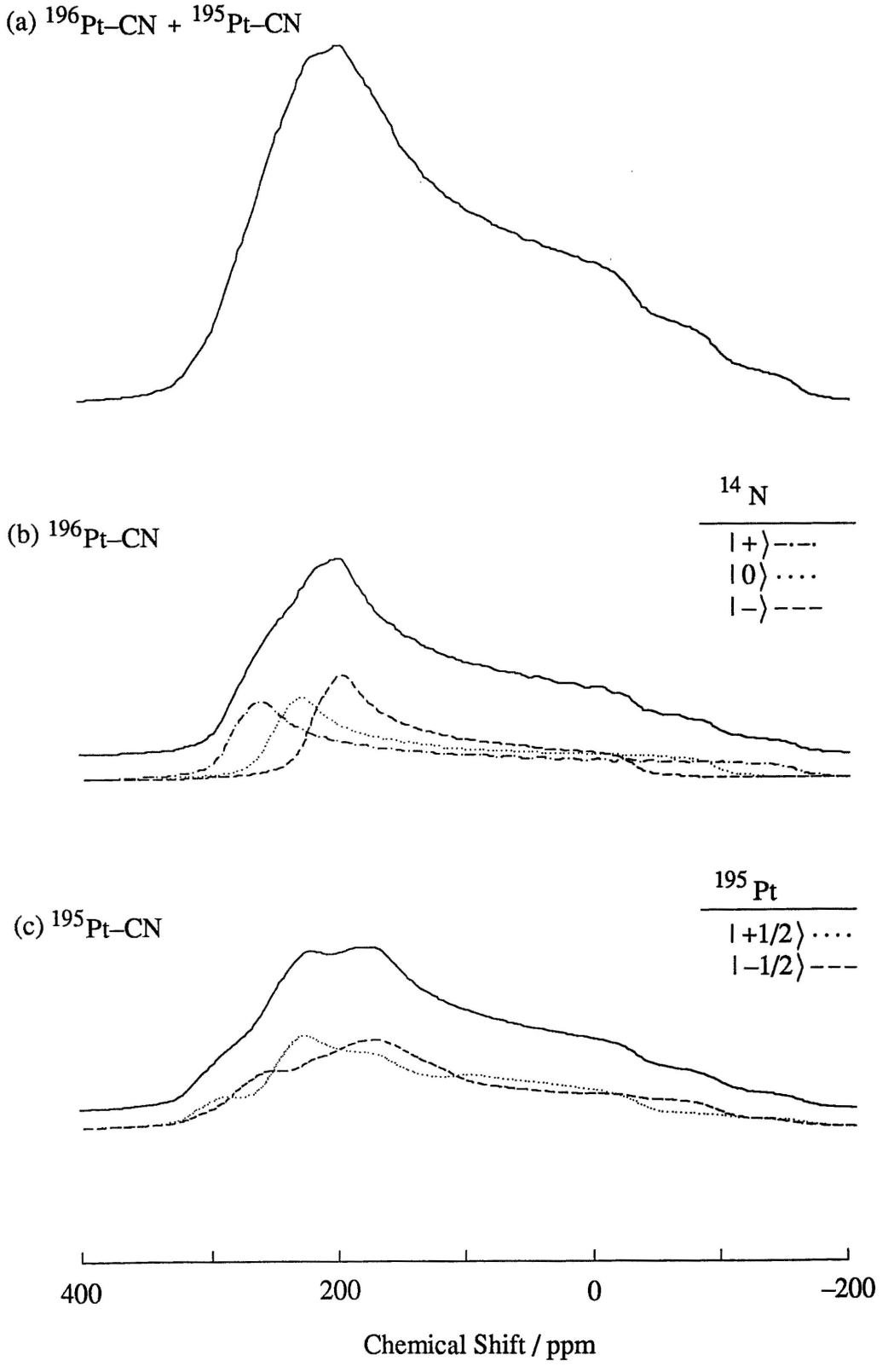
(a) 196Pt–CN + 195Pt–CN
(b) 196Pt–CN
14 N
|+⟩
|0⟩
|−⟩
(c) 195Pt–CN
195 Pt
|+1/2⟩
|−1/2⟩
400
200
0
−200
Chemical Shift / ppm

Figure 4.2.

Solid-state ^{13}C chemical shift powder patterns and the corresponding nonlinear least-squares fits. Circles (o), solid lines (–), and crosses (+) represent the experimental ^{13}C chemical shift powder pattern, the best calculated fit, and the residual between the experimental spectrum and the fit, respectively. Experimental parameters are as follows (NS = number of scans, RD = recycle time):

(a) $K_2Ni(CN)_4 \cdot H_2O$, NS = 528, RD = 120 s, $\chi^2_\nu = 1.8$;

(b) $K_2Pd(CN)_4 \cdot 3H_2O$, 604, 120 s, 2.0; and,

(c) $K_2Pt(CN)_4 \cdot 3H_2O$, 520, 120 s, 1.3.

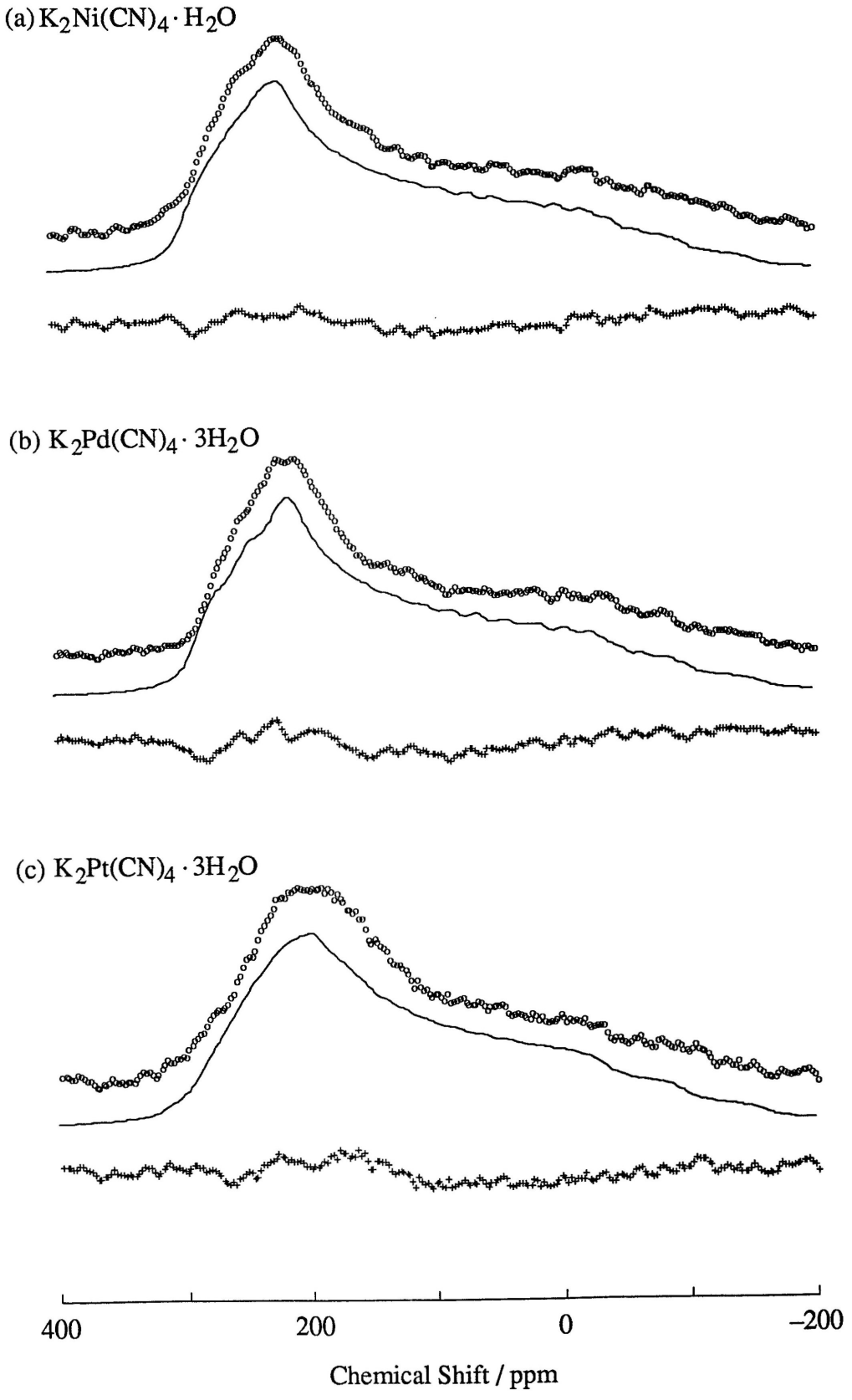
(a) $K_2Ni(CN)_4 \cdot H_2O$
(b) $K_2Pd(CN)_4 \cdot 3H_2O$
(c) $K_2Pt(CN)_4 \cdot 3H_2O$
400
200
0
–200
Chemical Shift / ppm

Figure 4.3.

Solid-state ^{31}P powder pattern of $K_4[Pt_2(P_2O_5H_2)_4]\cdot 2H_2O$ and ^{31}P MAS spectra at different spin rates, ν_r. Asterisks (*) and crosses (+) represent the spinning sidebands and the J coupling peaks to ^{195}Pt, respectively. Experimental parameters are as follows:

(a) ν_L = 80.98 MHz, ν_r = 0 kHz, NS = 30, RD = 120 s;

(b) 202.46 MHz, 6 kHz, 16, 100 s;

(c) 202.46 MHz, 8 kHz, 8, 100 s; and,

(d) 202.46 MHz, 11 kHz, 8, 100 s.

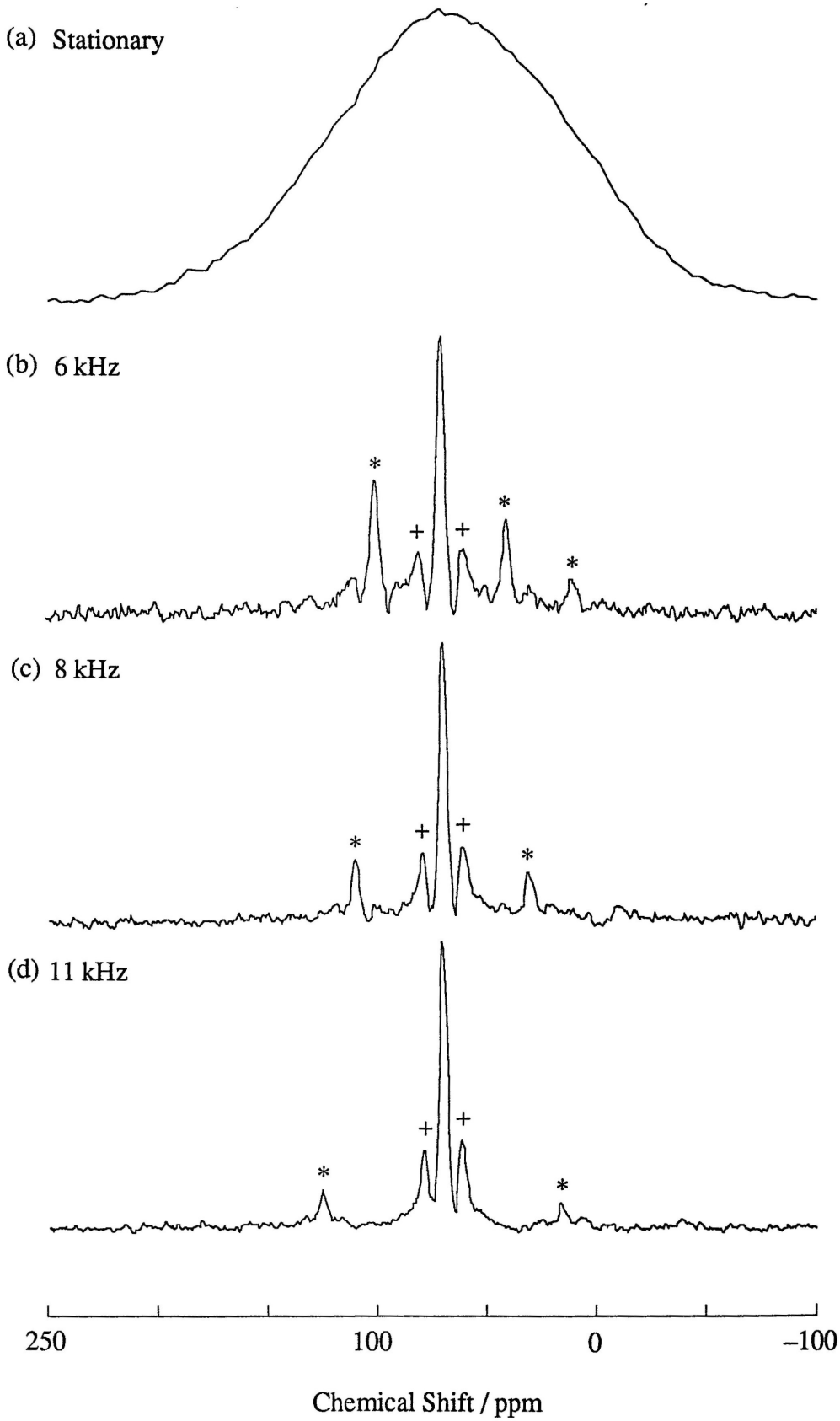
(a) Stationary
(b) 6 kHz
(c) 8 kHz
(d) 11 kHz
250
100
0
–100
Chemical Shift / ppm

Figure 4.4.

Solid-state ^{31}P MAS spectra of $K_4[Pt_2(P_2O_5H_2)_4]\cdot 2H_2O$, $K_4[Pt_2(P_2O_5H_2)_4Cl_2]\cdot 2H_2O$, and $K_4[Pt_2(P_2O_5H_2)_4Br_2]\cdot 2H_2O$ at $\nu_r = 10$ kHz and $\nu_L = 80.98$ MHz. The spectra show a single peak at the ^{31}P isotropic chemical shift and a doublet due to J coupling to ^{195}Pt. Experimental parameters are as follows:

(a) $K_4[Pt_2(P_2O_5H_2)_4]\cdot 2H_2O$, NS=100, RD=30 s;

(b) $K_4[Pt_2(P_2O_5H_2)_4Cl_2]\cdot 2H_2O$, 250, 30 s; and,

(c) $K_4[Pt_2(P_2O_5H_2)_4Br_2]\cdot 2H_2O$, 88, 30 s.

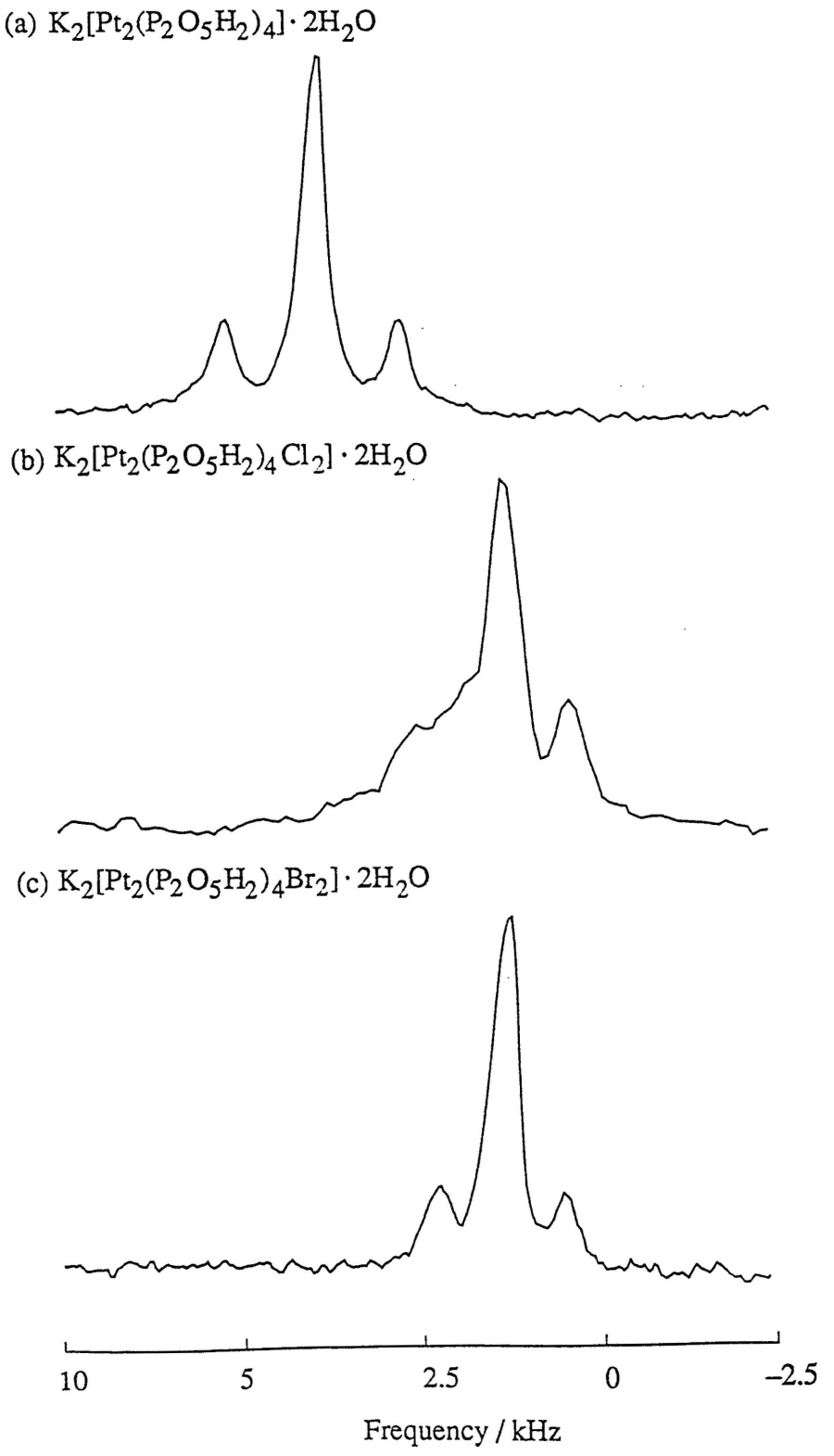
(a) $K_2[Pt_2(P_2O_5H_2)_4]\cdot 2H_2O$
(b) $K_2[Pt_2(P_2O_5H_2)_4Cl_2]\cdot 2H_2O$
(c) $K_2[Pt_2(P_2O_5H_2)_4Br_2]\cdot 2H_2O$
10
5
2.5
0
–2.5
Frequency / kHz

Figure 4.5.

Diagram showing both σ and δ scales for ^{13}C chemical shielding and shifts, respectively. Shown on the chemical shift scale are the experimental value of $\delta_{\parallel}$ and the calculated value (INDO SCF–MO) for $\delta_{\perp}^{dia}$ for $CH_3{}^{13}CN$. Shown in the inserts are the estimated values for $\delta_{\parallel}^{dia}$ and $\delta_{\perp}^{dia}$ using the Flygare–Goodisman approximation. In the estimation of $\delta_{\parallel}^{dia}$, the effect of the methyl hydrogens is ignored. Not shown in the figure is the experimental value for the perpendicular chemical shift: $\delta_{\perp}$ (exp) = 224 ppm[79].

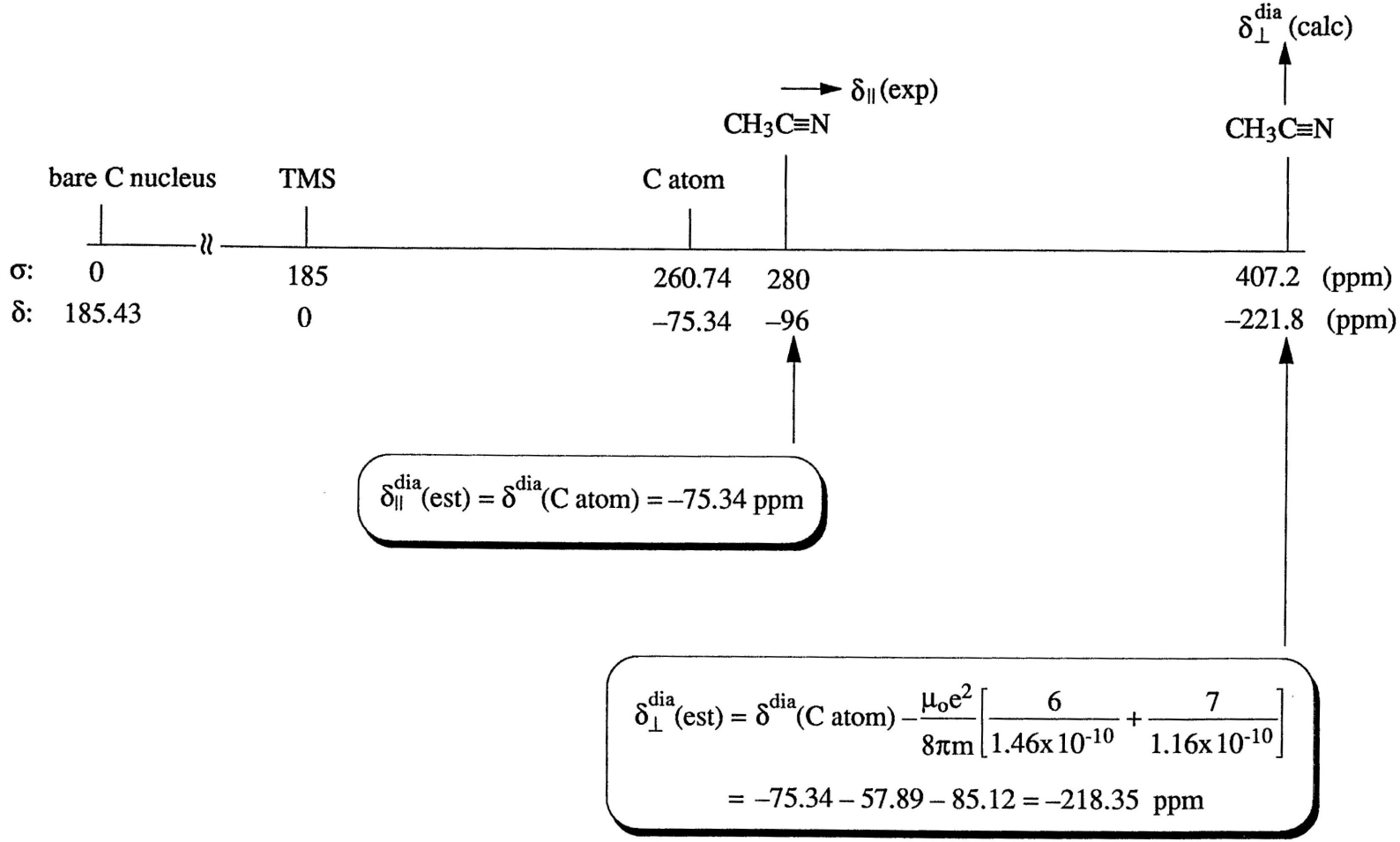
$\delta_{\perp}^{dia}$(calc)
$\delta_{\parallel}$(exp)
$CH_3C{\equiv}N$
$CH_3C{\equiv}N$
bare C nucleus
TMS
C atom
σ: 0 185 260.74 280 407.2 (ppm)
δ: 185.43 0 –75.34 –96 –221.8 (ppm)
$\delta_{\parallel}^{dia}(est) = \delta^{dia}(C\ atom) = -75.34$ ppm
$\delta_{\perp}^{dia}(est) = \delta^{dia}(C\ atom) - \frac{\mu_o e^2}{8\pi m}\left[\frac{6}{1.46\times10^{-10}} + \frac{7}{1.16\times10^{-10}}\right]$
$= -75.34 - 57.89 - 85.12 = -218.35$ ppm

Figure 4.6.

The illustration of the diamagnetic and paramagnetic contributions to the ^{13}C chemical shielding tensor in a simple metal-carbon fragment with axial symmetry.

Chemical Shift
(relative to bare C nucleus)

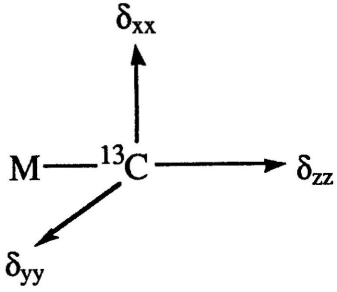

=

Diamagnetic Contribution

$$\delta_{xx}^{dia} = \delta^{dia}(\text{C atom}) - \frac{\mu_o e^2}{8\pi m}\frac{Z}{d}$$

$\overrightarrow{r_M} = (0,0,-d)$

M—13C → $\delta_{zz}^{dia} = \delta^{dia}(\text{C atom})$

$$\delta_{yy}^{dia} = \delta^{dia}(\text{C atom}) - \frac{\mu_o e^2}{8\pi m}\frac{Z}{r_M^3}\left(r_{M_x}^2 + r_{M_z}^2\right) = \delta^{dia}(\text{C atom}) - \frac{\mu_o e^2}{8\pi m}\frac{Z}{d}$$

+

Paramagnetic Contribution

$$\delta_{xx}^{para} = \frac{\mu_o e^2}{8\pi m}\left[\frac{\left\langle \phi_z^{grd}\middle|L_x\middle|\phi_y^{ex}\right\rangle\left\langle \phi_y^{ex}\middle|\frac{L_x}{r^3}\middle|\phi_z^{grd}\right\rangle}{E\left(\Psi^{ex}\approx\phi_y^{ex}\right) - E\left(\Psi^{grd}\approx\phi_z^{grd}\right)}\right]$$

π*–accepting

σ–donating

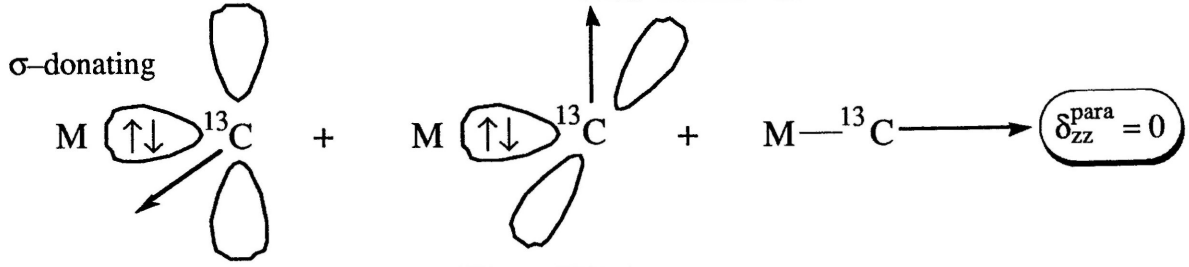

$$\delta_{yy}^{para} = \frac{\mu_o e^2}{8\pi m}\left[\frac{\left\langle \phi_x^{grd}\middle|L_y\middle|\phi_z^{ex}\right\rangle\left\langle \phi_z^{ex}\middle|\frac{L_y}{r^3}\middle|\phi_x^{grd}\right\rangle}{E\left(\Psi^{ex}\approx\phi_{z'}^{ex}\right) - E\left(\Psi^{grd}\approx\phi_x^{grd}\right)}\right]$$

Figure 4.7.

Plots of the perpendicular ^{13}C paramagnetic chemical shifts, $\delta_{\perp}^{para} = (\delta_{11}^{para} + \delta_{22}^{para})/2$, against the reciprocals of the metal-carbon bond stretching force constants ($1/F_{MC}$, ●) and the energies of the ligand field transition ($1/\Delta_1$, ◆) for $K_2Ni(CN)_4 \cdot H_2O$, $K_2Pd(CN)_4 \cdot 3H_2O$, and $K_2Pt(CN)_4 \cdot 3H_2O$. The value of $\delta_{\perp}^{para}$ is obtained using Flygare–Goodisman's approximation for $\delta_{\perp}^{dia}$.

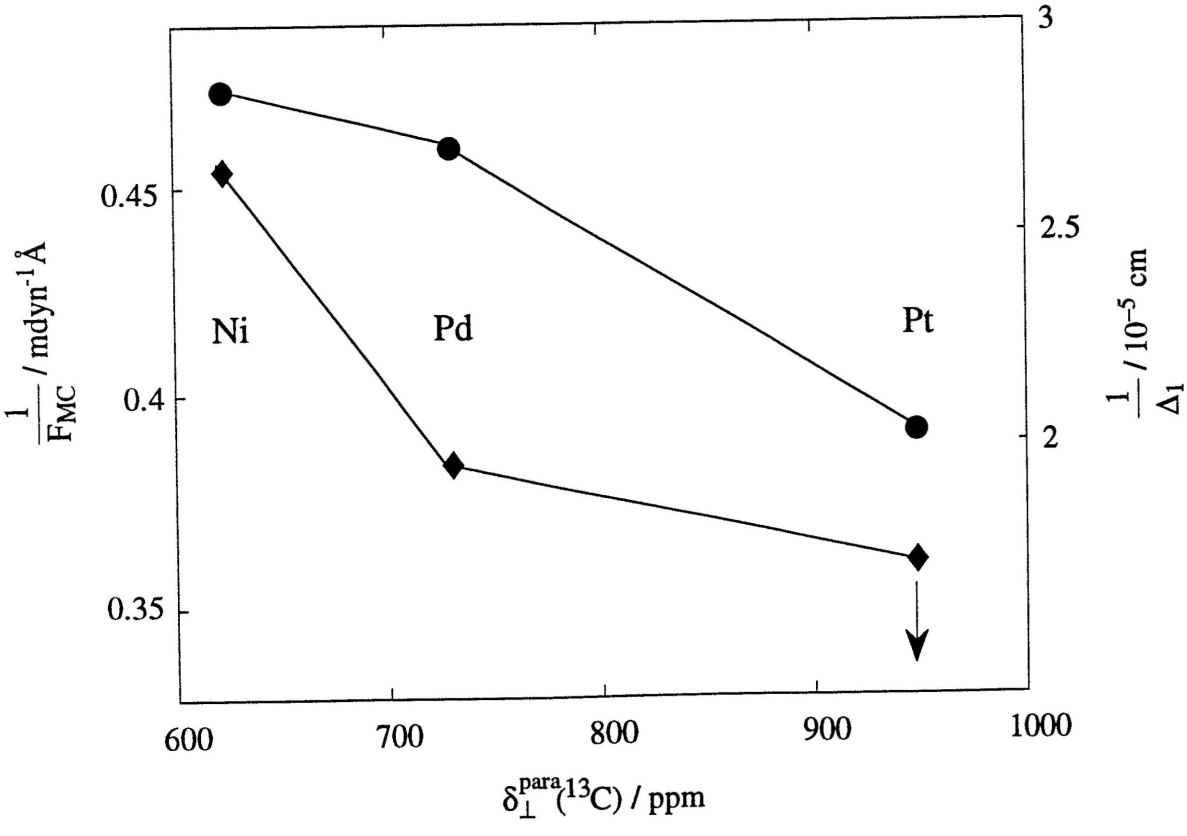
0.45
0.4
0.35
3
2.5
2
600
700
800
900
1000
Ni
Pd
Pt
$\frac{1}{F_{MC}}$ / mdyn^{-1}Å
$\frac{1}{\Delta_1}$ / 10^{-5} cm
$\delta_{\perp}^{para}(^{13}C)$ / ppm

Table 4.1. Solid–State ^{13}C NMR Chemical Shielding Tensors.

Compound	Solid State			Orientation	Solid State	Solution State[a]	F_{MC}[b]	Δ_1[c]
	δ_{11}	δ_{22}	δ_{33}		δ_{iso}	δ_{iso}	(mdyn Å^{-1})	(cm^{-1})
$K_2Ni(CN)_4 \cdot H_2O$	265.9 (3)	242.9 (3)	–92.7 (3)	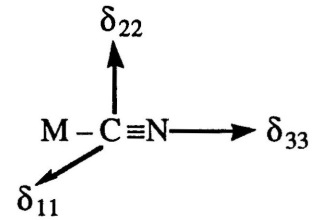	138.7	136.6	2.25 (2)	33,800
$K_2Pd(CN)_4 \cdot 3H_2O$	258.5 (3)	236.0 (3)	–94.9 (3)		133.2	131.9	2.32 (2)	44,600
$K_2Pt(CN)_4 \cdot 3H_2O$	251.8 (5)	226.2 (5)	–94.2 (4)		127.9	125.7	2.75 (1)	>50,000
$K_2Pt(CN)_4Br_{0.3} \cdot 3H_2O$[d]	225 (5)	187 (10)	–84 (10)	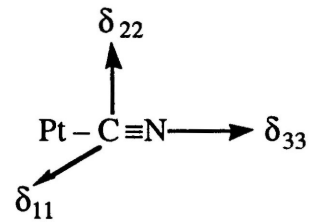	109			
HCN[e]	222	222	–112	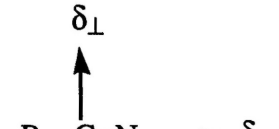	111			
CH_3CN[f]	224	224	–96		117			

[a] Ref. 57. [b] Ref. 71. [c] Ref. 72. [d] Ref. 55. [e] Dombi, G.; Diehl, P.; Lounila, J.; Wasser, R. *Org. Magn. Reson.* **1984**, *22*, 573-5. $\delta_{11} = \delta_{22} = \delta_{\perp}$ and $\delta_{33} = \delta_{\parallel}$. [f] Diehl, P.; Jokisaari, J.; Moria, F. *J. Magn. Reson.* **1982**, *49*, 498-506. Other values have been reported. The work of Diehl *et al.* is used here because they report the largest chemical shielding anisotropy on an absolute scale.

Table 4.2. Solid–State ^{31}P NMR Chemical Shielding Tensors.

Compound	Solid State [a]			Orientation	Solid State		Solution State [b]		d(Pt–P) (Å)
	δ_{11}	δ_{22}	δ_{33}		δ_{iso}	J_{Pt-P} (Hz)	δ_{iso}	J_{Pt-P} (Hz)	
$K_4[Pt_2(P_2O_5H_2)_4]\cdot 2H_2O$	138	66	6	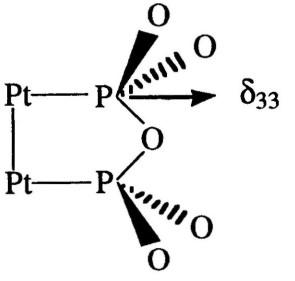	69.8	3120	69.4	3095	2.320 (5) [c]
$K_4[Pt_2(P_2O_5H_2)_4Cl_2]\cdot 2H_2O$	92	59	–69		27.5	ca.2460	28.0	2170	2.350 (2) [d]
$K_4[Pt_2(P_2O_5H_2)_4Br_2]\cdot 2H_2O$	96	60	–71		28.2	2185	24.0	2230	2.362 (2) [e]
	Solution State								
HPO_3^{2-} [f]	93	93	–30	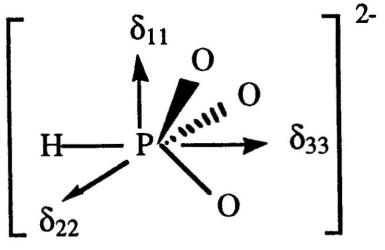					

[a] Obtained by using a Herzfeld-Berger method. Error limits are 10 – 20 ppm. [b] King, C.; Roundhill, D. M.; Dickson, M. K.; Fronczek, F. R. *J. Chem. Soc. Dalton Trans.* **1987**, 2769-80. [c] Filomena Dos Remedios Pinto, M. A.; Sadler, P. J.; Neidle, S.; Sanderson, M. R.; Subbiah, A.; Kuroda, R. J. *J. Chem. Soc., Chem. Commun.* **1980**, 13-15. Marsh, R. E.; Herbstein, F. H. *Acta Crystallogr., Sect. B* **1983**, *39*, 280-7. [d] Che, C.-M.; Schaefer, W. P.; Gray, H. B.; Dickson, M. K.; Stein, P. B.; Roundill, D. M. *J. Am. Chem. Soc.* **1982**, *104*, 4253-5. [e] Clark, R. J. H.; Kurmoo, M.; Dawes, H. M.; Hursthouse, M. B. *Inorg. Chem.* **1986**, *25*, 409-12. [f] Ref. 79. Tensor orientation shown in table based upon 3-fold site symmetry at phosphorus.

References for Chapter 4

(23) Walter, T. H.; Reven, L.; Oldfield, E. *J. Chem. Phys.* **1989**, *93*, 1320-6.

(24) Aime, S.; Botta, M.; Gobetto, R.; Osella, D.; Milone, L. *Inorg. Chim. Acta* **1988**, *146*, 151-3.

(25) Hasselbring, L.; Lamb, H.; Dybowski, C.; Gates, B.; Rheingold, A. *Inorg. Chim. Acta* **1987**, *127*, L49-51.

(26) Oldfield, E.; Keniry, M. A.; Shinoda, S.; Schramm, S.; Brown, T. L.; Gutowsky, H. S. *J. Chem. Soc., Chem. Comm.* **1985**, , 791-3.

(27) Gleeson, J. W.; Vaughan, R. W. *J. Chem. Phys.* **1983**, *78*, 5384-92.

(28) Carty, A. J.; Fyfe, C. A.; Lettinga, M.; Johnson, S.; Randall, L. H. *Inorg. Chem.* **1989**, *28*, 4120-4.

(29) Un, S.; Klein, M. P. *J. Am. Chem. Soc.* **1989**, *111*, 5119-24.

(30) Rahn, J. A.; O'Donnell, D. J.; Palmer, A. R.; Nelson, J. H. *Inorg. Chem* **1989**, *28*, 2631-5.

(31) Rahn, J. A.; Baltusis, L.; Nelson, J. H. *Inorg. Chem.* **1990**, *29*, 750-5.

(32) Nelson, J. H.; Rahn, J. A.; Bearden, W. H. *Inorg. Chem.* **1987**, *26*, 2192-3.

(33) Sano, M.; Yoshikawa, Y.; Yamatera, H. *Inorg. Chem.* **1982**, *21*, 2521-3.

(34) Duncan, T. M. *A Compilation of Chemical Shift Anisotropies*; The Farragut Press: Chicago, 1990.

(35) Sardashti, M.; Maciel, G. E. *J. Phys. Chem.* **1988**, *92*, 4620-32.

(36) Ikeda, R.; Nakamura, D.; Kubo, M. *J. Phys. Chem.* **1968**, *72*, 2982-6.

(37) Vannerberg, N.-G. *Acta Chem. Scand.* **1964**, *18*, 2385-91.

(38) Washecheck, D. M.; Peterson, S. W.; Reis, A. H.; Williams, J. M. *Inorg. Chem.* **1976**, *15*, 74-8.

(39) Colin-Moreau, M. L. *Struct. Bonding* **1972**, *10*, 167.

(40) Pesek, J. J.; Mason, W. R. *J. Magn. Reson.* **1977**, *25*, 519-29.

(41) Keller, H. J.; Rupp, H. H. *Z. Naturforsch* **1971**, *26a*, 785.

(42) Sparks, S. W.; Ellis, P. D. *J. Am. Chem. Soc.* **1986**, *108*, 3215-8.

(43) Penner, G. H.; Power, W. P.; Wasylishen, R. E. *Can. J. Chem.* **1988**, *66*, 1821-3.

(44) Fernelius, W. C.; Burbage, J. J. *Inorg. Synth.* **1946**, *2*, 227-8.

(45) Alexander, K. A.; Bryan, S. A.; Dickson, M. K.; Hedden, D.; Roundhill, D. M. *Inorg. Synth.* **1986**, *24*, 211-3.

(46) Che, C.-M.; Herbstein, F. H.; Schaefer, W. P.; Marsh, R. E.; Gray, H. B. *J. Am. Chem. Soc.* **1983**, *105*, 4604-7.

(47) Michaels, D. C.; Kim, A. J.; Perilloux, B. C.; Barksdale, D.; Butler, L. G. *Computers & Chemistry* **1991**, , in press.

(48) LabView for Macintosh computers, National Instruments, 6504 Bridge Point Highway, Austin, TX 78730-5039, (512) 794-0100.

(49) Matlab for VAX/VMS and Macintosh computers. The MathWorks Inc., 24 Prime Park Way, Natick, MA 01760.

(50) Bevington, P. R. *Data Reduction and Error Analysis for the Physical Sciences*; McGraw-Hill: New York, 1969.

(51) Press, W. H.; Flannery, B. P.; Teukolsky, S. A.; Vetterling, W. T. *Numerical Recipes*; Cambridge University Press: Cambridge, 1986.

(52) Herzfeld, J.; Berger, A. E. *J. Chem. Phys.* **1980**, *73*, 6021-30.

(53) Naito, A.; Ganapathy, S.; McDowell, C. A. *J. Magn. Reson.* **1982**, *48*, 367-81.

(54) Böhm, J.; Fenzke, D.; Pfeifer, H. *J. Magn. Reson.* **1983**, *55*, 197-204.

(55) Stoll, M. E.; Vaughan, R. W.; Saillant, R. B.; Cole, T. *J. Chem. Phys.* **1974**, *61*, 2896-9.

(56) Penner, G. H.; Wasylishen, R. E. *Can. J. Chem.* **1989**, *67*, 1909-13.

(57) Pesek, J. J.; Mason, W. R. *Inorg. Chem.* **1979**, *18*, 924-8.

(58) Ramsey, N. F. *Phys. Rev.* **1950**, *78*, 699-703.

(59) Ebraheem, K. A. K.; Webb, G. A. *Prog. NMR Spect.* **1977**, *11*, 149-81.

(60) Mason, J. *J. Chem. Soc. (A)* **1971**, 1038-47.

(61) Grinter, R.; Mason, J. *J. Chem. Soc. (A)* **1970**, , 2196-9.

(62) Flygare, W. H.; Goodisman, J. *J. Chem. Phys.* **1968**, *49*, 3122-5.

(63) Malli, G.; Froese, C. *Int. J. Quantum Chem.* **1967**, *1S*, 95.

(64) Ando, I.; Webb, G. A. *Theory of NMR Parameters*; Academic Press: New York, 1983.

(65) Brown, D. A.; Chester, J. P.; Fitzpatrick, N. J.; King, I. J. *Inorg. Chem.* **1977**, *16*, 2497-500.

(66) Wolinski, K.; Hinton, J. F.; Pulay, P. *J. Am. Chem. Soc.* **1990**, *112*, 8251-60.

(67) Becker, E. D. *High Resolution NMR; Theory and Chemical Applications*, 2nd ed.; Academic Press: New York, 1980.

(68) Barfield, M.; Grant, D. M. *J. Chem. Phys.* **1977**, *67*, 3322-9.

(69) Mahnke, H.; Sheline, R. K.; Spiess, H. W. *J. Chem. Phys.* **1974**, *61*, 55-60.

(70) Pople, J. A. *Proc. Roy. Soc. London Ser. A* **1957**, *239*, 541-9.

(71) Kubas, G. J.; Jones, L. H. *Inorg. Chem.* **1974**, *13*, 2816-9.

(72) Mason, W. R., III; Gray, H. B. *J. Am. Chem. Soc.* **1968**, *90*, 5721-9.

(73) Cowman, C. D.; Ballhausen, C. J.; Gray, H. B. *J. Am. Chem. Soc.* **1973**, *95*, 7873-5.

(74) Collman, J. P.; Hegedus, L. S.; Norton, J. R.; Finke, R. G. *Principles and Applications of Organotransition Metal Chemistry*; University Science Books: Mill Valley, CA, 1987.

(75) Jameson, C. J.; De Dios, A.; Jameson, A. K. *Chem. Phys. Lett.* **1990**, *167*, 575-82.

(76) Spiess, H. W.; Grosescu, R.; Haeberlen, U. *Chem. Phys.* **1974**, *6*, 226-34.

(77) Bjorholm, T.; Jakobsen, H. J. *J. Magn. Reson.* **1989**, *84*, 204-11.

(78) Naito, A.; Sastry, D. L.; McDowell, C. A. *Chem. Phys. Lett.* **1985**, *115*, 19-23.

(79) Farrar, T. C.; Locker, I. C. *J. Chem. Phys.* **1987**, *87*, 3281-7.

CHAPTER 5

Resolving Two Inequivalent Sites with Deuterium MAS NMR

5.1. Introduction

Techniques that can resolve slightly different deuterium sites on the basis of the values of the quadrupole coupling constant and asymmetry parameter are useful for many structural studies. In the past, techniques having high resolution included single crystal NMR[80], SEDOR[81], and field cycling techniques[82,83]. High resolution deuterium NMR/NQR spectra have been important for the study of systems having multiple hydrogen bonds[84,85], separating resonances due to terminal and bridging metal hydride sites in organometallic complexes[86], and the development of a Karplus–type relationship for ^{2}H–C–C–X units[87,88]. Recent reports on MAS NMR for quadrupole nuclei have prompted us to examine the resolution available with this potentially convenient technique.

Herein, we report deuterium MAS NMR results for four simple inorganic compounds and two physical mixtures. The question addressed can be stated as follows: Is the resolution in the deuterium MAS NMR experiment sufficient to distinguish two slightly different deuterium sites from a single site having the average quadrupolar interaction? For the physical mixture where the quadrupolar coupling constants of the two components differ by 30.4 kHz, a two component model fits the deuterium MAS NMR spectrum much better than a single component model. However, for the mixture for which the quadrupole coupling constants differ by only 4.8 kHz, either model fits the spectrum equally well. Based upon simulated MAS NMR spectra, it appears that the spin rate must be significantly slower than the difference between the quadrupole coupling constants in order to resolve two distinct sites.

5.2. Experimental Methods

5.2.1. Sample Preparation. The samples chosen have been previously studied at room temperature by Poplett and Smith[89] using $^1H/^2H$ double resonance nuclear quadrupole resonance spectroscopy. This technique yields the $|+1\rangle \rightarrow |0\rangle$ and $|0\rangle \rightarrow |-1\rangle$ transition frequencies in zero magnetic field from which the values of the deuterium quadrupole coupling constant and asymmetry parameter can be directly calculated. Also, the observed resonance frequencies are affected little by molecular reorientations in the solid state, much less than in the solid-state deuterium NMR lineshape. $^2HIO_3$ and Na^2HCO_3 yield a single pair of deuterium resonances in zero magnetic field; the experimental quadrupole coupling constants and asymmetry parameters are given in Table 5.1. In the ^2H NQR spectra, K^2HCO_3 and K^2HSO_4 each showed two different deuterium sites. For K^2HCO_3, the quadrupole coupling constant and asymmetry parameter are 154.7 (3) kHz and 0.189 (2) for site 1 and 152.6 (3) kHz and 0.193 (2) for site 2, respectively[89]. For K^2HSO_4, the quadrupole coupling constant and asymmetry parameter are 176.0 (5) kHz and 0.156 (7) for site 1 and 174.4 (2) kHz and 0.164 (2) for site 2, respectively[89].

The samples were deuterated by recrystallization from hot saturated solution of 50 % ^2H_2O + 50 % ^1H_2O and dried over silica gel. The mixtures were made by simple mixing of equal molar ratios of each component.

5.2.2. Solid-State Deuterium NMR Spectroscopy. Deuterium MAS NMR spectra were acquired at 30.709 MHz on a Bruker MSL 200 solid-state NMR spectrometer using a 7 mm CP/MAS probe at about 300 K. A spin rate of 5 kHz was used; the spin rate was stable to within 10 Hz during the acquisition of each spectrum. A 60° 2.7 μs rf pulse was used with a 200 μs delay (one rotor period) before acquisition. A relaxation delay of 60 s was used which was greater than $3xT_1$ for all samples.

The rotational echo trains were processed by application of an exponential line broadening factor of 300 Hz, Fourier transformation, baseline correction with a fourth-order polynomial, and integration of each spinning sideband. Symmetrized stick spectra were obtained by averaging each pair of spinning sidebands that are related to each other about the isotropic chemical shift. The sum of the spinning sideband integrals was normalized to a value of one by a scale factor applied to all integrals.

5.2.3. Calculation of Spinning Sideband Intensities. Simulated MAS sideband intensities were calculated using the Herzfeld–Berger method[90] with minor modifications for the quadrupolar interaction: (1) $\sigma_{iso} - \sigma_{zz} = \delta$, (2) $\gamma H_o \delta = \omega_Q = \frac{3\pi}{2}\frac{e^2 q_{zz} Q}{h}$, and (3) $\Delta_- = -\eta\frac{\omega_Q}{\omega_r}$ and $\Delta_+ = -3\frac{\omega_Q}{\omega_r}$. This yields the $|0\rangle \rightarrow |-1\rangle$ component of the deuterium powder pattern. The $|+1\rangle \rightarrow |0\rangle$ component is obtained by reflection of the calculated spinning sidebands about the centerband. For the calculation of the spinning sideband intensities, the trapezoidal rule was used to approximate the integrals with 64 subdivisions over θ, α, and β. The spinning sideband pattern meets the normalization condition, $\sum_{-N}^{N} I_k = 1$, where I_k is the intensity of the k–th spinning sideband in the quadrupolar MAS spectrum where there are N unique sidebands (we assume that the chemical shift anisotropy is negligible). No corrections for finite pulse lengths[91,92] were made.

The quality of the fit between the experimental and simulated spinning sideband patterns was assessed by inspection of stick spectra of the residuals and by the value of χ_ν^2[93]. χ^2 is obtained from the experimental and simulated spinning sidebands by

$$\chi^2 \equiv \sum_{k=0}^{N} \frac{\left[I_k^{exp} - I_k^{calc}\right]^2}{\sigma^2_{integral(k)}} \qquad (5.1)$$

where the standard deviation of each spinning sideband integral, $\sigma_{integral(k)}$, is given by

$$\sigma_{integral(k)} = \sigma_{intensity}\, a \frac{I_k^{exp}}{max(I^{exp})} \tag{5.2}$$

and where the constant a is calculated from the relative intensities of the discrete data points that define the line shape for one of the most intense spinning sidebands,

$$a = \sqrt{(0.19^2 + 0.44^2 + 0.75^2 + 0.98^2 + 1^2 + 0.57^2 + 0.28^2 + 0.17^2)} \tag{5.3}$$

and where we make the assumption that all sidebands have a similar line shape. The standard deviation of the intensity for each data point in the spectrum, $\sigma_{intensity}$, is evaluated from the peak-to-peak noise level of the baseline, which shows a Gaussian distribution, and where the full-width at half-maximum, Γ, was measured

$$\sigma_{intensity} = \frac{\Gamma}{2.345} \tag{5.4}$$

and where the scale factor is specific for a Gaussian distribution. The value of the reduced chi-square, χ_ν^2, is determined from

$$\chi_\nu^2 = \frac{\chi^2}{N + 1} \tag{5.5}$$

where, in this case, there are no fitted parameters in the model and N is the number of unique sidebands in the symmetrized stick spectrum. When an appropriate model is fitted to the data, the value of χ_ν^2 is about 1, which indicates each data point deviates from by the model by about one standard deviation. The confidence limit for the model is close to 50 % so long as χ_ν^2 is close to 1, that is, less than 1.5.

5.3. Results

Shown in Figure 5.1 is the deuterium MAS NMR spectrum for K^2HCO_3 taken at a spin rate of 5 kHz. The signal-to-noise ratio for the most intense spinning sideband

is 43, which exceeds that obtainable in a non-spinning experiment for the same number of accumulations. In Figure 5.1b, we show a symmetrized stick spectrum generated by integrating each spinning sideband and the centerband of the MAS NMR spectrum. The stick spectrum shown in Figure 5.1c was calculated by the Herzfeld–Berger method using the values of the deuterium quadrupole coupling constant and asymmetry parameter listed in Table 5.1. There is a close correspondence between the experimental and calculated stick spectra, as demonstrated by a plot of the residuals and the rather small value of $\chi_\nu^2 = 0.97$. Shown in Figure 5.2 are the experimental and calculated deuterium MAS NMR spectra for $^2HIO_3$. Again the simulation, based upon the deuterium quadrupole coupling constant and asymmetry parameter from the double resonance NQR work of Poplett and Smith, models the experimental results well with $\chi_\nu^2 = 0.81$. Similar results were also obtained for Na^2HCO_3, as listed in Table 5.1. At this point, we concluded that, at least for these samples, simulated deuterium MAS NMR spectra can be reliably generated based upon deuterium quadrupole coupling constants and asymmetry parameters obtained from double resonance NQR spectroscopy.

However, the results for K^2HSO_4 are significantly different. Here, the experimental deuterium MAS NMR spectrum was not modeled well using the quadrupolar parameters from the double resonance NQR work. One possible explanation is based upon deuterium jump motions in the hydrogen bonding network that reorient the electric field gradient tensor with respect to the laboratory axis system. In the double resonance NQR work, reorientation does not affect the frequency of the zero magnetic field transition whereas in the NMR experiment, the transition frequency between the deuterium spin states is affected. Because of the discrepancy between the simulated and experimental spectra, K^2HSO_4 was excluded from the next series of experiments employing mixtures.

Two physical mixtures were prepared. In neither case was there evidence of a solid state reaction between the components. The first mixture, consisting of an equimolar ratio of K^2HCO_3 and $^2HIO_3$, yielded the deuterium MAS NMR spectrum at a spin rate of 5 kHz shown in Figure 5.3. The stick spectrum in Figure 5.3b was made by summing, with equal weighting, the independently calculated spectra of the two components, K^2HCO_3 and $^2HIO_3$. There is a close correspondence between the experimental and the simulated spectra of the two component model, with $\chi^2_\nu = 0.87$. Shown in Figure 5.3d is the simulated stick spectrum using values for the quadrupole coupling constant and asymmetry parameter that are the average of those for K^2HCO_3 and $^2HIO_3$. The large value of $\chi^2_\nu = 9.05$ indicates that the averaged model fits the experimental spectrum poorly. Therefore, two inequivalent deuterium sites having a difference in quadrupole coupling constant of 30.4 kHz are resolved in the MAS NMR spectrum with a spin rate of 5 kHz.

On the other hand, the second mixture composed of equal molar ratios of K^2HCO_3 and Na^2HCO_3 shows equally good fits to both the two components and the averaged models, with values of χ^2_ν less than 1.5 and small residuals in both fits. The inability to resolve the two inequivalent deuterium sites may be due to a smaller difference in quadrupole coupling constant, 4.8 kHz, relative to a spin rate of 5 kHz. Also, there may be a small compensating effect in the asymmetry parameters for the two components that makes the singularities in the powder patterns for the two components occur at similar frequencies.

From these observations, it appears that there is a correspondence between the magnitude of the difference of the quadrupole coupling constants and the MAS spin rate. Shown in Figure 5.4 are the deuterium MAS NMR spectra calculated at different spin rates, ν_r = 10, 5, and 2.5 kHz, for both one and two component systems. For the calculation of the one component spectra, the value of the deuterium quadrupole

coupling constant is 80 kHz. For the calculation of the two component spectra, the deuterium quadrupole coupling constants are 85 and 75 kHz for two sites of equal abundance. The differences clearly show the effect of the spin rate upon the ability to resolve the two inequivalent deuterium sites, with $\nu_r = 2.5$ kHz yielding the greater resolution.

5.4. Discussion

Based on MAS spectra of pure substances and of mixtures, combined with calculated MAS spectra, we conclude that low-speed MAS is preferred over high-speed MAS for resolving multiple deuterium sites based on the difference in the quadrupole coupling constants.

Aside from spin rate, another factor that could, in principle, affect an attempt to resolve multiple deuterium sites is the presence of large chemical shift anisotropy. At the magnetic field strength and spin rate used here, 4.7 Tesla and 5 kHz, respectively, an anisotropy of 30 ppm[94] is small with respect to the separation between spinning sidebands. In the experiments described herein, no corrections for chemical shift anisotropy effects were deemed necessary, though this may not be the case at higher fields in other low-speed MAS experiments.

Acknowledgments. The purchase of the Bruker MSL 200 NMR spectrometer was made possible by NSF grant CHE–8711788. The support of the National Science Foundation (CHE–8715517) and the Louisiana Board of Regents' through the Louisiana Educational Quality Support Fund are gratefully acknowledged. Leslie G. Butler is a Fellow of the Alfred P. Sloan Foundation (1989–1991). We thank Prof. Niels Chr. Nielsen for supplying a preprint on MAS NMR of quadrupolar nuclei.

Figure 5.1.

Deuterium MAS NMR spectra of K^2HCO_3 at a spin rate of 5 kHz. (a) Experimental spectrum showing a series of spinning sidebands (N = 25) acquired using a simple Bloch decay. Experimental parameters are as follows: NS = 264, RD = 60 s, and LB = 300 Hz. The linewidth, $\Delta\nu$, of the most intense spinning sideband is 610 Hz (FWHH). (b) Experimental stick spectrum recreated from the symmetrized spinning sideband integrals. (c) Calculated spectrum using $e^2q_{zz}Q/h$ = 153.65 kHz and η = 0.191. (d) The residuals between the experimental and calculated stick spectra.

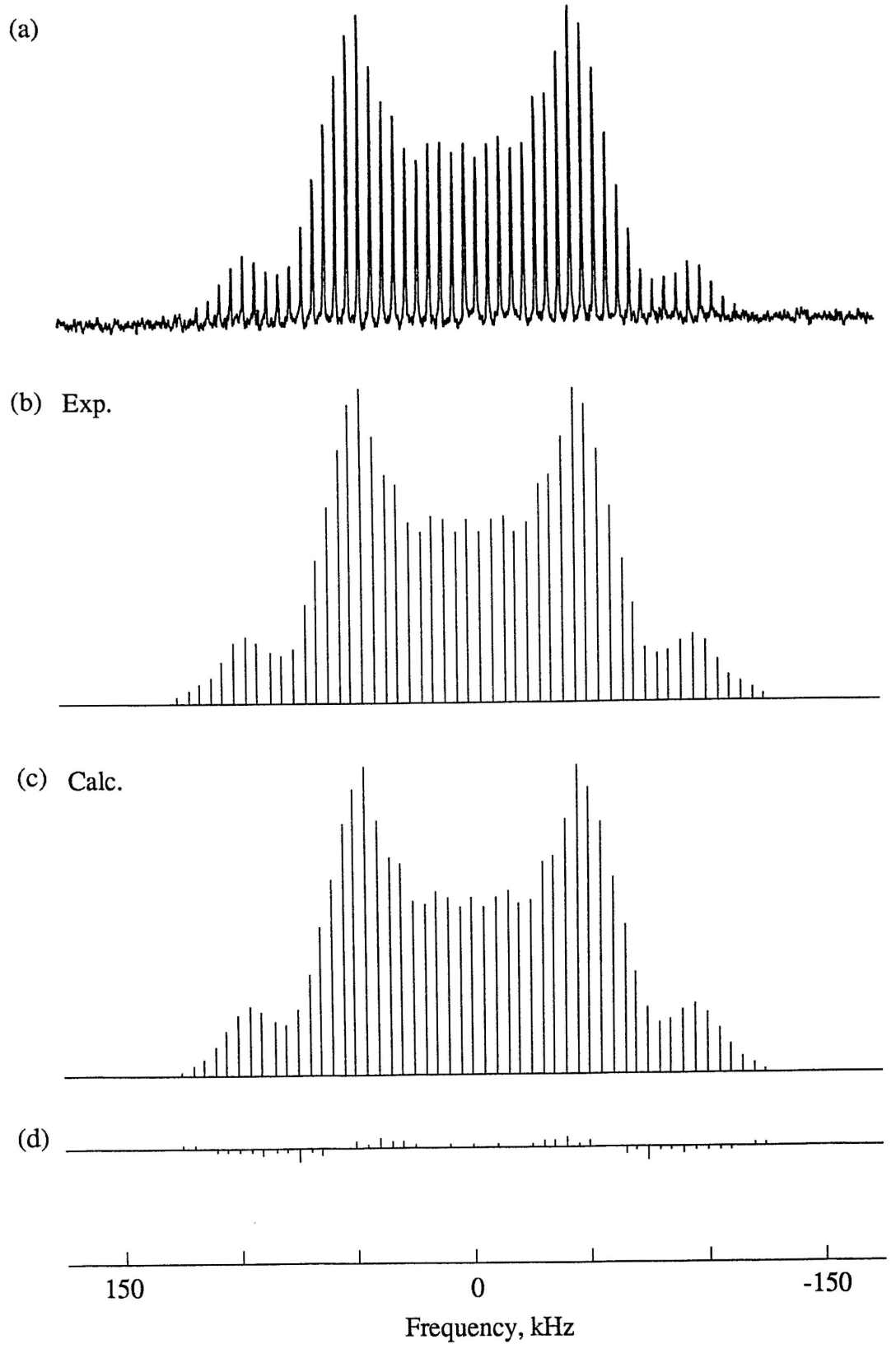
(a)
(b) Exp.
(c) Calc.
(d)
150
0
-150
Frequency, kHz

Figure 5.2.

Deuterium MAS NMR spectra of $^2HIO_3$ at a spin rate of 5 kHz. (a) Experimental spectrum, $\Delta\nu$ = 915 Hz, showing a series of spinning sidebands (N = 30) acquired using a simple Bloch decay. Experimental parameters are as follows: NS = 240, RD = 60 s, and LB = 300 Hz. (b) Experimental stick spectrum recreated from the symmetrized spinning sideband integrals. (c) Calculated spectrum using $e^2q_{zz}Q/h$ = 184.1 kHz and η = 0.125. (d) The residuals between the experimental and calculated stick spectra.

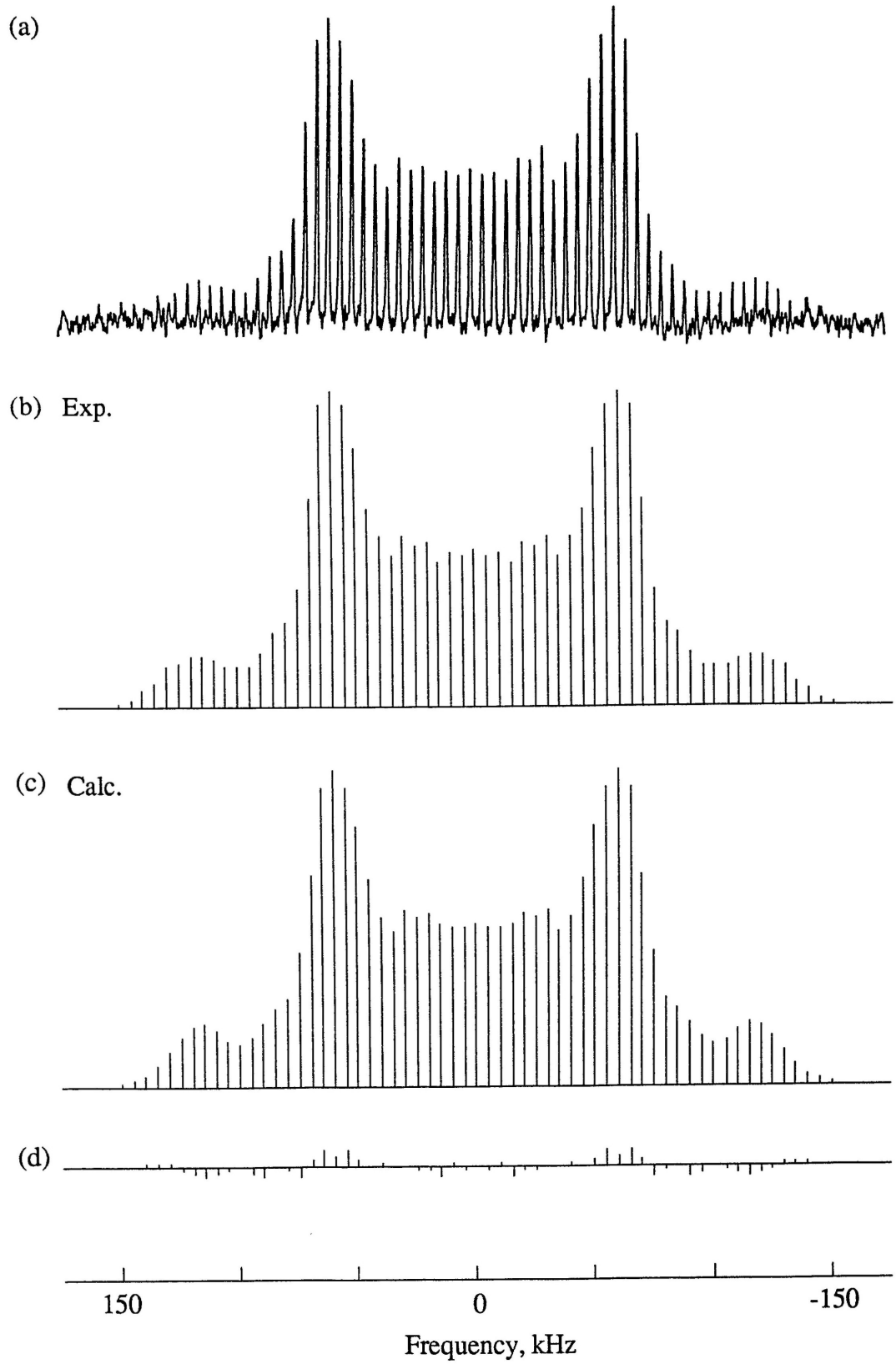
(a)
(b) Exp.
(c) Calc.
(d)
150
0
-150
Frequency, kHz

Figure 5.3.

Deuterium MAS NMR spectra of equal molar ratios of K^2HCO_3 and $^2HIO_3$ at a spin rate of 5 kHz. (a) Experimental spectrum, $\Delta\nu$ = 760 Hz, showing a series of spinning sidebands (N = 30) acquired using a simple Bloch decay. Experimental parameters are as follows: NS = 310, RD = 60, and LB = 300 Hz. (b) Calculated spectrum made by summing the spinning sideband intensities of K^2HCO_3 and $^2HIO_3$ components. (c) The residuals between the experimental (a) and calculated (b) spectra. (d) Calculated spectrum using an average quadrupole coupling constant and asymmetry parameter from K^2HCO_3 and $^2HIO_3$; $e^2q_{zz}Q/h$ = 168.875 kHz and η = 0.158. (e) The residuals between the experimental (a) and calculated (d) spectra.

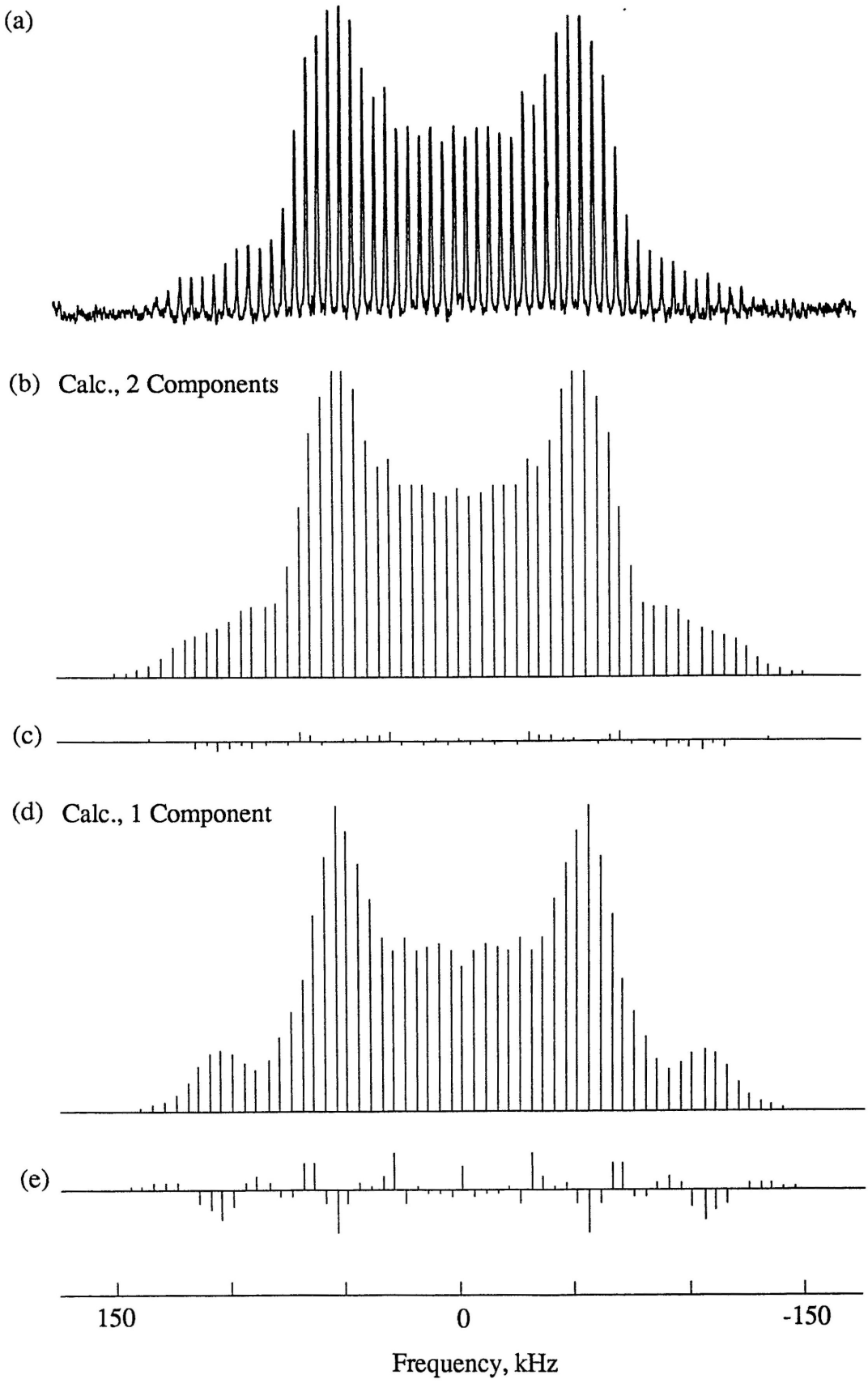
(a)
(b) Calc., 2 Components
(c)
(d) Calc., 1 Component
(e)
150
0
-150
Frequency, kHz

Figure 5.4.

Calculated deuterium MAS NMR spectra at spin rates, ν_r, of (a) 10, (b) 5, and (c) 2.5 kHz. Top: calculated stick spectra of a single component with $e^2q_{zz}Q/h$ = 80 kHz, η = 0. Middle: calculated stick spectra for two components of equal abundance; $e^2q_{zz}Q/h$ = 85 and $e^2q_{zz}Q/h$ = 75 kHz. Bottom: differences between the one and two component stick spectra.

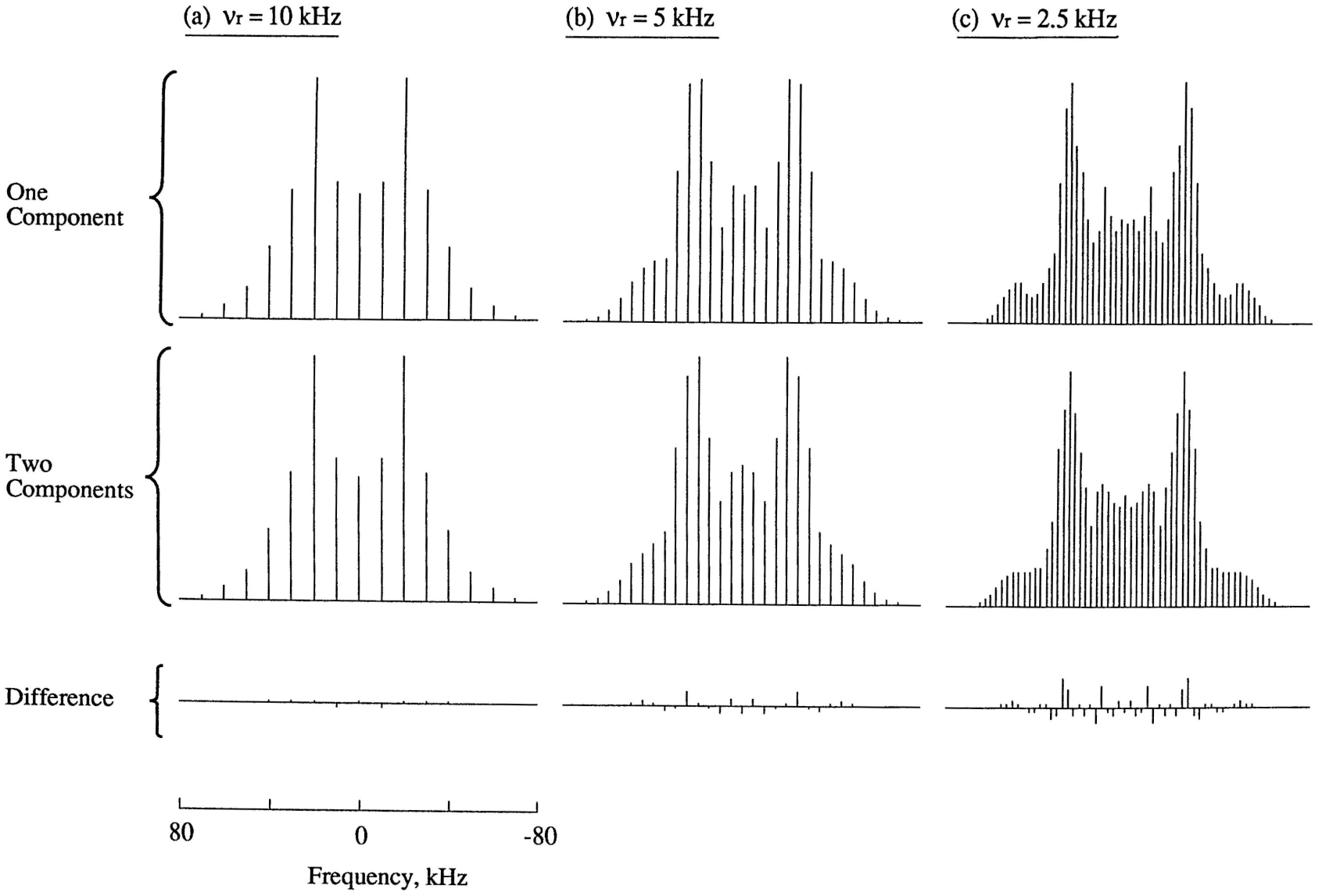
(a) νr = 10 kHz
(b) νr = 5 kHz
(c) νr = 2.5 kHz
One Component
Two Components
Difference
80
0
-80
Frequency, kHz

Table 5.1. Quality of the Fit Between Experimental and Simulated Deuterium MAS NMR Spectra.

Compound	$e^2q_{zz}Q/h$, kHz [a]	η [a]	χ_ν^2
K^2HCO_3	153.65 (3)	0.191 (2)	0.97
$^2HIO_3$	184.1 (2)	0.125 (2)	0.81
Na^2HCO_3	148.8 (10)	0.182 (5)	1.49
K^2HSO_4	175.2 (4)	0.160 (4)	7.43
$K^2HCO_3 + {}^2HIO_3$	(two components)		0.87
	(averaged)		9.05
$K^2HCO_3 + Na^2HCO_3$	(two components)		1.36
	(averaged)		1.40

[a] From $^1H/^2H$ double resonance NQR (ref *89*).

References for Chapter 5

(80) Soda, G.; Chiba, T. *J. Chem. Phys.* **1969**, *50*, 439-55.

(81) Ireland, P. S.; Olson, L. W.; Brown, T. L. *J. Am. Chem. Soc.* **1975**, *97*, 3548-9.

(82) Thayer, A. M.; Pines, A. *Acc. Chem. Res.* **1987**, *20*, 47-53.

(83) Edmonds, D. T. *Phys. Rep.* **1977**, *29C*, 233-90.

(84) Edmonds, D. T.; White, A. A. L. *J. Mang. Reson.* **1978**, *31*, 149-59.

(85) Edmonds, D. T.; Hunt, M. J.; Mackay, A. L. *J. Magn. Reson.* **1975**, *20*, 505-14.

(86) Jarrett, W. L.; Farlee, R. D.; Butler, L. G. *Inorg. Chem.* **1987**, *26*, 1381-3.

(87) Jarrett, W. L.; Guo, K.; Jackish, M. A.; Butler, L. G. *J. Magn. Reson.* **1989**, *82*, 76-85.

(88) Jackisch, M. A.; Jarrett, W. L.; Guo, K.; Fronczek, F. R.; Butler, L. G. *J. Am. Chem. Soc.* **1988**, *110*, 343-7.

(89) Poplett, I. J. F.; Smith, J. A. S. *J. Chem. Soc., Faraday Trans. 2* **1978**, *74*, 1077-87.

(90) Herzfeld, J.; Berger, A. E. *J. Chem. Phys.* **1980**, *73*, 6021-30.

(91) Bloom, M.; Davis, J. H.; Valic, M. I. *Can. J. Phys.* **1980**, *58*, 1510-7.

(92) Henrichs, P. M.; Hewitt, J. M.; Linder, M. *J. Magn. Reson.* **1984**, *60*, 280-98.

(93) Bevington, P. R. *Data Reduction and Error Analysis for the Physical Sciences*; McGraw-Hill: New York, 1969.

(94) Mehring, M. *Principles of High Resolution NMR in Solids*; Springer-Verlag: New York, 1983.

CHAPTER 6

Nonlinear Least-Squares Fitting Procedure for Solid-State NMR Powder Patterns

6.1. Introduction

The solid-state NMR line shape can furnish information on molecular geometry[95], electronic structure of chemical bonds[96], and motion of molecules in dynamic systems[97]. Information can be extracted from the overall line shape of the NMR powder pattern, which is the superposition of individual lines resulting from the resonance of each microcrystalline orientation relative to the applied magnetic field. Alternative approaches based upon critical frequencies in the powder pattern have been proposed and successfully applied for the purpose of extracting characteristic NMR parameters.[98]

In this chapter, a fitting procedure using a nonlinear least-squares analysis is described. The Levenberg–Marquardt algorithm is recoded in Matlab and used to extract characteristic NMR parameters by a fit of the experimental NMR powder pattern. Four examples are shown. The principal elements of the ^{13}C chemical shielding tensor are obtained from the ^{13}C powder pattern for the $^{13}CH_2$ unit in *cis*-(μ-CH_2)(μ-CO)[FeCp(CO)]$_2$ and for $K_2Pt(CN)_4 \cdot 3H_2O$. Also, the dipolar coupling tensor is used to determine d(C–H) and $\angle$H–C–H from the proton-coupled ^{13}C powder pattern. The deuterium quadrupole coupling constant and asymmetry parameter are determined from the powder pattern for the bridging deuterium site in $[Et_4N][^2HCr_2(CO)_{10}]$.

6.2. Levenberg–Marquardt algorithm[99]

The model to be fitted is

$$y = y\_calc(x, a) \tag{6.1}$$

where x is an independent variable and a is a parameter,which is a q-dimensional vector, $a = [a_1\ a_2 \cdots a_q]$. The value of χ^2 is calculated by

$$\chi^2 = \sum_{i=1}^{N} \left[\frac{(y\_exp(x_i) - y\_calc(x_i, a))^2}{\sigma^2} \right] \tag{6.2}$$

where σ is the standard deviation of experimental data, N is the number of sampled data points, and $y\_calc(x_i, a)$ and $y\_exp(x_i)$ are the fitted and experimental data, respectively.

Let us expand χ^2 to second order in a Taylor's expansion with respect to the parameter a

$$\begin{aligned} \chi^2 \equiv \chi_0^2 + & \left\{ \frac{\partial \chi_0^2}{\partial a_1} \delta a_1 + \frac{\partial \chi_0^2}{\partial a_2} \delta a_2 + \cdots + \frac{\partial \chi_0^2}{\partial a_q} \delta a_q \right\} \\ & + \frac{1}{2} \left\{ \frac{\partial^2 \chi_0^2}{\partial a_1^2} \delta a_1^2 + \frac{\partial^2 \chi_0^2}{\partial a_1 \partial a_2} \delta a_1 \delta a_2 + \cdots + \frac{\partial^2 \chi_0^2}{\partial a_1 \partial a_q} \delta a_1 \delta a_q + \cdots + \right. \\ & \left. \frac{\partial^2 \chi_0^2}{\partial a_q \partial a_1} \delta a_q \delta a_1 + \frac{\partial^2 \chi_0^2}{\partial a_q \partial a_2} \delta a_q \delta a_2 + \cdots + \frac{\partial^2 \chi_0^2}{\partial a_q^2} \delta a_q^2 \right\} \end{aligned} \tag{6.3}$$

where χ_0^2 is the value of χ^2 at some starting point. From eq 6.2, first and second derivatives of χ^2 with respect to a can be written as follows:

$$\frac{\partial \chi^2}{\partial a_k} = -2 \sum_{i=1}^{N} \left[\frac{1}{\sigma^2} (y\_exp(x_i) - y\_calc(x_i, a)) \frac{\partial y\_calc(x_i, a)}{\partial a_k} \right] \tag{6.4a}$$

$$\begin{aligned} \frac{\partial^2 \chi^2}{\partial a_k \partial a_j} = 2 \sum_{i=1}^{N} \frac{1}{\sigma^2} \left[\frac{\partial y\_calc(x_i, a)}{\partial a_k} \frac{\partial y\_calc(x_i, a)}{\partial a_j} - \right. \\ \left. (y\_exp(x_i) - y\_calc(x_i, a)) \frac{\partial^2 y\_calc(x_i, a)}{\partial a_k \partial a_j} \right] \end{aligned} \tag{6.4b}$$

where k = 1, 2, $\cdots$, and q.

Now, let us define

$$\delta a = [\delta a_1 \ \delta a_2 \cdots \delta a_q] \tag{6.5a}$$

$$\beta = \left[\beta_1 \ \beta_2 \cdots \beta_q\right] \tag{6.5b}$$

$$\alpha = \begin{bmatrix} \alpha_{11} & \alpha_{12} & \cdots & \alpha_{1q} \\ \alpha_{21} & \alpha_{22} & \cdots & \alpha_{2q} \\ \cdots & \cdots & \cdots & \cdots \\ \alpha_{q1} & \alpha_{q2} & \cdots & \alpha_{qq} \end{bmatrix} \tag{6.5c}$$

where β is the gradient vector with dimension given by the number of parameters and α is the curvature matrix:

$$\beta_k = -\frac{1}{2}\frac{\partial \chi_0^2}{\partial a_k} \tag{6.6a}$$

$$\alpha_{kj} = \frac{1}{2}\frac{\partial^2 \chi_0^2}{\partial a_k \partial a_j} \tag{6.6b}$$

Then, eq 6.3 can be written in a simplified form

$$\chi^2 \equiv \bar{\chi}^2 = \chi_0^2 - 2\,\delta a\ \beta^T + \delta a\ \alpha\ \delta a^T \tag{6.7}$$

where T represents the transpose. In the above eq 6.7, χ^2 is approximated to $\bar{\chi}^2$ by a Taylor series. The method of least squares uses the above quadratic approximation of χ^2 to find fitted parameters, a, where the gradient of the function $\bar{\chi}^2$ is zero. This yields a set of N simultaneous linear equations and the values of δa come from the solution of this set of linear equations. The gradient of $\bar{\chi}^2$ with respect to parameters a is represented by

$$\frac{\partial \bar{\chi}^2}{\partial a} \equiv \left[\frac{\partial \bar{\chi}^2}{\partial a_1} \ \frac{\partial \bar{\chi}^2}{\partial a_2} \cdots \frac{\partial \bar{\chi}^2}{\partial a_q}\right] \tag{6.8}$$

Each element of the above vector $\frac{\partial \bar{\chi}^2}{\partial a_k}$ can be found from eq 6.3, that is,

$$\frac{\partial \bar{\chi}^2}{\partial a_k} = \frac{\partial \chi_0^2}{\partial a_k} + \sum_{j=1}^{q} \frac{\partial \chi_0^2}{\partial a_k \partial a_j}\,\delta a_j \tag{6.9}$$

From eq 6.8 and 6.9, the gradient of $\overline{\chi}^2$ can be written

$$\frac{\partial \overline{\chi}^2}{\partial a} = -2\beta + 2\,\delta a\,\alpha \tag{6.10}$$

Therefore, for a set of parameter a for which the gradient of $\overline{\chi}^2$ is zero, we can see this relationship

$$\delta a = \beta\,\alpha' \tag{6.11}$$

must be satisfied. The following expression is used to modify α.

$$\alpha'_{jk} = \begin{cases} \alpha_{jk}(1+\lambda) & \text{for } j = k \\ \alpha_{jk} & \text{for } j \neq k \end{cases} \tag{6.12}$$

If λ is very small, eq 6.12 are similar to the solution of eq 6.11. If λ is very large, the diagonal terms of the curvature matrix dominate and the matrix equation degenerates into N separate equations.

$$\beta_k \equiv \lambda\,\delta a_k\,\alpha_{kk} \tag{6.13}$$

Given an initial guess for the set of fitted parameters, a, the recommended Marquardt recipe is as follows:[99]

1. Compute $\chi^2(a)$ from eq 6.2.
2. Start initially with $\lambda = 0.001$.
3. Compute δa from eq 6.11 and evaluate $\chi^2(a + \delta a)$ with this choice of λ.
4. If $\chi^2(a + \delta a) \geq \chi^2(a)$, increase λ by a factor of 10, go back to step 3.
5. If $\chi^2(a + \delta a) < \chi^2(a)$, decrease λ by a factor of 10, consider a_new = a + δa to be the new starting point, and go back to step 3 substituting a_new for a.
6. The stopping criteria are $\lambda < 0.001$ or the reduction in χ^2 is less than 1.

7. The error limits for each parameter are calculated from the final values of the inverse curvature matrix, α^{-1}, as shown in eq 6.17.

For nonlinear parameter estimation, the following programs were recoded in Matlab, a vector-oriented programming language. Program 6.1 describes the Levenberg–Marquardt method which is attempting to minimize the value χ^2 of a fit between the experimental and calculated data points. This algorithm combines a gradient search with an analytical solution developed from linearizing the fitting function. The nonlinear fitting functions are described in Program 6.2. The functions, `ChemShift_functn` and `Dipole_ChemShift_functn` are used to calculate the proton-decoupled and proton-coupled ^{13}C proton-decoupled powder patterns, respectively, for *cis*-(μ-$^{13}CH_2$)(μ-CO)[FeCp(CO)]$_2$. Also, the function `ChemShift_PtCN_functn` is used to calculate the (^{14}N, ^{195}Pt)-coupled ^{13}C powder pattern for $K_2Pt(CN)_4 \cdot 3H_2O$. The function `Deu_functn` is used to calculate the deuterium powder pattern for $[Et_4N][^2HCr_2(CO)_{10}]$. The derivatives of the fitting function are evaluated numerically with respect to each of the parameters, a_j, with the function `CurFit_nonanal` , described in Program 6.3:

$$\frac{\partial y\_calc(x,a)}{\partial a_j} \cong \frac{1}{2\Delta a_j}\{[y\_calc(x,a_1;a_2 \cdots a_{j-1};a_j+\Delta a_j;a_{j+1};a_q)] - [y\_calc(x,a_1;a_2 \cdots a_{j-1};a_j-\Delta a_j;a_{j+1};a_q)]\} \quad (6.14)$$

The value of χ^2 is calculated by the use of the function `CurFit_chisqr` , described in Program 6.4.

6.3. Fitting Procedures

There are several steps in the procedure to extract the NMR parameters from the NMR powder pattern. First, the fitting procedure is begun by visual examination of the NMR powder pattern to make initial guesses at parameter values, a. This step is very important because it starts the parameter values in a region of parameter space which contains the global minimum of χ^2, thus avoiding the local minima outside this region. The parameter values, a, are the row vector consisting of the NMR parameters and the adjustable parameters. The NMR parameters characterize the line shape of the NMR powder pattern. For the fitting function `ChemShift_functn` , the NMR parameters are the principal elements of the chemical shielding tensor, δ_{11} and δ_{22}; the value of δ_{33} can be extracted from the isotropic chemical shift, δ_{11}, and δ_{22}. For the fitting function `Dipole_ChemShift_functn` , d(C–H) and ∠H–C–H are used as variables for calculating the dipolar coupling tensor, with fixed principal elements of the chemical shielding tensor. For the fitting function `ChemShift_PtCN_functn` , the NMR parameters are the principal elements of the chemical shielding tensor, δ_{11} and δ_{33}, with fixed value of δ_{iso} and d(C–N) and d(P–Pt). In the case of the fitting function `Deu_functn`, the NMR parameters include the deuterium quadrupole coupling constant and asymmetry parameter. Because the value of the asymmetry parameter should range from 0 to 1, inclusive, two "IF" statements are used, as shown in Programs 6.1 and 6.3. The adjustable parameters, such as scale factor, baseline offset, and frequency offset, can also be used to reduce the value of χ^2. These functions yield powder pattern line shapes by simple summation over the Euler angles, θ and χ, with constant angle step size. More elaborate tiling schemes[100] have been developed, but were not tested here.

Second, the experimental data are obtained from the exponentially filtered, Fourier-transformed, and manually phased NMR powder pattern acquired by using a

Bruker MSL 200 solid-state NMR spectrometer. Usually, 512 or 1024 data points are sampled from the whole spectrum and they are denoted by x(i) and y_exp(i). Each data point has an associated uncertainty. The standard deviation, σ, is evaluated from the peak-to-peak noise level of the baseline of the experimental spectrum, which shows a Gaussian distribution, and where the full-width at half-maximum, Γ, was measured.

$$\sigma = \frac{\Gamma}{2.345} \tag{6.15}$$

and where the scale factor is specific for a Gaussian distribution. Figure 6.1a shows the peak-to-peak noise level of the baseline of the experimental deuterium powder pattern for $[Et_4N][^2HCr_2(CO)_{10}]$. The standard deviation, $\sigma = 3.75$, is evaluated from the value of Γ in a Gaussian distribution, as shown in Figure 6.1b.

Third, the values for the vector Δa are assigned for later use in calculating numerical derivatives. Typically, Δa is ~10 % of a.

Finally, the Levenberg–Marquart algorithm, including three sub-routines, is ready for running. The first call provides χ^2_old from an initial guess of the parameter values. If the second call with $\lambda = 0.001$ succeeds, then χ^2_new becomes smaller than χ^2_old and λ decreases by a factor of 10 and parameter values, a, are replaced by a_new (= a + δa). If this step fails, λ grows by a factor of 10. We must call this routine repeatedly until convergence is achieved to minimize the value of χ^2 between the experimental and the best fitted data points.

Best fitted parameters (a_new), best fitted spectral points (y_calc), and the value of χ^2 are given by the fitting procedure as output variables. The quality of the fit is judged to be good if no systematic deviations are observed in a plot of the residuals, y_exp–y_calc, and the value of χ^2_ν is approximately 1 to 1.5. The value of the reduced chi-square, χ^2_ν, is given by

$$\chi^2_\nu = \frac{\chi^2}{N - \nu + 1} \tag{6.16}$$

where N and ν represent the number of data points and the number of fitted parameters, respectively.

The error limits, σ_{a_i}, for each parameter a are determined from the diagonal elements of the inverse of the curvature matrix, α^{-1},

$$\sigma_{a_i} = \sqrt{\left(\alpha^{-1}\right)_{ii}} \tag{6.17}$$

6.4. Fitting Results

Here, we recall Figures 2.3, 2.5, 3.3a, and 4.2c. Shown in Figure 2.3 are the ^{13}C chemical shift powder pattern for the $^{13}CH_2$ unit in *cis*-(μ-CH_2)(μ-CO)[FeCp(CO)]$_2$, the nonlinear least-squares fit to the experimental spectrum, and the residuals. The results are listed in Table 6.1. The principal elements of the ^{13}C chemical shielding tensor for two crystallographically inequivalent components, monoclinic and triclinic forms (40:60 mixture), are used to fit. The value of $\chi^2_\nu = 2.0$ indicates that this model is relatively tenable. Corrections for finite pulse lengths[101] and anisotropic cross polarization[102] may reduce the value of χ^2_ν. The important aspect with these results is that the paramagnetic contribution derived from the chemical shielding tensor is related to a molecular orbital description of the bonding at the methylene carbon site.

The proton-coupled ^{13}C powder pattern for the $^{13}CH_2$ unit in *cis*–(μ-$^{13}CH_2$)(μ-CO)[FeCp(CO)]$_2$ is fitted while allowing d(C–H) and ∠H–C–H to vary, with fixed values of the principal elements of the ^{13}C chemical shielding tensor. The results of the nonlinear least-squares fit are shown in Figure 2.6 and listed in Table 6.2. The critical feature is that the structural information at the bridging methylene unit

can be extracted from proton-coupled ^{13}C powder pattern by the analysis of the dipolar coupling to protons.

Shown in Figure 4.2c are the (^{14}N, ^{195}Pt)-coupled ^{13}C powder pattern for $K_2Pt(CN)_4 \cdot 3H_2O$. Only ^{13}C chemical shielding tensor components are fitted to the best calculated model, with constant contributions obtained from the dipolar and quadrupolar interactions to ^{14}N and the dipolar and J coupling to ^{195}Pt. The results are summarized in Table 6.3.

Figure 3.3a shows the deuterium powder pattern obtained for $[Et_4N][^2HCr_2(CO)_{10}]$, the nonlinear least-squares fit to the experimental spectrum, and the residuals. The results are listed in Table 6.4. The residuals show no obvious systematic deviation and the value of χ^2_ν is 2.6. Again, no correction for finite pulse lengths was made. The NMR parameters for the deuterated site, the quadrupole coupling constant and the asymmetry parameter, are extracted from the fit of the deuterium powder pattern. The quadrupole coupling constant is a measure of the magnitude of the electric field gradient at the deuterium site while the asymmetry parameter gives information about the shape of the electric field gradient.

6.5. Conclusions

The Levenberg–Marquardt nonlinear least-squares fitting procedure has been used for the extraction of the characteristic NMR parameters. The best fitted NMR powder patterns include the calculation of quadrupolar, dipolar, and dipole- and quadrupole-coupled chemical shielding tensors. For several reasons, this work provides a textbook example for line shape analysis of the NMR powder patterns. We note the following:

1. The non-linear least-squares fitting procedure (Levenberg–Marquardt algorithm) is simple and program implementation, with a vector–oriented programming language, is easy;

2. The calculation of residuals between the experimental and calculated spectra and the value of χ_v^2 provide the opportunity to judge the quality of the fit, and;
3. The computation time is not excessively long. Typically, the line shape is recalculated 30–60 times during the non-linear least-squares fit.

Figure 6.1.

Evaluation of the standard deviation from the experimental spectrum for $[Et_4N][^2HCr_2(CO)_{10}]$. (a) Peak-to-peak noise level of the baseline of the spectrum. (b) Gaussian distribution of the noise; $\Gamma = 8.8$, thus $\sigma = 3.75$.

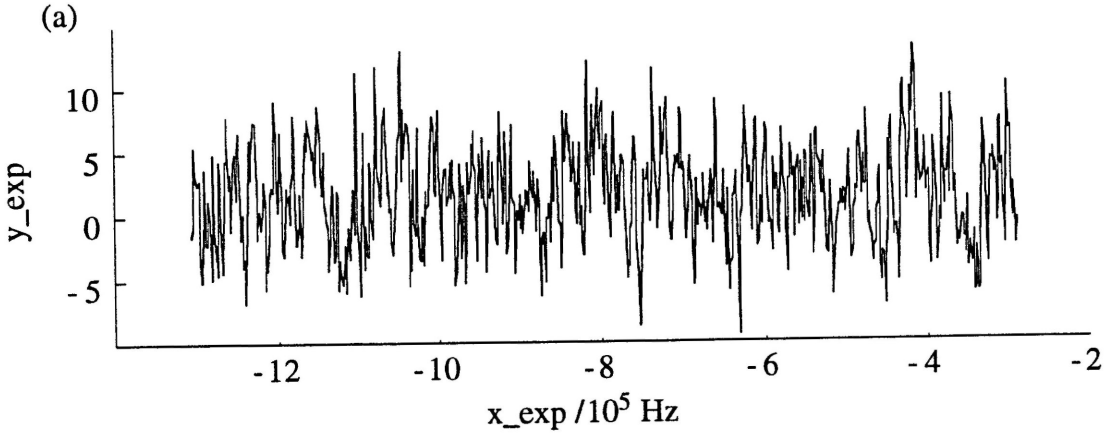
(a)
y_exp
10
5
0
-5
-12
-10
-8
-6
-4
-2
x_exp /10^5 Hz

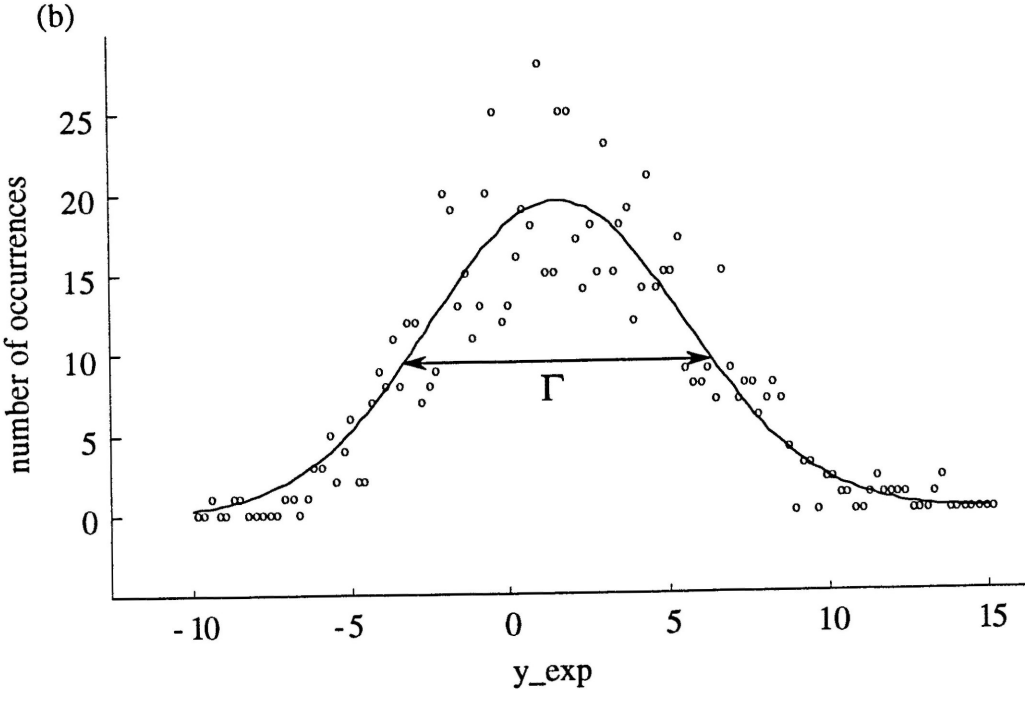
(b)
number of occurrences
25
20
15
10
5
0
Γ
-10
-5
0
5
10
15
y_exp

Table 6.1. Results of a Nonlinear Least-Squares Fit of the Proton-Decoupled ^{13}C Powder Pattern for the $^{13}CH_2$ unit in Monoclinic *cis*-(μ-$^{13}CH_2$)(μ-CO)[FeCp(CO)]$_2$.

Fitted Parameters	
δ_{11}	365.7 (6) ppm
δ_{22}	75.5 (1) ppm
Baseline Offset	0.8 (1)
Scale Factor	1.0 (1)
Fixed Parameters [a]	
δ_{iso}	139.0 ppm
Input Variables	
Standard Deviation	2.0
deg	2°
LB	1000 Hz
Δa	10 %
Other Parameters	
χ^2_ν	2.0
CPU_Time on VAX 3200	20 hr

[a] ^{13}C chemical shielding tensor elements for Cp ring are fixed; $\delta_{11} = \delta_{22} = 122$ and $\delta_{33} = 22$ ppm.

Table 6.2. Results of a Nonlinear Least-Squares Fit of the Proton-Coupled ^{13}C Powder Pattern for the $^{13}CH_2$ unit in Monoclinic *cis*-(μ-$^{13}CH_2$)(μ-CO)[FeCp(CO)]$_2$.

Fitted Parameters	
d(C–H)	1.122 (3) Å
∠H–C–H	110.8 (4)°
Baseline Offset	0.4 (1)
Scale Factor	1.0 (3)
Fixed Parameters	
δ_{11}	365.7 (6) ppm
δ_{22}	75.5 (1) ppm
δ_{33}	–24.2 (6) ppm
Input Variables	
Standard Deviation	2.0
deg	5°
LB	3000 Hz
Δa	10 %
Other Parameters	
χ^2_ν	2.1
CPU_Time on VAX 3200	140 hr

Table 6.3. Results of a Nonlinear Least-Squares Fit of the (^{14}N, ^{195}Pt)-Coupled ^{13}C Powder Pattern for $K_2Pt(CN)_4 \cdot 3H_2O$.

Fitted Parameters	
δ_{11}	251.8 (5) ppm
δ_{33}	–94.2 (4) ppm
Baseline Offset	5.2 (1)
Scale Factor	0.99 (1)
Frequency Offset	48.2 (6) Hz
Fixed Parameters	
δ_{iso}	127.9 ppm
d(C–N)	1.11 Å
d(C–Pt)	2.35 Å
$^1J_{C-Pt}$	1034 Hz
Input Variables	
Standard Deviation	3.6
deg	2°
LB	1000 Hz
Δa	10 %
Other Parameters	
χ^2_ν	1.3
CPU_Time on VAX 3200	45 hr

Table 6.4. Results of a Nonlinear Least-Squares Fit of the Deuterium Powder Pattern for the Bridging Deuterium Site in $[Et_4N][^2HCr_2(CO)_{10}]$.

Fitted Parameters	
Quadrupole Coupling Constant	85.4 (1) kHz
Asymmetry Parameter	0.034 (1)
Baseline Offset	6.9 (1)
Scale Factor	1.0 (1)
Frequency Offset	2.27 (4) kHz
Input Variables	
Standard Deviation	3.75
deg	2°
LB	3000 Hz
Δa	5 %
Other Parameters	
χ_ν^2	2.6
CPU_Time on VAX 3200	11 hr

Program 6.1. Levenberg–Marquardt Nonlinear Least-Squares Algorithm.

```
%  Description of Parameters
%  sigma      -  Standard Deviations for y_exp data points
%  FID_size   -  Number of Data Points
%  a          -  Array of Parameters
%  delta_a    -  Array of Increments for Parameter a
%  x          -  Array of Data Points for Freq_axis
%  y_calc     -  Array of Calculated Values
%  y_exp      -  Array of Experimental Values
%  chi_sqr    -  Chi-Square for Fit
%  lamda      -  Constant Factor set to 0.001 at the Beginning
%                of Each Fit


clg; clear; echo on; hold off;

global  FID_size sin_v cos_v Left_Spectrum HzPt Damped_exp
t0 = clock;  flops(0);  count = 0;

% x,y_exp  experimental data sets
load filename;

% Calculation of the standard deviation from the peak-to-peak
% noise level in the baseline
y_exp = 100*(y-min(y_exp))/max(y_exp);
s = 3.75;
sigma = s*ones(length(FID_size),1);
inv_sigma_sqr = (sigma.^2).\1;
inv_sigma_sqr = inv_sigma_sqr(:);

FID_size = number of data points ;
SF = resonance frequence ;  % 30.709e6 for deuterium and
                            % 50.301e6 for carbon
SW = x(length(x)) - x(1);
Dwell_time = 1/SW;
Time_axis = (0:FID_size-1)*Dwell_time;
HzPt = (SW)/(FID_size - 1);
Left_Spectrum = SF + x(1);
Right_Spectrum = SF + x(length(x));
Freq_axis = Left_Spectrum - SF + HzPt*(0:FID_size - 1);
x_calc = Freq_axis;
LB = 3000;
T2_L = 1/(pi*LB);
Damped_exp = exp(-Time_axis/T2_L);
deg = 2;
angles = 0:deg:90;
angles = angles*(2*pi/360);
sin_v = sin(angles);
cos_v = cos(angles);

% Parameters
% a(1), a(2), and a(5) are the adjustable parameters and
% a(3) and a(4) are the NMR parameters
a = [5.2, 0.94, 162, 0.05, 1] ;

V = [min(x) max(x) -0.1*max(y_exp) 1.1*max(y_exp)];
axis(V);
plot(x,y_exp,'o');
% errorbar(x,y_exp,sigma);
```

```
xlabel('Freq, kHz');
ylabel('Intensities'); hold on;

[y_calc] = Fitting function ;
           % ChemShift_Functn(x_calc,a,deg,LB,SF,x)
           % Dipole_ChemShift_functn(x_calc,a,deg,T2_L,SF,x)
           % ChemShift_PtCN_Functn(x_calc,a,deg,LB,SF,x)
           % Deu_Functn(x_calc,a,deg,LB,wL,SW)

plot(x_calc,y_calc);

alpha = zeros(length(a));
beta = zeros(1,length(a));
DA = zeros(1,length(a));

% Increasement of parameters
delta_a(1:5) = abs( 0.1*a(1:5));

% Initialize arrays
a_new = zeros(1,length(a));
dyda = zeros(length(x_calc),length(a));

% Degree of Freedom
N_free = length(y_calc) - length(a) + 1;

% Evaluate Chi Square at starting point and y_exp_new.
chi_sqr_old = CurFit_chisqr(y_exp,y_calc,inv_sigma_sqr);

% Evaluate ALPHA and BETA.
[dyda] = CurFit_nonanal(a,delta_a,deg,T2_L,SF,x);
for J = 1:length(a)
   for K = J:length(a)
      alpha(J,K) = sum(inv_sigma_sqr.*(dyda(:,J).*dyda(:,K)));
      alpha(K,J) = alpha(J,K);
   end;
end;
for K = 1:length(a)
      beta(K) = sum(inv_sigma_sqr.*((y_exp -
                                     y_calc).*dyda(:,K)));
end;

% Invert modified curvature matrix to find new parameters.
lambda = 0.001;
alpha_prime = alpha*(eye(length(a))*(1 + lambda));
DA = beta*inv(alpha_prime);

% Optional for deuterium powder pattern fitting
a_new = a + DA;
   if a_new(4)<0  a_new(4)=0;
      else a_new(4) = a_new(4);
   end
   if a_new(4)>1   a_new(4)=1;
      else a_new(4) = a_new(4);
   end

[y_calc] = Fitting function ;
           % ChemShift_Functn(x_calc,a,deg,LB,SF,x)
           % Dipole_ChemShift_functn(x_calc,a,deg,T2_L,SF,x)
           % ChemShift_PtCN_Functn(x_calc,a,deg,LB,SF,x)
           % Deu_Functn(x_calc,a,deg,LB,wL,SW)
chi_sqr_new = CurFit_chisqr(y_exp,y_calc,inv_sigma_sqr);
```

```
while chi_sqr_old > (chi_sqr_new + 1) | lambda >= 0.001
if chi_sqr_new >= chi_sqr_old
   lambda = lambda*10;
else
plot(x_calc,y_calc);
a = a_new;
lambda = lambda*0.1;
chi_sqr_old = chi_sqr_new;
[dyda] = CurFit_nonanal(a,delta_a,deg,T2_L,SF,x);
for J = 1:length(a)
   for K = J:length(a)
      alpha(J, K) = sum(inv_sigma_sqr.*(dyda(:,J).*dyda(:,K)));
      alpha(K,J) = alpha(J,K);
   end;
end;  % end J loop
   for K = 1:length(a)
      beta(K) = sum(inv_sigma_sqr.*((y_exp -
                                        y_calc).*dyda(:,K)));
   end;  % end K loop
end;  % end if-then-else conditional

alpha_prime = alpha*(eye(length(a))*(1+lambda));
DA =  beta*inv(alpha_prime);

% Optional for deuterium powder pattern fitting
a_new = a + DA;
   if a_new(4)<0  a_new(4)=0;
      else a_new(4) = a_new(4);
   end
   if a_new(4)>1   a_new(4)=1;
      else a_new(4) = a_new(4);
   end

[y_calc] =  Fitting function ;
            % ChemShift_Functn(x_calc,a,deg,LB,SF,x)
            % Dipole_ChemShift_functn(x_calc,a,deg,T2_L,SF,x)
            % ChemShift_PtCN_Functn(x_calc,a,deg,LB,SF,x)
            % Deu_Functn(x_calc,a,deg,LB,wL,SW)

chi_sqr_new = CurFit_chisqr(y_exp,y_calc,inv_sigma_sqr);

end;  % end of while loop

error = sqrt(diag(inv(alpha)))';
etime(clock,t0)
flops
count
save filename
```

Program 6.2a. Calculation of the Proton-Decoupled ^{13}C Powder Pattern.

```
% Four Parameters to be fitted
% a(1) = Baseline Offset,
% a(2) = Scale Factor,
% a(3) = Sigma_11 for monoclinic form , and
% a(4) = Sigma_22 for monoclinic form .

function [y_calc] = ChemShift_Functn(x_calc,a,deg,LB,SF,x)

% Instrument and calculation parameters
FID_size = 256;
SW = x(length(x)) - x(1);
Dwell_time = 1/SW;
HzPt = (SW)/(FID_size-1);
inv_HzPt = 1/HzPt;
Left_Spectrum = SF + x(1);
Right_Spectrum = SF + x(length(x));
Freq_axis = Left_Spectrum - SF + HzPt*(0:FID_size - 1);

% Initialize arrays for the calculated spectra
Spectrum_mono = zeros(1,FID_size);
Spectrum_tri  = zeros(1,FID_size);
Spectrum_Cp   = zeros(1,FID_size);
Spectrum = zeros(1,FID_size);

Iz = [0 0 1];
Bo = [0 0 1];
Bo = Bo';

% 13C chemical shielding tensor
% monoclinic_iso = 139.0 and triclinic_iso = 145.6 ppm
SigmaPA_mono = [a(3) 0 0; 0 a(4) 0;...
                0 0 (139e-6*3 - a(3) - a(4))];
SigmaPA_tri  = [(a(3) + 6.6e-6) 0 0; 0 (a(4) + 6.6e-6) 0;...
                0 0 (139e-6*3 - a(3) - a(4) + 6.6e-6)];
SigmaPA_Cp   = [120e-6 0 0; 0 120e-6 0; 0 0 20e-6];

% Averaging over beta(B) and alpha(A)
for B = 1:length(sin_vector)
   Rybeta  = [cos_vector(B) 0 sin_vector(B);0 1 0;...
              -sin_vector(B) 0 cos_vector(B)];
   Left_Side = Iz*Rybeta';
   Right_Side = Rybeta*Bo;

for A = 1:length(sin_vector)
   Rzalpha = [cos_vector(A) sin_vector(A) 0;...
              -sin_vector(A) cos_vector(A) 0;0 0 1];
   Scalar_Sigma_mono = Left_Side*Rzalpha'*SigmaPA_mono*...
                                    Rzalpha*Right_Side;
   v_mono = SF*(1 - Scalar_Sigma_mono);
   index = round((v_mono - Left_Spectrum)*inv_HzPt);
Spectrum_mono(index) = sin_vector(B) + Spectrum_mono(index);

   Scalar_Sigma_tri = Left_Side*Rzalpha'*SigmaPA_tri*...
                                   Rzalpha*Right_Side;
   v_tri = SF*(1-Scalar_Sigma_tri);
   index = round((v_tri - Left_Spectrum)*inv_HzPt);
Spectrum_tri(index) = sin_vector(B) + Spectrum_tri(index);
```

```
   Scalar_Sigma_Cp = Left_Side*Rzalpha'*SigmaPA_Cp*...
                                 Rzalpha*Right_Side;
   v_Cp = SF*(1 - Scalar_Sigma_Cp);
   index = round((v_Cp - Left_Spectrum)*inv_HzPt);
Spectrum_Cp(index) = sin_vector(B) + Spectrum_Cp(index);

end  % of A loop
end  % of B loop

Spectrum = 0.37*Spectrum_mono + 0.55*Spectrum_tri +...
           0.08*Spectrum_Cp;

FID = ifft(Spectrum);
Spectrum = real(fft(FID.*Damped_exp));
Spectrum = Spectrum - min(Spectrum);
Spectrum = (100/max(Spectrum))*Spectrum;
y_calc = a(1) + a(2)*Spectrum;
y_calc = y_calc(:);
```

Program 6.2b. Calculation of the Proton-Coupled ^{13}C Powder Pattern.

```
% Four Parameters to be fitted
% a(1) = Baseline Offset,
% a(2) = Scale Factor,
% a(3) = C-H bond length, and
% a(4) = H-C-H bond angle.

function [y_calc] =
        Dipole_ChemShift_functn(x_calc,a,deg,T2_L,SF,x)

% Structural parameters
r_1 = a(3)*1e-8;                                        % cm
r_2 = a(3)*1e-8;
r   = a(3)*1e-8*sin(a(4)/2*(pi/180))*2;
xH_1 = 0;
xH_2 = 0;
yH_1 = a(3)*1e-8*sin(a(4)/2*(pi/180));
yH_2 =-a(3)*1e-8*sin(a(4)/2*(pi/180));
zH_1 = a(3)*1e-8*cos(a(4)/2*(pi/180));
zH_2 = a(3)*1e-8*cos(a(4)/2*(pi/180));
R_H1 = [xH_1 yH_1 zH_1];
R_H2 = [xH_2 yH_2 zH_2];

% Fundamental parameters
gamma_H = 4257.5;
gamma_C = 1070.5;                                       % sec^-1 G^-1
h = 6.626176e-27;                                       % erg sec
CH2_const_1 =    gamma_C*gamma_H*h/r_1^3;
CH2_const_2 = 3*(gamma_C*gamma_H*h/r_1^5);
H2_const_1  =    gamma_H^2*h/r^3;
H2_const_2  = 3*(gamma_H^2*h/r^5);

% Instrument and calculation parameters
const_eps = 1 + eps*1e7;
alpha_spin = -1;
beta_spin = 1;
T2_L = 1/(pi*LB);
SF = 50310163;
FID_size = 512;
SW = x(length(x)) - x(1);
Dwell = 1/SW;
Time_axis = (0:FID_size-1)*Dwell;
Damped_exp = exp(-Time_axis/T2_L);
HzPt = (SW)/(FID_size-1);
inv_HzPt = 1/HzPt;
Left_Spectrum = SF + x(1);
Right_Spectrum = SF + x(length(x));
Freq_axis = Left_Spectrum - SF + HzPt*(0:FID_size - 1);
x_calc = Freq_axis;

% Initialize array for the calculated spectrum
Spect = zeros(1,FID_size);
Spect_mono = zeros(1,FID_size);
Spect_tri = zeros(1,FID_size);

% Principal elements of the 13C chemical shielding tensor
Sigma11_mono = 365.8e-6;
Sigma22_mono =  75.7e-6;
Sigma33_mono = -24.2e-6;
```

```
SigmaPA_mono = [Sigma11_mono 0 0;0 Sigma22_mono 0;...
                0 0 Sigma33_mono];
Sigma11_tri = Sigma11_mono + 6.6e-6;
Sigma22_tri = Sigma22_mono + 6.6e-6;
Sigma33_tri = Sigma33_mono + 6.6e-6;
SigmaPA_tri = [Sigma11_tri 0 0;0 Sigma22_tri 0;...
               0 0 Sigma33_tri];

% Spin angular momentum operators; I for 13C and S for 1H
S_xH1= 1/2*kron([0 1;  1 0], eye(4));
S_yH1= i/2*kron([0 -1; 1 0], eye(4));
S_zH1= 1/2*kron([1 0; 0 -1], eye(4));
S_xH2= 1/2*kron(eye(4), [0 1;  1 0]);
S_yH2= i/2*kron(eye(4), [0 -1; 1 0]);
S_zH2= 1/2*kron(eye(4), [1 0; 0 -1]);
I_xC = 1/2*kron(eye(2), kron([0 1;  1 0], eye(2)));
I_yC = i/2*kron(eye(2), kron([0 -1; 1 0], eye(2)));
I_zC = 1/2*kron(eye(2), kron([1 0; 0 -1], eye(2)));
I_pmC =    kron(kron(eye(2), [0 1; 1 0]), eye(2));

% Averaging over psi and theta using the y-convention
Range_Error = 0;
deg = 2;
angles = (deg:deg:360)*(pi/180);
sin_v = sin(angles);  cos_v = cos(angles);

for psi = 1:length(angles)/4
for theta = 1:length(angles)/4

A_11 =  cos_v(theta)*cos_v(psi);
A_21 =  sin_v(psi);
A_31 = -cos_v(psi)*sin_v(theta);
A_12 = -cos_v(theta)*sin_v(psi);
A_22 =  cos_v(psi);
A_32 =  sin_v(psi)*sin_v(theta);
A_13 =  sin_v(theta);
A_23 =  0;
A_33 =  cos_v(theta);
A = [A_11 A_12 A_13; A_21 A_22 A_23; A_31 A_32 A_33]';

% First, calc 13C Chemical Shielding & Zeeman and 1H Zeeman
  SigmaLAB_mono = A'*SigmaPA_mono*A;
  SigmaLAB_tri  = A'*SigmaPA_tri*A;
H_CS_mono = SF*(1 - SigmaLAB_mono(3,3))*I_zC;
H_CS_tri  = SF*(1 - SigmaLAB_tri(3,3))*I_zC;

H_Z = 200.044e6*(S_zH1 + const_eps*S_zH2);

% Second, calc CH2 and H2 dipolar interactions
    R_H1_lab = R_H1*A;
    R_H2_lab = R_H2*A;
      r1x = R_H1_lab(1);
      r1y = R_H1_lab(2);
      r1z = R_H1_lab(3);
      r2x = R_H2_lab(1);
      r2y = R_H2_lab(2);
      r2z = R_H2_lab(3);
  CH2_first_term = CH2_const_1*...
                   ((I_xC*S_xH1 + I_yC*S_yH1 + I_zC*S_zH1) +...
                    (I_xC*S_xH2 + I_yC*S_yH2 + I_zC*S_zH2));
  H2_first_term  =  H2_const_1*...
                   (S_xH1*S_xH2 + S_yH1*S_yH2 + S_zH1*S_zH2);
  CH2_second_term = CH2_const_2*...
```

```
                    ((I_xC*r1x + I_yC*r1y + I_zC*r1z)*...
                     (S_xH1*r1x + S_yH1*r1y + S_zH1*r1z)+...
                     (I_xC*r2x + I_yC*r2y + I_zC*r2z)*...
                      (S_xH2*r2x + S_yH2*r2y + S_zH2*r2z));
H_D_CH2 = CH2_first_term - CH2_second_term;
  H2_second_term = H2_const_2*...
           ((S_xH1*(r1x-r2x) + S_yH1*(r1y-r2y) + S_zH1*(r1z-r2z))*...
            (S_xH2*(r1x-r2x) + S_yH2*(r1y-r2y) + S_zH2*(r1z-r2z)));
H_D_H2 = H2_first_term - H2_second_term;

% Total Hamilitonian
H_total_mono = H_CS_mono + H_Z + H_D_CH2 + H_D_H2;
H_total_tri  = H_CS_tri  + H_Z + H_D_CH2 + H_D_H2;

% Calc. eigenenergies & transition frequencies for monoclinic form
[V,D] = eig(H_total_mono);
[lam,k] = sort(diag(D));
V=V(:,k);  Vadj = conj(V.');
x = diag(Vadj*S_zH1*V);
y = diag(Vadj*S_zH2*V);
z = diag(Vadj*I_zC*V);

  for test_diag = 1:8
    if x(test_diag)>0
      T_H1(test_diag)=beta_spin;
      else T_H1(test_diag)=alpha_spin;  end
    if y(test_diag)>0
      T_H2(test_diag)=beta_spin;
      else T_H2(test_diag)=alpha_spin;  end
    if z(test_diag)>0
      T_C(test_diag)=beta_spin;
      else T_C(test_diag)=alpha_spin;  end
  end

valid = zeros(2,6); k=1;
  for m=1:7                                    % starting spin state
    for n=m:8                                  % ending spin state
      if (T_H1(m) == T_H1(n))&(T_H2(m) == T_H2(n))&...
          (T_C(m) ~= T_C(n))
         valid(1,k)=m;  valid(2,k)=n;  k=k+1;
      end
      if (T_H1(m)~=T_H1(n))&(T_H2(m)~=T_H2(n))&...
         (T_C(m)~=T_C(n))&(T_H1(m)~=T_H2(m))&(T_H1(n)~=T_H2(n))
         valid(1,k)=m;  valid(2,k)=n;  k=k+1;
      end
    end
  end

total_trans = k - 1;
for k = 1:total_trans
  T(k) = abs(lam(valid(1,k)) - lam(valid(2,k)));
end

for j = 1:total_trans
  index = round((T(j) - Left_Spectrum)*inv_HzPt);
  if index>0 & index<=FID_size
    Spect_mono(index) = Weight + Spect_mono(index);
    else
    Range_Error = Range_Error + 1;
  end;
end
```

```
% Calc. eigenenergies & transition frequencies for triclinic form
[V,D] = eig(H_total_tri);
[lam,k] = sort(diag(D));
V=V(:,k);  Vadj = conj(V.');
x = diag(Vadj*S_zH1*V);
y = diag(Vadj*S_zH2*V);
z = diag(Vadj*I_zC*V);

  for test_diag = 1:8
    if x(test_diag)>0
      T_H1(test_diag)=beta_spin;
      else T_H1(test_diag)=alpha_spin;  end
    if y(test_diag)>0
      T_H2(test_diag)=beta_spin;
      else T_H2(test_diag)=alpha_spin;  end
    if z(test_diag)>0
      T_C(test_diag)=beta_spin;
      else T_C(test_diag)=alpha_spin;  end
  end

valid = zeros(2,6); k=1;
  for m=1:7                                    % starting spin state
    for n=m:8                                  % ending spin state
      if (T_H1(m) == T_H1(n))&(T_H2(m) == T_H2(n))&...
         (T_C(m) ~= T_C(n))
        valid(1,k)=m;  valid(2,k)=n;  k=k+1;
      end
      if (T_H1(m)~=T_H1(n))&(T_H2(m)~=T_H2(n))&...
         (T_C(m)~=T_C(n))&(T_H1(m)~=T_H2(m))&(T_H1(n)~=T_H2(n))
        valid(1,k)=m;  valid(2,k)=n;  k=k+1;
      end
    end
  end

total_trans = k - 1;
for k = 1:total_trans
  T(k) = abs(lam(valid(1,k)) - lam(valid(2,k)));
end

for j = 1:total_trans
  index = round((T(j) - Left_Spectrum)*inv_HzPt);
  if index>0 & index<=FID_size
    Spect_tri(index) = Weight + Spect_tri(index);
    else
    Range_Error = Range_Error + 1;
  end;
end

Spect = 0.4*Spect_mono + 0.6*Spect_tri;

end % of theta loop
end % of psi loop

FID = ifft(Spect);
Damped_FID = FID.*Damped_exp;
Spectrum = real(fft(FID.*Damped_exp));
Spectrum = Spectrum - min(Spectrum);
y_calc = (100/max(Spectrum))*Spectrum;
y_calc = a(1) + a(2)*Spectrum;
```

Program 6.2c. Calculation of the (^{14}N,^{195}Pt)-Coupled ^{13}C Powder Pattern.

```
% Five Parameters to be fitted
% a(1) = Baseline Offset,
% a(2) = Scale Factor,
% a(3) = Sigma_11,
% a(4) = Sigma_33, and
% a(5) = Frequency Offset in Hz.

function [y_calc] = ChemShift_PtCN_Functn (x_calc,a,deg,T2_L,SF,x)

% Structural parameters
r_CN  = 1.11e-8;                                        % cm
r_CPt = 2.02e-8;
xN = 0; yN = 0; zN = r_CN;
R_CN = [xN yN zN];
xPt = 0; yPt = 0; zPt = r_CPt;
R_CPt = [xPt yPt zPt];

% Fundamental parameters
gamma_C = 1070.5;                                       % sec^-1 G^-1
gamma_N = 307.5;
gamma_Pt = 915.32;
h = 6.626176e-27;                                       %erg sec
CN_const_1 =    gamma_C*gamma_N*h/r_CN^3;
CN_const_2 = 3*(gamma_C*gamma_N*h/r_CN^5);
CPt_const_1 =    gamma_C*gamma_Pt*h/r_CPt^3;
CPt_const_2 = 3*(gamma_C*gamma_Pt*h/r_CPt^5);

% Principal elements of the 13C chemical shielding tensor
Sigma11 = a(3)*1e-6;
Sigma33 = a(4)*1e-6;
Sigma22 = (127.9e-6*3 - Sigma11 - Sigma33);
SigmaPA = [Sigma11 0 0; 0 Sigma22 0; 0 0 Sigma33];

% 14N quadrupole coupling constant and asymmetry parameter
qcc = 3.467e6;
eta = 0.0;

% Instrumental and calculation parameters
alpha_spin = -1;
beta_spin = 1;
FID_size = 512;
SW = x(length(x)) - x(1);
Dwell = 1/SW;
Time_axis = (0:FID_size-1)*Dwell;
Damped_exp = exp(-Time_axis/T2_L);
HzPt = (SW)/(FID_size-1);
inv_HzPt = 1/HzPt;
%Left_Spectrum = SF - SW/2;
Left_Spectrum = SF + x(1);
Right_Spectrum = SF + x(length(x));
Freq_axis = Left_Spectrum - SF + HzPt*(0:FID_size - 1);

% Initialize array for spectrum
Spect = zeros(1,FID_size);


% Spin angular momentum operators; I for 13C and S for 14N and 195Pt
I_xC = 1/2*kron(eye(2), kron([0 1;  1 0], eye(3)));
```

```
I_yC = i/2*kron(eye(2), kron([0 -1; 1 0], eye(3)));
I_zC = 1/2*kron(eye(2), kron([1 0; 0 -1], eye(3)));
S_xPt = 1/2*kron([0 1;  1 0], eye(6));
S_yPt = i/2*kron([0 -1; 1 0], eye(6));
S_zPt = 1/2*kron([1 0; 0 -1], eye(6));
S_xN =   (sqrt(2)/2)*kron(eye(4), [0  1 0; 1  0  1; 0 1 0]);
S_yN = (i*sqrt(2)/2)*kron(eye(4), [0 -1 0; 1  0 -1; 0 1 0]);
S_zN =               kron(eye(4), [1  0 0; 0  0  0; 0 0 -1]);
S_sqrN =             kron(eye(4), [2 0 0; 0 2 0; 0 0 2]);
S_plusN =  sqrt(2)*kron(eye(4), [0 1 0; 0 0 1; 0 0 0]);
S_minusN = sqrt(2)*kron(eye(4), [0 0 0; 1 0 0; 0 1 0]);
S_x_sqrN = S_xN*S_xN;  S_y_sqrN = S_yN*S_yN;  S_z_sqrN = S_zN*S_zN;
S_plus_sqrN =  S_plusN*S_plusN;  S_minus_sqrN = S_minusN*S_minusN;
H_xx_op = 3*S_x_sqrN - S_sqrN;
H_yy_op = 3*S_y_sqrN - S_sqrN;
H_zz_op = 3*S_z_sqrN - S_sqrN;
H_xy_op = 1.5*(S_xN*S_yN + S_yN*S_xN);
H_xz_op = 1.5*(S_xN*S_zN + S_zN*S_xN);
H_yz_op = 1.5*(S_yN*S_zN + S_zN*S_yN);

% Averaging over psi and theta using y-convention
angles = 0:deg:90;
angles = angles*(2*pi/360);
sin_v = sin(angles);
cos_v = cos(angles);

for psi = 1:length(angles)
for theta = 1:length(angles)

Weight = sin_v(theta);
A_11 =  cos_v(theta)*cos_v(psi);
A_21 =  sin_v(psi);
A_31 = -cos_v(psi)*sin_v(theta);
A_12 = -cos_v(theta)*sin_v(psi);
A_22 =  cos_v(psi);
A_32 =  sin_v(psi)*sin_v(theta);
A_13 =  sin_v(theta);
A_23 =  0;
A_33 =  cos_v(theta);
A = [A_11 A_12 A_13; A_21 A_22 A_23; A_31 A_32 A_33]';

% First, calc 13C Chemical Shielding & Zeeman
  SigmaLAB = A'*SigmaPA*A;
H_CS = (SF + a(5)*HzPt)*(1 - SigmaLAB(3,3))*I_zC;

% Second, calc 14N Qadrupole
  q_efg = [qcc*(eta-1)/2 0 0; 0 -qcc*(eta+1)/2 0 ; 0 0 qcc];
  H_constant = 1/6;

  q_lab = A'*q_efg*A;
    H_xx = q_lab(1,1)*H_xx_op;
    H_yy = q_lab(2,2)*H_yy_op;
    H_zz = q_lab(3,3)*H_zz_op;
    H_xy = q_lab(1,2)*H_xy_op;  H_yx = H_xy';
    H_xz = q_lab(1,3)*H_xz_op;  H_zx = H_xz';
    H_yz = q_lab(2,3)*H_yz_op;  H_zy = H_yz';
H_NQ = H_constant*(H_xx + H_xy + H_xz + H_yx + H_yy + H_yz +...
                   H_zx + H_zy + H_zz);

% Third, calc 14N and 195Pt Zeeman
H_NZ  = 14.455e6*S_zN;
H_PtZ = 42.998e6*S_zPt;
```

```
% Fourth, calc 14N and 195Pt Dipole
     R_lab_CN = R_CN*A;
     rx_CN = R_lab_CN(1);
     ry_CN = R_lab_CN(2);
     rz_CN = R_lab_CN(3);
   CN_first_term = CN_const_1*...
                   (I_xC*S_xN + I_yC*S_yN + I_zC*S_zN);
   CN_second_term = CN_const_2*(I_xC*rx_CN + I_yC*ry_CN + ...
                    I_zC*rz_CN)*(S_xN*rx_CN + S_yN*ry_CN + S_zN*rz_CN);
H_ND = (CN_first_term - CN_second_term);

     R_lab_CPt = R_CPt*A;
     rx_CPt = R_lab_CPt(1);
     ry_CPt = R_lab_CPt(2);
     rz_CPt = R_lab_CPt(3);
   CPt_first_term = CPt_const_1*...
                    (I_xC*S_xPt + I_yC*S_yPt + I_zC*S_zPt);
   CPt_second_term = CPt_const_2*(I_xC*rx_CPt + I_yC*ry_CPt + ...
             I_zC*rz_CPt)*(S_xPt*rx_CPt + S_yPt*ry_CPt + S_zPt*rz_CPt);
H_PtD = (CPt_first_term - CPt_second_term);

% Fifth, calc 13C and 195Pt J-Coupling
H_J = 1034*(I_xC*S_xPt + I_yC*S_yPt + I_zC*S_zPt);

% Total Hamiltonian
H_total    = H_CS + H_NQ + H_NZ + H_ND + H_PtZ + H_PtD + H_J;

[V,D] = eig(H_total);
[lam,k] = sort(diag(D));
V=V(:,k);
Vadj = conj(V.');
x = diag(Vadj*S_zN*V);
y = diag(Vadj*S_zPt*V);
z = diag(Vadj*I_zC*V);

% Calc, six-transition frequencies
   for test_diag = 1:12
     if x(test_diag)>0
       T_N(test_diag)=beta_spin; else T_N(test_diag)=alpha_spin;
     end
     if abs(x(test_diag))<0.1
       T_N(test_diag)=0;
     end
     if y(test_diag)>0
       T_Pt(test_diag)=beta_spin; else T_Pt(test_diag)=alpha_spin;
     end
     if z(test_diag)>0
       T_C(test_diag)=beta_spin; else T_C(test_diag)=alpha_spin;
     end
   end

   valid = zeros(2,10);
   k=1;
   for m=1:11                                        %starting spin state
     for n=m:12                                      %ending spin state
     if (T_N(m) == T_N(n))&(T_Pt(m) == T_Pt(n))&(T_C(m) ~= T_C(n))
       valid(1,k)=m;  valid(2,k)=n;  k=k+1;
     end
     end
   end

total_trans = k - 1;
```

```
  for k=1:total_trans
    T(k) = abs(lam(valid(1,k)) - lam(valid(2,k)));
  end

for j=1:total_trans
  index = round((T(j) - Left_Spectrum)*inv_HzPt);
  Spect(index) = sin_v(theta) + Spect(index);
end

end % end theta loop
end % end psi loop

FID = ifft(Spect);
Spectrum = real(fft(FID.*Damped_exp));
Spectrum = Spectrum - min(Spectrum);
Spectrum = (100/max(Spectrum))*Spectrum;
y_calc = a(1) + a(2)*Spectrum;
```

Program 6.2d. Calculation of the Deuterium Powder Pattern.

```
% Five Parameters to be fitted
% a(1) = Baseline Offset,
% a(2) = Scale Factor,
% a(3) = Quadrupole Coupling Constant ,
% a(4) = Asymmetry Parameter , and
% a(5) = Frequency Offset in Hz.

function[y_calc] = Deu_Functn(x_calc,a,deg,LB,wL,SW)

% 2H quadrupole coupling constant and asymmetry parameter
qcc = a(3);
eta = a(4);

% Spin angular monentum operators
I_x =    (sqrt(2)/2)*[0  1 0; 1  0  1; 0 1  0];
I_y = (i*sqrt(2)/2)*[0 -1 0; 1  0 -1; 0 1  0];
I_z =                [1  0 0; 0  0  0; 0 0 -1];
I_x_sqr = I_x*I_x;
I_y_sqr = I_y*I_y;
I_z_sqr = I_z*I_z;
I_sqr = [2 0 0; 0 2 0; 0 0 2];
I_plus = sqrt(2)*[0 1 0; 0 0 1; 0 0 0];
I_minus = sqrt(2)*[0 0 0; 1 0 0; 0 1 0];
I_plus_sqr = I_plus*I_plus;
I_minus_sqr = I_minus*I_minus;

H_xx_op = 3*I_x_sqr - I_sqr;
H_yy_op = 3*I_y_sqr - I_sqr;
H_zz_op = 3*I_z_sqr - I_sqr;
H_xy_op = 3/2*(I_x*I_y + I_y*I_x);
H_xz_op = 3/2*(I_x*I_z + I_z*I_x);
H_yz_op = 3/2*(I_y*I_z + I_z*I_y);

% Start Defining 2H Zeeman & Quadrupolar Hamiltonians
   q_efg = [qcc*(eta-1)/2 0 0; 0 -qcc*(eta+1)/2 0 ; 0 0 qcc];
   H_constant = 1/6;
H_zeeman = -(wL + a(5)*HzPt)*I_z;

% Averaging over psi = 0 to 90 and theta = 0 to 90 deg
for psi = 1:length(sin_v)
for theta = 1:length(sin_v)

   A_11 =  cos_v(theta)*cos_v(psi);
   A_21 =  sin_v(psi);
   A_31 = -cos_v(psi)*sin_v(theta);
   A_12 = -cos_v(theta)*sin_v(psi);
   A_22 =  cos_v(psi);
   A_32 =  sin_v(psi)*sin_v(theta);
   A_13 =  sin_v(theta);
   A_23 =  0;
   A_33 =  cos_v(theta);
   A = [A_11 A_12 A_13; A_21 A_22 A_23; A_31 A_32 A_33]';

   q_lab = A'*q_efg*A;
      H_xx = q_lab(1,1)*H_xx_op;
      H_yy = q_lab(2,2)*H_yy_op;
      H_zz = q_lab(3,3)*H_zz_op;
      H_xy = q_lab(1,2)*H_xy_op;  H_yx = H_xy';
```

```
      H_xz = q_lab(1,3)*H_xz_op;  H_zx = H_xz';
      H_yz = q_lab(2,3)*H_yz_op;  H_zy = H_yz';
   H_quad = H_constant*(H_xx + H_xy + H_xz + H_yx + H_yy +...
                        H_yz +.H_zx + H_zy + H_zz);

H_total = H_zeeman + H_quad;

[U,E] = eig(H_total);
[E,k] = sort(real(diag(E)));
trans_1 = E(3) - E(2) - Left_Spectrum;
trans_2 = E(2) - E(1) - Left_Spectrum;
index_1 = round(trans_1/HzPt);
index_2 = round(trans_2/HzPt);

Spect(index_1) = sin_vector(B) + Spect(index_1);
Spect(index_2) = sin_vector(B) + Spect(index_2);

end   % of theta loop
end   % of psi loop

FID = ifft(Spect);
Damped_FID = FID.*Damped_exp;
Spectrum = real((fft(Damped_FID)));
Spectrum = real(Spectrum - min(Spectrum));
Spectrum = (100/max(Spectrum))*Spectrum;
y_calc = a(1) + a(2)*Spectrum;
y_calc = y_calc(:);
```

Program 6.3. Calculation of the Derivatives of the Fitting Function.

```
function[dyda] = CurFit_nonanal(a,delta_a,deg,T2_L,SF,x)

dyda = zeros(length(x),length(a));
y_plus_delta = zeros(length(x),1);
y_minus_delta = zeros(length(x),1);
a_temp = zeros(1,length(a));

for J = 1:length(a)
   a_temp = a;
   a_temp(J) = a(J) + delta_a(J);

% Optional for deuterium powder pattern fitting
      if a_temp(4)<0  a_temp(4)=0;
         else a_temp(4) = a_temp(4);
      end
      if a_temp(4)>1   a_temp(4)=1;
         else a_temp(4) = a_temp(4);
      end

   [y_plus_delta] = Fitting function ;
   a_temp(J) = a(J) - delta_a(J);

% Optional for deuterium powder pattern fitting
      if a_temp(4)<0  a_temp(4)=0;
         else a_temp(4) = a_temp(4);
      end
      if a_temp(4)>1   a_temp(4)=1;
         else a_temp(4) = a_temp(4);
      end

   [y_minus_delta] = Fitting function ;

dyda(:,J) = ((y_plus_delta - y_minus_delta)/(2*delta_a(J)));

end;
```

Program 6.4. Calculation of the value of χ^2 for the Fitting Function.

```
function[chi_sqr] = CurFit_chisqr(y_exp,y_calc,inv_sigma_sqr)
chi_sqr = (sum(inv_sigma_sqr.*(y_exp - y_calc).^2));
```

References for Chapter 6

(95) See section 3.4.

(96) See sections 2.4 and 4.4.

(97) Altbach, M. I.; Hiyama, Y.; Wittebort, R. J.; Butler, L. G. *Inorg. Chem.* **1990**, *29*, 741-7.

(98) (a) Teng, Q.; Cross, T. A. *J. Magn. Reson.*, **1989**, *85*, 439-47.
(b) Oas, T. G.; Drobny, G. P.; Dahlquist, F. W. *J. Magn. Reson.* **1988**, *78*, 408-24.
(c) Hyde, J. S.; Pasenkiewicz-Gierula, M.; Basosi, R.; Froncisz, W.; Antholine, W. E. *J. Magn. Reson.* **1989**, *82*, 63-75.

(99) (a) Bevington, P. R. *Data Reduction and Error Analysis for the Physical Sciences*; McGraw-Hill: New York, 1969.
(b) Press, W. H.; Flannery, B. P.; Teukolsky, S. A.; Vetterling, W. T. *Numerical Recipes*; Cambridge University Press: Cambridge, 1986.

(100) (a) Alderman, D. W.; Solum, M. S.; Grant, D. M. *J. Chem. Phys.* **1986**, *84*, 3717-25.
(b) Conroy, H. *J. Chem. Phys.* **1967**, *47*, 5307-18.
(c) Cheng, V. B.; Suzukawa, Jr., H. H.; Wolfsberg, M. *J. Chem. Phys.* **1973**, *59*, 3992-9.

(101) (a) Bloom, M.; Davis, J. H.; Valic, M. I. *Can. J. Phys.* **1980**, *58*, 1510-7.
(b) Henrichs, P. M.; Hewitt, J. M.; Linder, M. *J. Magn. Reson.* **1984**, *60*, 280-98.

(102) (a) VanderHart, D. L. *J. Chem. Phys.* **1976**, *64*, 830-4.
(b) Levitt, M. H.; Suter, D.; Ernst, R. R. *J. Chem. Phys.* **1986**, *84*, 4243-55.

CHAPTER 7

Conclusions and Recommendations for Future Work

Various solid-state NMR techniques have been used in this research to study the nature of chemical bonding in organometallic complexes including metal-hydrogen, metal-carbon, and metal-phosphorus bonds. Experiments were done with a Bruker MSL200 solid-state spectrometer. This research has been concentrated on the interpretation of NMR parameters as well as procedures for extracting the parameters from solid-state NMR powder patterns.

The studies of M-$^{13}CH_2$-M and M-^{13}CN units provide a simple system for the analysis of the paramagnetic contribution to the chemical shielding tensor as well as obtaining structural information based on the dipolar coupling tensor. The principal elements and the complete orientation of the chemical shielding tensor provide three-dimensional information on electronic structure, which is a fundamental probe of the nature of the chemical bonding at a specific site. For the study of a bridging methylene unit, molecular orbital analysis shows that the very large paramagnetic chemical shielding tensor element is a result of relatively weak C–M bonds through two carbon atomic p orbitals and strong C–H bonds with the remaining carbon p orbital. The dipolar coupling interaction allows not only the assignment of the chemical shielding tensor orientation, but also the determination of local molecular geometry. In the case of metal cyanide complexes, the paramagnetic contribution is correlated with an increase in π back–bonding in the order Ni < Pd < Pt.

The study of bridging metal hydride complexes shows that deuterium quadrupole coupling constants and asymmetry parameters are related to the M–H–M bond distance and the M–H–M bond angle with a point charge model and by assuming that the sign of the quadrupole coupling constant is positive. In addition, high resolution deuterium MAS NMR spectra are important for the study of systems having multiple deuterium sites. From the application of deuterium MAS NMR to simple inorganic compounds, we found that the ability for resolving each deuterium site

depends on the spin rate and the difference between the quadrupole coupling constants of two distinct sites.

The formation of M–C, M–H, or M–P bonds is important in reactions of discrete organometallic complexes and also for reactions occurring on catalytic surfaces. Thus, an extension of this work is the qualitative prediction of the NMR parameters for surface-bound species. Although the detection of bridging methylene units on surfaces has been particularly difficult for traditional surface science technique, it is possible to qualitatively predict some aspects of the NMR chemical shielding tensor for a surface bound species. In addition, an extension to μ_3–bridging hydrides on surfaces is possible by using a model developed herein describing the effect of M–H distance and M–H–M bond angle on the deuterium quadrupole coupling constant and the asymmetry parameter.

APPENDICES

Appendix A. Program for Calculating the 2D Separated Local Field Spectrum.

```
clc; clear; clg; echo off; flops(0); fix(clock)

% Now uses Hamiltonians for chemical shielding and C-H dipolar
% coupling
% Dimension 1 is DIPOLAR COUPLING
% DImension 2 is CHEMICAL SHIELDING

% Structural parameters
r_1 = 1.122e-8;                                          % cm
r_2 = 1.122e-8;
r   = 1.122e-8*sin(110.8/2*(pi/180))*2;
xH_1 = 0;
xH_2 = 0;
yH_1 = 1.122e-8*sin(110.8/2*(pi/180));
yH_2 =-1.122e-8*sin(110.8/2*(pi/180));
zH_1 = 1.122e-8*cos(110.8/2*(pi/180));
zH_2 = 1.122e-8*cos(110.8/2*(pi/180));
R_H1 = [xH_1 yH_1 zH_1];
R_H2 = [xH_2 yH_2 zH_2];

% Fundamental parameters
gamma_H = 4257.5;                                        % sec^-1 G^-1
gamma_C = 1070.5;
h = 6.626176e-27;                                        % erg sec
CH2_const_1 =    gamma_C*gamma_H*h/r_1^3;
CH2_const_2 = 3*(gamma_C*gamma_H*h/r_1^5);

% Instrument and calculation constants
const_eps = 1 + eps*1e7;
alpha_spin = -1;
beta_spin = 1;
SF = 50.301e6 + 9250;
FID_size_1 = 64;
FID_size_2 = 64;
SW_1 = 185185;
SW_2 = 62500;
HzPt_1 = SW_1/FID_size_1;
HzPt_2 = SW_2/FID_size_2;
Dwell_1 = 1/SW_1;
Dwell_2 = 1/SW_2;
  j = 1:FID_size_1;
    Freq_axis_1 = -SW_1/2 + HzPt_1*(j-1);
    Time_axis_1 = (j-1)*Dwell_1;
    Damp_1 = exp(-(Time_axis_1*1000).^2);
  j = 1:FID_size_2;
    Freq_axis_2 = -SW_2/2 + HzPt_2*(j-1);
    Freq_axis_2_ppm = Freq_axis_2/v1*1e6;
    Time_axis_2 = (j-1)*Dwell_2;
    Damp_2 = exp(-(Time_axis_2*5000).^2);

% Initialize array for the calculated spectra
Spect_mono = zeros(FID_size_1,FID_size_2);
Spect_tri = zeros(FID_size_1,FID_size_2);
Spect_Cp = zeros(FID_size_1,FID_size_2);
Spect_F1 = zeros(1,FID_size_1);
Spect_F2 = zeros(1,FID_size_2);
Spect = zeros(FID_size_1,FID_size_2);
```

```
% Principal elements of the 13C chemical shielding tensor
Sigma11_mono = 378.9e-6;
Sigma22_mono =  67.5e-6;
Sigma33_mono = -29.4e-6;
Sigma11_tri = 385.4e-6;
Sigma22_tri =  74.1e-6;
Sigma33_tri = -22.8e-6;
Sigma11_Cp = 122e-6;
Sigma22_Cp = 122e-6;
Sigma33_Cp =  22e-6;

SigmaPA_mono = [Sigma11_mono 0 0; 0 Sigma22_mono 0;...
                0 0 Sigma33_mono];
SigmaPA_tri  = [Sigma11_tri 0 0; 0 Sigma22_tri 0;...
                0 0 Sigma33_tri];
SigmaPA_Cp = [Sigma11_Cp 0 0; 0 Sigma22_Cp 0; 0 0 Sigma33_Cp];

%Spin angular momentum operators
S_xH1= 1/2*kron([0 1;  1 0], eye(4));
S_yH1= i/2*kron([0 -1; 1 0], eye(4));
S_zH1= 1/2*kron([1 0; 0 -1], eye(4));
S_xH2= 1/2*kron(eye(4), [0 1;  1 0]);
S_yH2= i/2*kron(eye(4), [0 -1; 1 0]);
S_zH2= 1/2*kron(eye(4), [1 0; 0 -1]);
I_xC = 1/2*kron(eye(2), kron([0 1;  1 0], eye(2)));
I_yC = i/2*kron(eye(2), kron([0 -1; 1 0], eye(2)));
I_zC = 1/2*kron(eye(2), kron([1 0; 0 -1], eye(2)));
I_pmC =    kron(kron(eye(2), [0 1; 1 0]), eye(2));

% Averaging over psi and theta using y-convention
Range_Error = 0;
deg = 5;
angles = (deg:deg:360)*(pi/180);
sin_v = sin(angles);
cos_v = cos(angles);

for psi = 1:length(angles)/4
for theta = 1:length(angles)/4

Weight = sin_v(theta);
A_11 =  cos_v(theta)*cos_v(psi);
A_21 =  sin_v(psi);
A_31 = -cos_v(psi)*sin_v(theta);
A_12 = -cos_v(theta)*sin_v(psi);
A_22 =  cos_v(psi);
A_32 =  sin_v(psi)*sin_v(theta);
A_13 =  sin_v(theta);
A_23 =  0;
A_33 =  cos_v(theta);
A = [A_11 A_12 A_13; A_21 A_22 A_23; A_31 A_32 A_33]';

% First, calc 13C chemical shielding & Zeeman and 1H Zeeman
  SigmaLAB_mono = A'*SigmaPA_mono*A;
  SigmaLAB_tri = A'*SigmaPA_tri*A;
  SigmaLAB_Cp = A'*SigmaPA_Cp*A;
H_CS_mono = SF*(1 - SigmaLAB_mono(3,3))*I_zC;
H_CS_tri  = SF*(1 - SigmaLAB_tri(3,3))*I_zC;
H_CS_Cp   = SF*(1 - SigmaLAB_Cp(3,3))*I_zC;
H_Z = 200.044e6*(S_zH1 + const_eps*S_zH2);

% Second, calc CH2 and H2 dipolar interactions
  R_H1_lab = R_H1*A;
  R_H2_lab = R_H2*A;
```

```
  r1x = R_H1_lab(1); r1y = R_H1_lab(2); r1z = R_H1_lab(3);
  r2x = R_H2_lab(1); r2y = R_H2_lab(2); r2z = R_H2_lab(3);

  CH2_first_term = CH2_const_1*...
             ((I_xC*S_xH1 + I_yC*S_yH1 + I_zC*S_zH1) +...
              (I_xC*S_xH2 + I_yC*S_yH2 + I_zC*S_zH2));
  CH2_second_term = CH2_const_2*...
             ((I_xC*r1x + I_yC*r1y + I_zC*r1z)*...
              (S_xH1*r1x + S_yH1*r1y + S_zH1*r1z)+...
              (I_xC*r2x + I_yC*r2y + I_zC*r2z)*...
              (S_xH2*r2x + S_yH2*r2y + S_zH2*r2z));
H_D_CH2 = CH2_first_term - CH2_second_term;

H_total_mono = H_CS_mono + H_Z + (H_D_CH2)/sqrt(3);
H_total_tri  = H_CS_tri +  H_Z + (H_D_CH2)/sqrt(3);
H_total_Cp =   H_CS_Cp +   H_Z + (H_D_CH2)/sqrt(3);

% Calc. eigenenergies and transition frequiencies for
  monoclinic form
[V,D] = eig(H_total_cis1);
[lam,k] = sort(diag(D));
V=V(:,k);  Vadj = conj(V.');
x = diag(Vadj*S_zH1*V);
y = diag(Vadj*S_zH2*V);
z = diag(Vadj*I_zC*V);

  for test_diag = 1:8
    if x(test_diag)>0
      T_H1(test_diag)=beta_spin;
      else T_H1(test_diag)=alpha_spin; end
    if y(test_diag)>0
      T_H2(test_diag)=beta_spin;
      else T_H2(test_diag)=alpha_spin; end
    if z(test_diag)>0
      T_C(test_diag)=beta_spin;
      else T_C(test_diag)=alpha_spin; end
  end

valid = zeros(2,6); k=1;
  for m=1:7                                  % starting spin state
    for n=m:8                                % ending spin state
      if (T_H1(m)==T_H1(n))&(T_H2(m)==T_H2(n))&...
         (T_C(m)~=T_C(n))
      valid(1,k)=m;  valid(2,k)=n;  k=k+1;
      end
      if (T_H1(m)~=T_H1(n))&(T_H2(m)~=T_H2(n))&...
         (T_C(m)~=T_C(n))&(T_H1(m)~=T_H2(m))&...
        (T_H1(n)~=T_H2(n))
      valid(1,k)=m;  valid(2,k)=n;  k=k+1;
      end
    end
  end

T_ChemShift_mono = SF*(1 - SigmaLAB_mono(3,3));
index_CS_mono = round((T_ChemShift_mono - SF + SW_2/2)/HzPt_2);

total_trans = k - 1;
for k=1:total_trans
  T(k) = abs(lam(valid(1,k)) - lam(valid(2,k)));
end

for k=1:total_trans
  T_Dipolar_mono(k) = abs(lam(valid(1,k)) - lam(valid(2,k)));
```

```
  index_Dipolar_mono =...
           round((T_Dipolar_mono(k) - SF +SW_1/2)/HzPt_1);
  Spect_mono(index_Dipolar_mono,index_CS_mono) =
        Weight + Spect_mono(index_Dipolar_mono,index_CS_mono);
end

% Calc. eigenenergies and transition frequiencies for
  triclinic form
[V,D] = eig(H_total_tri);
[lam,k] = sort(diag(D));
V=V(:,k);  Vadj = conj(V.');
x = diag(Vadj*S_zH1*V);
y = diag(Vadj*S_zH2*V);
z = diag(Vadj*I_zC*V);

  for test_diag = 1:8
    if x(test_diag)>0
      T_H1(test_diag)=beta_spin;
      else T_H1(test_diag)=alpha_spin; end
    if y(test_diag)>0
      T_H2(test_diag)=beta_spin;
      else T_H2(test_diag)=alpha_spin; end
    if z(test_diag)>0
      T_C(test_diag)=beta_spin;
      else T_C(test_diag)=alpha_spin; end
  end

valid = zeros(2,6); k=1;
  for m=1:7                                  % starting spin state
    for n=m:8                                % ending spin state
      if (T_H1(m) == T_H1(n))&(T_H2(m) == T_H2(n))&...
         (T_C(m) ~= T_C(n))
      valid(1,k)=m;  valid(2,k)=n;  k=k+1;
      end
      if (T_H1(m)~=T_H1(n))&(T_H2(m)~=T_H2(n))&...
         (T_C(m)~=T_C(n))&(T_H1(m)~=T_H2(m))&...
         (T_H1(n)~=T_H2(n))
      valid(1,k)=m;  valid(2,k)=n;  k=k+1;
      end
    end
  end

T_ChemShift_tri = SF*(1 - SigmaLAB_tri(3,3));
index_CS_tri = round((T_ChemShift_tri - SF + SW_2/2)/HzPt_2);

total_trans = k - 1;
for k=1:total_trans
  T_Dipolar_tri(k) = abs(lam(valid(1,k)) - lam(valid(2,k)));
  index_Dipolar_tri = round((T_Dipolar_tri(k) - SF +...
                        SW_1/2)/HzPt_1);
  Spect_cis2(index_Dipolar_tri,index_CS_tri) = Weight +...
                Spect_tri(index_Dipolar_tri,index_CS_tri);
end

% Calc. eigenenergies and transition frequencies for Cp ring
[V,D] = eig(H_total_Cp);
[lam,k] = sort(diag(D));
V=V(:,k);  Vadj = conj(V.');
x = diag(Vadj*S_zH1*V);
y = diag(Vadj*S_zH2*V);
z = diag(Vadj*I_zC*V);

  for test_diag = 1:8
    if x(test_diag)>0
```

```
      T_H1(test_diag)=beta_spin;
      else T_H1(test_diag)=alpha_spin; end
    if y(test_diag)>0
      T_H2(test_diag)=beta_spin;
      else T_H2(test_diag)=alpha_spin; end
    if z(test_diag)>0
      T_C(test_diag)=beta_spin;
      else T_C(test_diag)=alpha_spin; end
  end

valid = zeros(2,6); k=1;
  for m=1:7                                    % starting spin state
    for n=m:8                                  % ending spin state
      if (T_H1(m) == T_H1(n))&(T_H2(m) == T_H2(n))&...
         (T_C(m) ~= T_C(n))
      valid(1,k)=m;  valid(2,k)=n;  k=k+1;
      end
      if (T_H1(m)~=T_H1(n))&(T_H2(m)~=T_H2(n))&...
         (T_C(m)~=T_C(n))&(T_H1(m)~=T_H2(m))&...
         (T_H1(n)~=T_H2(n))
      valid(1,k)=m;  valid(2,k)=n;  k=k+1;
      end
    end
  end

T_ChemShift_Cp = SF*(1 - SigmaLAB_Cp(3,3));
index_CS_Cp = round((T_ChemShift_Cp - SF + SW_2/2)/HzPt_2);

total_trans = k - 1;
for k=1:total_trans
  T_Dipolar_Cp(k) = abs(lam(valid(1,k)) - lam(valid(2,k)));
  index_Dipolar_Cp = round((T_Dipolar_Cp(k) - SF +...
                            SW_1/2)/HzPt_1);
  Spect_Cp(index_Dipolar_Cp,index_CS_Cp) = Weight +...
                    Spect_Cp(index_Dipolar_Cp,index_CS_Cp);
end

end    % of theta loop
end    % of psi loop

Spect = 0.37*Spect_mono + 0.55*Spect_tri + 0.08*Spect_Cp;
Spect = Spect(FID_size_1:-1:1,:);
FID_2D = ifft2(Spect);
  for j = 1: FID_size_2
    Damped_FID_2D(j,:) = FID_2D(j,:).*Damp_2;
  end
  for k = 1: FID_size_1
    Damped_FID_2D(:,k) = Damped_FID_2D(:,k).*Damp_1';
  end

Spectrum = fft2(Damped_FID_2D);
mesh(Spectrum);
flops
fix(clock)
```

Appendix B. Program for Calculating the MAS Sideband Intensities.

```
clc; clear; echo on; flops(0); fix(clock)

% Trapezoidal Rule was used to approximate the integrals
% l;interval, k;superscript, and h;width of each subdivision
l_beta = pi;
k_beta = 6;
h_beta = l_beta/(2^k_beta);

vR = [5000];
ssb = [-25:25];

% Initialize arrays for the calculated spinning sidebands
IN = zeros(length(ssb),length(vR));
IN_D = zeros(length(ssb),length(vR));

for k = 1:length(vR)
  wR = 2*pi*vR(k);

for j = 1:length(ssb)
  N = ssb(j);

sum_beta = 0;
for l = 1:(2^k_beta-1)
  beta = l*h_beta;
  sum_alpha = f_alpha[beta,wR,N];
  C = sum_alpha*sin(beta);
    if l==0 | l==2^k_beta
      CI_beta = (h_beta/2)*C;
    else
      CI_beta = (h_beta/2)*2*C;
    end
  sum_beta = sum_beta + CI_beta;
end    % of l loop

IN(j,k) = 1/(4*pi)*sum_beta;

end % of k loop
end % of j loop

% Symmetrization of the spinning sidebands for deuterium MAS
for m = 1:length(vR)
  for n = 1:length(ssb)
    IN_D(n,m) = (IN(n,m) + IN((length(ssb)+1-n),m))/2;
  end
end

flops; fix(clock)
```

Subroutine f_alpha function.

```
function sum_alpha = f_alpha[beta,wR,N];

l_alpha = 2*pi;
k_alpha = 6;
h_alpha = l_alpha/(2^k_alpha);

sum_alpha = 0;
for m = 0:(2^k_alpha)
  alpha = m*h_alpha;
  B = f_theta[alpha,beta,wR,N];
    if m==0 | m==2^k_alpha
      BI_alpha = (h_alpha/2)*B;
     else
      BI_alpha = (h_alpha/2)*2*B;
    end
  sum_alpha = sum_alpha + BI_alpha;

end
```

Subroutine f_theta function.

```
function B = f_theta[alpha,beta,wR,N]

% Quadrupole coupling constant and asymmetry parameter for
% Deuterium MAS
QCC = 162e3;
wQ = 3/2*pi*QCC;
eta = 0.171;

% Chemical shielding tensor for 13C MAS
wL = 50.301e6 + 9163;
sigma_zz = 365.7e-6; sigma_yy = 75.5e-6; sigma_xx = -24.2e-6;
sigma_bar = (sigma_xx + sigma_yy + sigma_zz)/3;

l_theta = 2*pi;
k_theta = 6;
h_theta = l_theta/(2^k_theta);

sum_theta = 0;
for n = 0:(2^k_theta)
  theta = n*h_theta;

% For deuterium MAS
  delta_m = eta*(-wQ/wR);
  delta_p = 3*(-wQ/wR);

% For 13C MAS
  delta_m = (-wL/wR)*(sigma_xx - sigma_yy);
  delta_p = (-wL/wR)*3*(sigma_bar - sigma_zz);

    tau_m_s1 = (1/24)*cos(2*alpha)*...
                    (3+cos(2*beta))*sin(2*theta);
    tau_m_s2 = (1/6)*sin(2*alpha)*cos(beta)*cos(2*theta);
    tau_m_s3 = (sqrt(2)/6)*cos(2*alpha)*...
                    sin(2*beta)*sin(theta);
    tau_m_s4 = (sqrt(2)/3)*sin(2*alpha)*sin(beta)*cos(theta);
  tau_m = tau_m_s1 - tau_m_s2 + tau_m_s3 - tau_m_s4;
    tau_p_s1 = (cos(2*beta)-1)*sin(2*theta)/24;
    tau_p_s2 = (sqrt(2)/6)*sin(2*beta)*sin(theta);
  tau_p = tau_p_s1 + tau_p_s2;

  A = exp(i*(-N*theta + delta_m*tau_m + delta_p*tau_p));
    if n==0 | n==2^k_theta
      AI_theta = (h_theta/2)*A;
    else
      AI_theta = (h_theta/2)*2*A;
    end
  sum_theta = sum_theta + AI_theta;

end

F = 1/(2*pi)*sum_theta;
B = abs(F)^2;
```

Appendix C. Symmetrized Spinning Sideband Integrals Obtained from the Experimental Deuterium MAS NMR Spectra.

N	K^2HCO_3	$^2HIO_3$	Na^2HCO_3	K^2HSO_4	K^2HCO_3 + $^2HIO_3$	K^2HCO_3 + Na^2HCO_3
0	0.0265	0.0216	0.0273	0.0204	0.0241	0.0282
1	0.0248	0.0208	0.0270	0.0245	0.0224	0.0260
2	0.0265	0.0212	0.0290	0.0247	0.0239	0.0277
3	0.0269	0.0199	0.0307	0.0251	0.0234	0.0260
4	0.0249	0.0225	0.0285	0.0277	0.0236	0.0276
5	0.0261	0.0221	0.0264	0.0262	0.0232	0.0265
6	0.0319	0.0233	0.0316	0.0236	0.0287	0.0295
7	0.0332	0.0206	0.0366	0.0249	0.0273	0.0309
8	0.0389	0.0232	0.0404	0.0331	0.0311	0.0393
9	0.0460	0.0273	0.0476	0.0398	0.0367	0.0472
10	0.0433	0.0356	0.0446	0.0407	0.0387	0.0451
11	0.0370	0.0416	0.0330	0.0356	0.0382	0.0372
12	0.0287	0.0434	0.0234	0.0309	0.0351	0.0249
13	0.0208	0.0414	0.0187	0.0229	0.0317	0.0196
14	0.0142	0.0286	0.0133	0.0214	0.0225	0.0140
15	0.0078	0.0159	0.0078	0.0148	0.0132	0.0101
16	0.0070	0.0114	0.0086	0.0121	0.0097	0.0077
17	0.0074	0.0099	0.0100	0.0090	0.0085	0.0066
18	0.0083	0.0070	0.0089	0.0098	0.0082	0.0087
19	0.0096	0.0052	0.0075	0.0081	0.0077	0.0081
20	0.0084	0.0053	0.0060	0.0075	0.0062	0.0090
21	0.0060	0.0055	0.0050	0.0078	0.0049	0.0067
22	0.0037	0.0064	0.0019	0.0071	0.0052	0.0051
23	0.0027	0.0068	0	0.0054	0.0046	0.0025
24	0.0016	0.0068	0	0.0042	0.0043	0
25	0.0009	0.0058	0	0.0030	0.0035	0
26		0.0051			0.0024	
27		0.0032			0.0017	
28		0.0019			0.0008	
29		0.0010			0.0007	
30		0.0005			0	

Appendix D.

Copyright Letters for Chapters 2 and 3.

LOUISIANA STATE UNIVERSITY
AND AGRICULTURAL AND MECHANICAL COLLEGE
Department of Chemistry

September 3, 1991

Copyright Administrator
Books and Journals Division
American Chemical Society
1155 16th Street, N. W.
Washington, DC 20036

Dear Sir:

Please grant me permission to use the manuscript of "The ^{13}C NMR Chemical Shielding Tensor of the Bridging Methylene Unit in *cis*-(μ-CH_2)(μ-CO)[FeCp(CO)]$_2$" published in the Journal of the American Chemical Society, **1991**, *113*, 4831-4838, in my Ph.D. dissertation. I am the first author on this manuscript.

Sincerely,

Ae Ja Kim

Ae Ja Kim
Box E-21, Choppin Hall
Department of Chemistry
Louisiana State University
Baton Rouge, LA 70803

LOUISIANA STATE UNIVERSITY
AND AGRICULTURAL AND MECHANICAL COLLEGE
Department of Chemistry

September 3, 1991

Copyright Administrator
Books and Journals Division
American Chemical Society
1155 16th Street, N. W.
Washington, DC 20036

Dear Sir:

Please grant me permission to use the manuscript of "Deuterium Quadrupole Coupling Constants and Asymmetry Parameters in Bridging Metal Hydride Complexes" which is in press (JA910922P–50–6–85) in the Journal of the American Chemical Society in my Ph.D. dissertation. I am the first author on this manuscript.

Sincerely,

Ae Ja Kim

Ae Ja Kim
Box E–21, Choppin Hall
Department of Chemistry
Louisiana State University
Baton Rouge, LA 70803

PUBLICATIONS DIVISION

1155 SIXTEENTH STREET, N.W.
WASHINGTON, D.C. 20036
Phone (202) 872-4600
Fax (202) 872-6060

DATE: September 9, 1991

MEMORANDUM

TO: Ae Ja Kim
Box E-21, Choppin Hall
Department of Chemistry
Louisiana State University
Baton Rouge, LA 70803

FROM: C. Arleen Courtney
Copyright Assistant C. Arleen Courtney

RE: Your letter dated September 3, 1991

Your paper,s from J. Am. Chem. Soc. 1991, 113, 4831-4838 and
Kim, A. J. J. Am. Chem. Soc., in press

Thank you for your recent letter, regarding your request for permission to include your paper, as cited above, in your thesis. Please note the following:

☑ If your paper has already been published by ACS, I would be happy to grant you this permission royalty free provided that you print the required ACS copyright credit line on the first page of your article: "Reprinted with permission from FULL REFERENCE CITATION. Copyright YEAR American Chemical Society."

If you plan to submit your thesis to UMI, please inform them that permission to include your published ACS article as part of your thesis is granted for paper and micorform copies only; the ACS copyright notice (see above) must appear on the first page of the ACS article.

☑ If you paper has not already been published by ACS, you may include it in your thesis provided that you print the following ACS copyright credit line on the first page of your article: "Reprinted with permission from JOURNAL NAME, in press. Unpublished work copyright CURRENT YEAR American Chemical Society." You may NOT include the ACS paper in the version that you submit to UMI until ACS has published your paper.

☐ Other: _____

Thank you for writing. If you have any questions, please call me at (202) 872-4368.

Vita

Ae Ja Kim (Woo) was born in Seoul, Korea on December 9, 1958. She received a B.S. degree in 1981 and a M.S. degree in 1986 in chemistry from Ewha Womans University in Seoul, Korea. She married Weon Ho Kim in November of 1984 and came to the United States of America in August of 1986. In January of 1987, she entered Louisiana State University as a candidate for the degree of Doctor of Philosophy, where she worked in the area of "Solid-State NMR Studies of Organometallic Complexes" under the direction of Professor Leslie G. Butler. She was honored with the "Superior Chemistry Research Assistant" (1990-91) by the Department of Chemistry at LSU.

Results from these studies have been presented by Ae Ja Kim at the 39th ACS Southwest Regional Meeting and at the 32nd Experimental NMR Conference. She is the first author of two papers: "The ^{13}C NMR Chemical Shielding Tensor of the Bridging Methylene Unit in *cis*-(μ-CH_2)(μ-CO)[FeCp(CO)]$_2$" published in the *Journal of the American Chemical Society*, **1991**, *113*, 4831-8 and "Deuterium Quadrupole Coupling Constants and Asymmetry Parameters in Bridging Metal Hydride Complexes" which has been accepted for publication by the same journal. In addition, three other manuscripts have been submitted for review:"Solid-State ^{13}C and ^{31}P NMR Chemical Shielding Tensors in Square-Planar Metal Complexes and Metal Dimers" has been submitted to *Inorganic Chemistry*, "Resolving Two Inequivalent Sites with Deuterium MAS NMR" has been submitted to *Journal of Magnetic Resonance*, and "Nonlinear Least-Squares Fitting Procedure for Solid-State NMR Powder Patterns" has been submitted to *Concepts in Magnetic Resonance*.

DOCTORAL EXAMINATION AND DISSERTATION REPORT

Candidate: Ae Ja Kim

Major Field: Chemistry (Analytical)

Title of Dissertation: Solid-State NMR Studies of Organometallic Complexes

Approved:

Leslie G. Butler
Major Professor and Chairman

Kathleen dela Peña McCook
Dean of the Graduate School

EXAMINING COMMITTEE:

Robert J. Gale

Richard Dmlay

Andrew W. Ewaniuk

Paul S Russo

T. W. Robinson

Date of Examination:

November 13, 1991